Title
Sensitivity Analysis and Uncertainty Quantification in Reduced-Order Monopropellant Catalyst Bed Model

Author
Kerr, Daniel Hunter

Publication Date
2019

Peer reviewed|Thesis/dissertation

UNIVERSITY OF CALIFORNIA

Los Angeles

Sensitivity Analysis and Uncertainty Quantification in Reduced-Order Monopropellant Catalyst Bed Model

A thesis submitted in partial satisfaction
of the requirements for the degree
Master of Science in Aerospace Engineering

by

Daniel Hunter Kerr

2019

ABSTRACT OF THE THESIS

Sensitivity Analysis and Uncertainty Quantification in
Reduced-Order Monopropellant Catalyst Bed Model

by

Daniel Hunter Kerr
Master of Science in Aerospace Engineering
University of California, Los Angeles, 2019
Professor Ann R. Karagozian, Chair

The present study replicates a 1D, steady, chemically-reacting, reduced-order model for hydrogen peroxide flow through a monopropellant catalyst bed as described in Pasini et al. [9] with model validation completed by comparison with both model data and experimental data from Jung et al. [10]. Adaptations were made to improve heat transfer capabilities within the model and to adapt the model such that a hydroxylammonium nitrate and water mixture could be used as the propellant. Polynomial chaos expansion was implemented to decrease sampling time in order to perform non-deterministic analyses including: quantification of global sensitivities using Sobol indices, construction of axial property profiles with uncertainty envelopes for random physical inputs, and construction of posterior probability distributions with confidence intervals for variation in chemical tuning parameters. Results from the study show that model behavior is primarily governed by propellant mass fraction and activation energy of the global reaction. Additionally, posterior distributions indicate that activation energy and number of active sites per volume are related by a logarithmic family of solutions as a result of the reaction advancement gradient form in the model.

The thesis of Daniel Hunter Kerr is approved.

Raymond M. Spearrin

Xiaolin Zhong

Ann R. Karagozian, Committee Chair

University of California, Los Angeles

2019

To Mom and Dad,

who made sure I watched enough sci-fi growing up.

TABLE OF CONTENTS

LIST OF FIGURES

LIST OF TABLES

LIST OF SYMBOLS

Symbols

A	cross-sectional area
A_{f2}	Arrhenius preexponential constant
A_{specific}	specific Arrhenius preexponential
a_s	catalyst surface area per volume
C	concentration
C_d	diffusion coefficient
C_f	friction coefficient
c_p	molar specific heat
D	bed diameter
D_p	pellet diameter
G	bed loading
H	enthalpy
h	molar specific enthalpy
K_1	adsorption equilibrium constant
k_{b1}	backward adsorption constant
k_{f1}	forward adsorption constant
L	bed length
$\dot{m}$	mass flow rate
$\mathcal{M}$	molar mass
$\dot{n}$	molar flow rate
N_s	# active sites per volume
p	pressure
Q	heat
q	heat rate
R	universal gas constant
$\dot{r}$	volumetric reaction rate
Re	Reynolds number
Sc	Schmidt number
S_p	pellet surface area
T	temperature
u	superficial flow velocity
$\dot{V}$	volumetric flow rate
x	position
x_s	species mole fraction
Y	mass fraction

Greek Letters

α	void fraction
ϵ	evaporation parameter
$\tilde{\varepsilon}$	bed porosity
λ	advancement parameter
μ	dynamic viscosity, mean
ν	kinematic viscosity
ν_j	moles of species j
θ	relative site occupancy
ρ	density
σ	standard deviation

Subscripts

ad	adiabatic decomposition
b	boiling
c	catalytic
do	dryout

$g,\ (g)$	gas phase
$i,\ o$	initial quantity
$l,\ (l)$	liquid phase
s	species
sat	saturation
t	stagnation
th	thermal
v	vapor

Superscripts

$''$	product quantity
$'$	reactant quantity
$\circ$	standard condition
(i)	initial condition
(j)	arbitrary step j
(k)	arbitrary step k
(s)	catalytic surface quantity

ACKNOWLEDGMENTS

Research conducted for the study at hand was made possible by the invaluable guidance and assistance provided by both peers and mentors at UCLA and the Air Force Research Laboratory at Edwards Air Force Base.

It is of paramount importance that I express the utmost gratitude and appreciation for the mentorship provided by Professor Ann Karagozian. Her commitment to excellence and expert guidance are monumental sources of inspiration and have been essential to my growth as an engineer. Furthermore, her kindness and willingness to offer a helping hand served to create an extremely welcome environment within the Energy and Propulsion Research Laboratory at UCLA. Additional thanks are due to Professor Mitchell Spearrin and Professor Xiaolin Zhong for their service on my Master's committee as well as their continued mentorship in both my undergraduate and graduate years at UCLA.

A great deal of thanks are due to Dr. David Bilyeu for his mentorship in terms of both technical guidance and lessons in establishing good engineering practices. The completion of this research endeavor would not have been possible without his dedicated support. I would also like to express my gratitude towards Dr. Justin Koo and the remainder of the In-Space Propulsion branch for all of their insights and advice.

Lastly, I would like express my gratitude for my friends and family for their unerring support, constant encouragement, and remarkable willingness to let me ramble on about my thesis and its contents.

CHAPTER 1

Introduction

Recently, efforts have been made to implement "green propellants" for in-space chemical propulsion in order to reduce the risk associated with handling and preparing toxic monopropellants which would consequently lower costs concomitant with the level of precaution taken in these processes. One propellant of interest is high-concentration hydrogen peroxide due to its simplicity of use as well as its reduced toxicity when compared to the commonly used hydrazine. Even with its reduced toxicity, hydrogen peroxide (H_2O_2) still presents some risk to those handling it. H_2O_2 poses a health threat at exposure levels of only 75 ppm [1] and has a rather high vapor pressure [2]. Other green propellants that are primarily comprised of ionic liquids are even more promising in terms of safety due to their very low vapor pressures [3]. In addition to reduced toxicity, ionic liquid propellants, such as the hydroxylammonium nitrate (HAN) based propellant AF-M315, may yield benefits in terms of increased specific impulse and increased density to improve storage capabilities on the spacecraft [4].

Modeling flow through monopropellant thrusters, particularly using reduced-order models for the chemical reaction and transport processes, is critical to the thruster design optimization process. The computational efficiency of reduced-order models facilitates conducting many simulations in a short time frame which is essential for both predicting the performance of different thruster configurations as well as analyzing performance sensitivities for various inputs. Despite the value of utilizing a high efficiency model, monopropellant reduced-order modeling capabilities are not very extensive. This is likely due to the difficulty of accurately approximating the transient, multiphase, chemically reacting flow within the catalyst bed. Assumptions must be made regarding heat transfer within the bed, dominant reaction mechanisms, interactions between the phases, as well as flow interaction with the catalytic

material.

Decomposition of H_2O_2 was examined in a study by Johnson et al. [5] which attempted to analyze a transient pressure instability in a pressure-fed H_2O_2/JP-8 rocket engine. The catalyst bed domain was split into 2 control volumes, one for the liquid H_2O_2-H_2O mixture and one for the gaseous mixture of O_2 and steam. The control volumes were separated by a decomposition plane where it was assumed that the entire decomposition and evaporation of the mixture took place. The decomposition plane's location was determined as a function of time dependent on the required liquid residence time within the bed.

On the opposite scale of the study by Johnson et al., a study on modeling H_2O_2 decomposition for the purposes of using it as a monopropellant in MEMS thrusters to provide micro-Newton level thrust was conducted by Zhou and Hitt [6]. In this study, a 1D, steady, gas-liquid mixture model with five sub-regions was formulated. The five sub-regions dictated model behavior and were broken into: mixture heating, H_2O vaporization, H_2O_2 heating, H_2O_2 vaporization, and gas phase heating. Transition between the sub-regions was dependent on the mixture temperature. Catalytic decomposition of the H_2O_2 could be modeled using a constant rate or through temperature-dependent finite rate kinetics via an Arrhenius rate. Parameter sensitivity calculations in this study were limited to determining the optimal bed length for constant reaction rate versus an Arrhenius rate representation for the single step reaction kinetics as well as comparing the results from an adiabatic study to that with conductive heat losses.

Chiappetta et al. [7] developed a model of catalytically decomposing H_2O_2 through silver screens using the commercial software FLUENT. Flow through a porous medium was modeled by applying a body force on the fluid elements using Darcy's law with terms calibrated using experimental data. In this study, each chemical species is modeled as a separate fluid in which density is not pressure-dependent. Similar to previously described studies, H_2O_2 decomposition is modeled using a one-step global reaction governed by an Arrhenius rate. In this case, the preexponential factor varied linearly with the surface-to-volume ratio of the catalyst bed with a constant activation energy.

A 1D, steady, adiabatic model focusing on the thermal decomposition of H_2O_2 through a catalyst bed is described in Corpening et al. [8]. Once again, decomposition is based on a single step Arrhenius rate. This model accounts for droplet evaporation and implements control volume conservation of mass, momentum, and energy. The gas phase mixture evaporated from the droplets is assumed to have the same composition of the droplet liquid due to the small droplet size and rapid evaporation process.

The model of primary interest in this study is that described in Pasini et al. [9]. This model was replicated for the study at hand and as such the solution methodology is described at in great detail later in the text. Pasini et al. developed a 1D, steady, adiabatic, mixture model with the aim of simulating H_2O_2 decomposition in a pellet bed reactor, as well as conducted parameteric studies primarily pertaining to catalyst bed geometry. A distinction between the concentration of H_2O_2 in the bulk flow and at the catalytic surface is made using the mass-momentum Reynolds analogy. A single global reaction is split into two steps through catalytic adsorption and desorption processes with decomposition governed by an Arrhenius reaction rate. The model is governed by two quasi-linear ordinary differential equations (ODEs) that define the gradients in reaction advancement, or H_2O_2 decomposition, and pressure drop. Several tuning parameters appear in the reaction advancement gradient equation as a consequence of implementing the Arrhenius reaction rate and catalytic adsorption. While tuning was performed by Pasini et al. [9], both model data and experimental data from Jung et al. [10], another study that replicated the Pasini et al. model and conducted their own catalyst bed testing, were used in the tuning procedure as the Jung et al. study generated more experimental data for model validation.

While several of the previously mentioned studies conducted studies on parameter sensitivity, they were primarily interested in optimizing thruster performance by altering the catalyst bed geometry. Output sensitivity to thermochemical data, reaction rate tuning parameters, and physical input parameters was deemed of sufficient interest to be investigated in this study. Both sensitivity analyses and uncertainty quantification were conducted for these inputs to robustly quantify the input parameter impact on relevant outputs of the

model. Ultimately, results from the analysis would be used to formulate a generic understanding of sensitivities within a monopropellant catalyst bed and to inform the design of experiments for HAN-based monopropellant thruster testing at Edwards AFB (AFRL/RQR).

CHAPTER 2

Catalyst Bed Models

2.1 Governing Equations and Solution Method

The catalyst bed models presented in this paper are based on the homogeneous two-phase reacting flow model in Pasini et al. [9]. Flow properties are determined at each node in a 1D spatial domain with property evolution driven by two first-order ODEs defining the gradients in pressure and reaction advancement. The domain can be split into 3 relevant regions: Region I, pure liquid heating region ($\epsilon = 0$), Region II, liquid-vapor region ($0 < \epsilon < 1$), Region III, pure vapor heating region ($\epsilon = 1$), where ϵ is the evaporation parameter or the molar fraction of vapor in the mixture. The governing equations for the hydrogen peroxide (H_2O_2) model is as follows.

2.1.1 H_2O_2 Model

A pure liquid mixture of H_2O_2 and H_2O is assumed to enter the catalyst bed with some mass flow rate $\dot{m}$, initial pressure p_i, initial temperature T_i, and mass concentration of H_2O_2 Y. Upon contact with the catalytic material in the reactor bed, H_2O_2 begins to decompose into O_2 and H_2O as dictated by the following global reaction:

$$H_2O_2 \rightarrow H_2O + \frac{1}{2}O_2 \tag{2.1}$$

Conservation of mass dictates that:

$$\dot{m} = \dot{n}^{(i)}_{H_2O_2}\mathcal{M}_{H_2O_2} + \dot{n}^{(i)}_{H_2O}\mathcal{M}_{H_2O} \tag{2.2}$$

Local flow composition can be determined using the molar flow rates of each component in Equations 2.3 - 2.5 below with reaction advancement parameter λ representing the molar flow rate of reacted H_2O_2.

$$\dot{n}_{H_2O_2} = \dot{n}^{(i)}_{H_2O_2} - \lambda = \frac{Y\dot{m}}{\mathcal{M}_{H_2O_2}} - \lambda \tag{2.3}$$

$$\dot{n}_{H_2O} = \dot{n}^{(i)}_{H_2O} + \lambda = \frac{(1-Y)\dot{m}}{\mathcal{M}_{H_2O}} + \lambda \tag{2.4}$$

$$\dot{n}_{O_2} = \frac{1}{2}\lambda \tag{2.5}$$

Heat released from the exothermic decomposition of the H_2O_2 increases the mixture temperature to approach boiling conditions of the mixture. The mixture is considered to be boiling when the mixture temperature reaches the temperature as computed in the liquid-vapor region (Region II) with $\epsilon \approx 0$. Once the boiling condition has been reached, the mixture begins to evaporate causing both H_2O_2 and H_2O uniformly transition from the liquid phase to the vapor phase. Flow properties, apart from phase-specific properties such as densities, enthalpies, etc., are assumed to be equal in both phases. Dissolution of O_2 in the liquid phase due to the decomposition reaction is assumed to be negligible in both Regions I and II.

Temperature T and evaporation parameter ϵ are computed by solving a system of equations containing an enthalpy balance and summation of partial pressures. The enthalpy balance can be seen in Equation 2.8.

$$H_{H_2O_2} + H_{H_2O} + H_{O_2} = H \tag{2.6}$$

$$\begin{aligned}
&\dot{n}_{H_2O_2}\left\{\epsilon\left[h^{\circ}_{H_2O_2,(g)} + c_{pH_2O_2,(g)}(T-T^{\circ})\right] + (1-\epsilon)\left[h^{\circ}_{H_2O_2,(l)} + c_{pH_2O_2,(l)}(T-T^{\circ})\right]\right\} + \\
&\quad \dot{n}_{H_2O}\left\{\epsilon\left[h^{\circ}_{H_2O,(g)} + c_{pH_2O,(g)}(T-T^{\circ})\right] + (1-\epsilon)\left[h^{\circ}_{H_2O,(l)} + c_{pH_2O,(l)}(T-T^{\circ})\right]\right\} + \\
&\quad \dot{n}_{O_2}\left[h^{\circ}_{O_2} + c_{pO_2}(T-T^{\circ})\right] = H = H_o - \Delta Q
\end{aligned} \tag{2.7}$$

$$
\begin{aligned}
&\dot{n}_{\mathrm{O_2}}\left[h^{\circ}_{\mathrm{O_2}} + c_{p\mathrm{O_2}}(T - T^{\circ})\right] + \\
&\quad \epsilon\left\{\dot{n}_{\mathrm{H_2O_2}}\left[h^{\circ}_{\mathrm{H_2O_2},(g)} + c_{p\mathrm{H_2O_2},(g)}(T - T^{\circ})\right] + \dot{n}_{\mathrm{H_2O}}\left[h^{\circ}_{\mathrm{H_2O},(g)} + c_{p\mathrm{H_2O},(g)}(T - T^{\circ})\right]\right\} + \\
&\quad (1-\epsilon)\left\{\dot{n}_{\mathrm{H_2O_2}}\left[h^{\circ}_{\mathrm{H_2O_2},(l)} + c_{p\mathrm{H_2O_2},(l)}(T - T^{\circ})\right] + \dot{n}_{\mathrm{H_2O}}\left[h^{\circ}_{\mathrm{H_2O},(l)} + c_{p\mathrm{H_2O},(l)}(T - T^{\circ})\right]\right\} \\
&\quad = \dot{n}^{(i)}_{\mathrm{H_2O_2}}\left[h^{\circ}_{\mathrm{H_2O_2},(l)} + c_{p\mathrm{H_2O_2},(l)}(T_i - T^{\circ})\right] + \dot{n}^{(i)}_{\mathrm{H_2O}}\left[h^{\circ}_{\mathrm{H_2O},(l)} + c_{p\mathrm{H_2O},(l)}(T_i - T^{\circ})\right] - \Delta Q
\end{aligned}
\tag{2.8}
$$

Each enthalpy term depends on the species reference enthalpy h°, specific heat c_p, and reference temperature T° with initial enthalpies additionally depending on initial temperature T_i. The above enthalpy balance equation uniquely defines the mixture temperature in Regions I and III in which $\epsilon = 0$ and $\epsilon = 1$ respectively. Temperature can be solved for explicitly in these regions for constant specific heats but implicit methods may be required for temperature-dependent specific heats (specific heat equations found in Appendix A.3). Energy loss from a fluid element due to heat transfer, ΔQ, will be discussed later in Section 2.1.3.

Region II requires another equation as the evaporation parameter acts as another unknown under the following constraint: $0 < \epsilon < 1$. Temperature and evaporation parameter can be linked through the summation of partial pressures of each species. Summation of the partial pressures can be seen in Equation 2.9.

$$
p = p_{\mathrm{H_2O_2},(g)} + p_{\mathrm{H_2O},(g)} + p_{\mathrm{O_2}} \tag{2.9}
$$

It is assumed that the partial pressures of H_2O_2 and H_2O can be approximated as the liquid mole fraction multiplied by the saturation pressure at a given temperature for each respective species as seen in the following equations.

$$
p_{\mathrm{H_2O_2},(g)} = \frac{\dot{n}_{\mathrm{H_2O_2}}}{\dot{n}_{\mathrm{H_2O_2}} + \dot{n}_{\mathrm{H_2O}}} p_{\mathrm{H_2O_2,sat}}(T) \tag{2.10}
$$

$$
p_{\mathrm{H_2O},(g)} = \frac{\dot{n}_{\mathrm{H_2O}}}{\dot{n}_{\mathrm{H_2O_2}} + \dot{n}_{\mathrm{H_2O}}} p_{\mathrm{H_2O,sat}}(T) \tag{2.11}
$$

The partial pressure for O_2 can be obtained from Dalton's Law below where $x_{\mathrm{O_2}}$ is the mole

fraction of O_2 in the gas phase.

$$p_{O_2} = x_{O_2} p \tag{2.12}$$

$$p_{O_2} = \frac{\dot{n}_{O_2}}{\dot{n}_{O_2} + \epsilon(\dot{n}_{H_2O_2} + \dot{n}_{H_2O})} p \tag{2.13}$$

Substituting Equations 2.10, 2.11, and 2.13 into Equation 2.9 and rearranging we arrive at Equation 2.14 which describes the contributions of H_2O_2 and H_2O to the mixture pressure and is denoted p_v.

$$\left[1 - \frac{\dot{n}_{O_2}}{\dot{n}_{O_2} + \epsilon(\dot{n}_{H_2O_2} + \dot{n}_{H_2O})}\right] p = \frac{\dot{n}_{H_2O_2} p_{H_2O_2,\mathrm{sat}}(T) + \dot{n}_{H_2O} p_{H_2O,\mathrm{sat}}(T)}{\dot{n}_{H_2O_2} + \dot{n}_{H_2O}} = p_v(T, \lambda) \tag{2.14}$$

In Pasini et al. [9], arguments for region location are based on the mixture pressure as compared to p_v. The relations for these region definitions are as follows:

$$p_i \geq p_v(T_i, 0) \Rightarrow T \leq T_b(p_i) \tag{2.15}$$

$$p \leq \frac{\dot{n}_{H_2O_2} + \dot{n}_{H_2O} + \dot{n}_{O_2}}{\dot{n}_{H_2O_2} + \dot{n}_{H_2O}} p_v(T, \lambda) \Rightarrow T \geq T_{do}(p, \lambda) \tag{2.16}$$

In the model presented in this paper, the boiling condition is determined by comparing temperatures computed through the different equations used in Regions I and II. Before describing the different equations used in each region, it is important that the solution algorithm be discussed first.

Due to the temperature dependence on the specific heats, a single variable (T) nonlinear iterative solver was used in each region. The method implemented was a sequential combination of Newton's method and the bisector method (the bisector method was only used if Newton's method failed to converge to the specified criterion within a chosen number of iterations). Newton's method for temperature can be seen in Equation 2.17 in which j is an arbitrary iteration and $F(T)$ is some region-dependent equation in T, based on the enthalpy balance and summation of partial pressures above, equal to 0.

$$T^{(j+1)} = T^{(j)} + \mathrm{d}T^{(j)} \quad \text{where} \quad \mathrm{d}T^{(j)} = -\frac{F(T^{(j)})}{\mathrm{d}F(T^{(j)})} \tag{2.17}$$

In the instance the Newton's method was unable to converge to a satisfactory solution within 100 iterations (the typical evaluation requires approximately 7 iterations due to quadratic

convergence of Newton's method), the code switches to utilizing a bisector method. The bisector method algorithm is as follows (Steps 1 and 2 are only evaluated in the first iteration of the bisector method):

1. $T_1^{(j)} = (1 - 10^{-6})T^{(j)} \quad \text{for} \quad j_{\text{bisector}} = 1$
2. $T_2^{(j)} = (1 + 10^{-6})T^{(j)} \quad \text{for} \quad j_{\text{bisector}} = 1$
3. $T_3^{(j)} = \frac{T_2^{(j)} + T_1^{(j)}}{2}$
4. $F_i = F(T_i^{(j)}) \quad \text{for} \quad i = 1, 2, 3$
5. if $F_1 F_3 < 0$:

   $T_2^{(j+1)} = T_3^{(j)}, \qquad T_1^{(j+1)} = T_1^{(j)}$

   else if $F_2 F_3 < 0$:

   $T_1^{(j+1)} = T_3^{(j)}, \qquad T_2^{(j+1)} = T_2^{(j)}$

   else if $F_1 F_2 > 0$:

   $T_1^{(j+1)} = 0.99 T_1^{(j)}, \qquad T_2^{(j+1)} = 1.01 T_2^{(j)}$

The final "*else if*" in Step 5 of the bisector algorithm expands the bounds of the interval of interest by decreasing the magnitude of the lower bound and increasing that of the upper bound in the case that both F_1 and F_2 are of the same sign. Assuming that there can be only a single solution within the interval $[T_1, T_2]$, F_1 and F_2 having the same sign implies that the solution lies outside the interval $[T_1, T_2]$.

Functions F for determining T, as well as the qualifying conditions for operating within the region, are described below for each region:

Region I:

$$\text{Condition: } \epsilon = 0 \text{ in previous step AND } T < T_b$$

$$F(T) = H - \dot{n}_{\text{O}_2} h_{\text{O}_2} - \dot{n}_{\text{H}_2\text{O}_2} h_{\text{H}_2\text{O}_2,(l)} - \dot{n}_{\text{H}_2\text{O}} h_{\text{H}_2\text{O},(l)}$$

$$\text{where} \quad h_s = h_s^\circ + c_{ps}(T - T^\circ) \quad \text{for species } s$$

$$\epsilon = 0$$

Region II:

$$\text{Condition: } (T \geq T_b \text{ OR } \epsilon \neq 0 \text{ in previous step}) \text{ AND } \epsilon \text{ as computed below is } < 1$$

$$F(T) = \left[1 - \frac{\dot{n}_{O_2}}{\dot{n}_{O_2} + \epsilon(T)(\dot{n}_{H_2O_2} + \dot{n}_{H_2O})}\right] p - \frac{\dot{n}_{H_2O_2} p_{H_2O_2,\text{sat}} + \dot{n}_{H_2O} p_{H_2O,\text{sat}}}{\dot{n}_{H_2O_2} + \dot{n}_{H_2O}}$$

$$\epsilon(T) = \frac{H - \dot{n}_{O_2} h_{O_2} - \dot{n}_{H_2O_2} h_{H_2O_2,(l)} - \dot{n}_{H_2O} h_{H_2O,(l)}}{\dot{n}_{H_2O_2}(h_{H_2O_2,(g)} - h_{H_2O_2,(l)}) + \dot{n}_{H_2O}(h_{H_2O,(g)} - h_{H_2O,(l)})}$$

Region III:

$$\text{Condition: } \epsilon \geq 1 \text{ in previous step}$$

$$F(T) = H - \dot{n}_{O_2} h_{O_2} - \dot{n}_{H_2O_2} h_{H_2O_2,(g)} - \dot{n}_{H_2O} h_{H_2O,(g)}$$

$$\epsilon = 1$$

Boiling temperature T_b is calculated using $F(T)$ in Region II so that the condition $T < T_b$ in Region I determines when the temperature curves of Regions I and II intersect. Upon switching from Region I to Region II, ϵ is no longer constrained to be 0 and is instead a function of temperature and the molar flow rate of O_2 which was previously neglected. Because of this difference in the formulation of ϵ, there is a small discontinuity in flow properties at the transition between the two regions. This is the primary reason for using evaporation parameter driven region conditions. By determining the boiling and evaporation conditions using the above method as opposed to pressure-based definitions (boiling occurs when $p = p_v$), the property discontinuities can be reduced between Regions I and II. Once fully evaporated, the mixture regains pressure independence as it operates under the perfect gas assumption.

Using the T and ϵ as determined above, the liquid and gaseous volumetric flow rates are calculated using Equations 2.18 and 2.19 respectively.

$$\dot{V}_l = (1 - \epsilon)\left[\frac{\dot{n}_{H_2O_2}\mathcal{M}_{H_2O_2}}{\rho_{H_2O_2,(l)}} + \frac{\dot{n}_{H_2O}\mathcal{M}_{H_2O}}{\rho_{H_2O,(l)}}\right] \tag{2.18}$$

$$\dot{V}_g = \left[\dot{n}_{O_2} + \epsilon(\dot{n}_{H_2O_2} + \dot{n}_{H_2O})\right]\frac{\mathcal{R}T}{p} \tag{2.19}$$

The volumetric flow rates for each phase can be summed to form the total volumetric flow

rate as seen below:

$$\dot{V} = \dot{V}_l + \dot{V}_g \tag{2.20}$$

Using the volumetric flow rates, additional properties of the homogeneous mixture can be computed. Mixture density and void fraction of the catalyst bed are calculated using Equations 2.21 and 2.22 respectively.

$$\rho = \frac{\dot{n}_{H_2O_2}\mathcal{M}_{H_2O_2} + \dot{n}_{H_2O}\mathcal{M}_{H_2O} + \dot{n}_{O_2}\mathcal{M}_{O_2}}{\dot{V}} = \frac{\dot{m}}{\dot{V}} \tag{2.21}$$

$$\alpha = \frac{\dot{V}_g}{\dot{V}} \tag{2.22}$$

Using the void fraction, the dynamic and kinematic mixture viscosities can be found.

$$\mu \cong \mu_l(1-\alpha) + \mu_g\alpha \tag{2.23}$$

$$\nu = \frac{\mu}{\rho} \tag{2.24}$$

Liquid and gas phase dynamic viscosities are computed using the following equations:

$$\mu_l = \left[\sum_s Y_s \mu_s^{1/3}\right]^3 \tag{2.25}$$

$$\mu_g = \frac{\sum_s x_s \mu_s \mathcal{M}_s^{0.5}}{\sum_s x_s \mathcal{M}_s^{0.5}} \tag{2.26}$$

in which x_s and Y_s are the species mole fractions and mass fractions respectively defined by the following relations:

$$x_s = \frac{\dot{n}_s}{\sum_s \dot{n}_s} \tag{2.27}$$

$$Y_s = \frac{\dot{n}_s \mathcal{M}_s}{\dot{m}} \tag{2.28}$$

Concentrations for each species s can be determined using the following equation:

$$C_s = \frac{\dot{n}_s}{\dot{V}} \tag{2.29}$$

While the total mixture concentration is defined as:

$$C = \sum_s C_s = \frac{1}{\dot{V}} \sum_s \dot{n}_s \tag{2.30}$$

Additionally, the specific heat of constant pressure can be computed using Equation 2.33.

$$c_{p\mathrm{H_2O_2}} = (1-\epsilon)c_{p\mathrm{H_2O_2},(l)} + \epsilon c_{p\mathrm{H_2O_2},(g)} \tag{2.31}$$

$$c_{p\mathrm{H_2O}} = (1-\epsilon)c_{p\mathrm{H_2O},(l)} + \epsilon c_{p\mathrm{H_2O},(g)} \tag{2.32}$$

$$c_p = \frac{\dot{n}_{\mathrm{H_2O_2}} c_{p\mathrm{H_2O_2}} + \dot{n}_{\mathrm{H_2O}} c_{p\mathrm{H_2O}} + \dot{n}_{\mathrm{O_2}} c_{p\mathrm{O_2}}}{\dot{n}_{\mathrm{H_2O_2}} + \dot{n}_{\mathrm{H_2O}} + \dot{n}_{\mathrm{O_2}}} \tag{2.33}$$

Because evaporation parameter ϵ and temperature T are functions of the local values of pressure p and reaction advancement parameter λ, all mixture properties are purely defined by p and λ as well.

H_2O_2 decomposition on the catalytic surface S is modeled using fast equilibrium adsorption and first-order finite-rate product desorption and is represented using the chemical reaction in Equation 2.34.

$$\mathrm{H_2O_2} + \mathrm{S} \underset{k_{b1}}{\overset{k_{f1}}{\rightleftharpoons}} \mathrm{S-H_2O_2(ad)} \xrightarrow{k_{f2}} \mathrm{H_2O} + \frac{1}{2}\,\mathrm{O_2} \tag{2.34}$$

Denoting a molar concentration on the catalytic surface as $C^{(s)}$, the forward and backward reaction rates for the catalytic reaction can be related using reactant adsorption equilibrium condition in Equation 2.37. In this equation k_{f1} is the forward adsorption constant, k_{b1} is the backward adsorption constant, and K_1 is the adsorption equilibrium constant. Additionally N_s is the number of active adsorption sites per unit volume of the catalyst bed and θ is the relative occupancy of the sites.

$$k_{f1} C^{(s)}_{\mathrm{H_2O_2}} N_s (1-\theta) = k_{b1} N_s \theta \tag{2.35}$$

$$K_1 C^{(s)}_{\mathrm{H_2O_2}} (1-\theta) = \theta \qquad \text{where} \qquad K_1 = \frac{k_{f1}}{k_{b1}} \tag{2.36}$$

$$\theta = \frac{K_1 C^{(s)}_{\mathrm{H_2O_2}}}{1 + K_1 C^{(s)}_{\mathrm{H_2O_2}}} \tag{2.37}$$

The volumetric reaction rate can be obtained from product desorption finite-rate kinetics in the following equation where k_{f2} is represented by an Arrhenius rate with Arrhenius preexponential constant A_{f2} and activation energy E_{f2}.

$$\dot{r} = k_{f2} N_s \theta = A_{f2} e^{-E_{f2}/\mathcal{R}T} N_s \frac{K_1 C^{(s)}_{\mathrm{H_2O_2}}}{1 + K_1 C^{(s)}_{\mathrm{H_2O_2}}} \tag{2.38}$$

Arrhenius preexponential constant A_{f2} is assumed to be proportional to the catalyst surface area per unit volume [7] and is defined as in Equation 2.39 with surface area per unit volume [10] in Equation 2.40.

$$A_{f2} = a_s A_{\text{specific}} \tag{2.39}$$

$$a_s = (1 - \tilde{\varepsilon})\frac{6}{D_p} \tag{2.40}$$

H_2O_2 concentration at the catalytic surface can be approximated by making a similarity argument between mass and momentum transport with the generalized Reynolds analogy for a viscous, diffusive boundary layer along a flat plate. This simplifying assumption results in an expression relating the ratio of the nondimensional diffusion coefficient and the friction coefficient to the Schmidt number of the flow as shown in Equation 2.41.

$$\frac{C_d}{C_f} = \frac{\dot{m}_j^{(s)}/\rho u(Y_j - Y_j^{(s)})}{2\tau^{(s)}/\rho u^2} \approx \frac{1}{2}\text{Sc}^{-1/2} \cong \frac{1}{2} \Rightarrow C_f \cong 2C_d \tag{2.41}$$

In the above equation, it is assumed that the Schmidt number is equal to 1 which is generally true for gas mixtures although is less accurate for liquid mixtures [11]. Additionally, the flow friction coefficient is formulated assuming that the viscous friction along the pellet surface S_p is the sole source of the pressure losses in the bed as seen below.

$$\frac{\mathrm{d}p_{\text{loss}}}{\mathrm{d}x} = C_f \frac{1}{2}\rho u^2 \frac{1}{A}\frac{\mathrm{d}S_p}{\mathrm{d}x} \tag{2.42}$$

Assuming tetrahedral packing of spherical pellets (another relation would be need to be established for alternate pellet shapes or to account for spatially-varying randomness in pellet packing efficiency):

$$\frac{1}{A}\frac{\mathrm{d}S_p}{\mathrm{d}x} = \frac{\pi\sqrt{2}}{D_p} \tag{2.43}$$

$$\frac{\mathrm{d}p_{\text{loss}}}{\mathrm{d}x} \cong C_d \rho u^2 \frac{\pi\sqrt{2}}{D_p} \tag{2.44}$$

The spatial pressure loss gradient through the catalyst bed takes the following form:

$$\frac{\mathrm{d}p_{\text{loss}}}{\mathrm{d}x} = \left(c_1\left[\frac{1-\tilde{\varepsilon}}{Re_p}\right]^{c_2} + c_3\right)\frac{1-\tilde{\varepsilon}}{\tilde{\varepsilon}^3}\frac{\rho u^2}{D_p} \qquad \text{where} \qquad Re_p = \frac{uD_p}{\nu} \tag{2.45}$$

in which $\tilde{\varepsilon}$ is the bed porosity, D_p is the pellet diameter, and u is the superficial flow velocity in the x-direction, that is, the hypothetical flow velocity for a pelletless bed. The equation for u along with its derivation will be shown later. In contrast to Pasini et al., in which bed porosity $\tilde{\varepsilon}$ is treating as a model tuning parameter, the value of $\tilde{\varepsilon}$ is determined using Equation 2.46 from Bey and Eigenberger [12] in which D is the bed diameter. The equation is limited to predicting bed porosity for spherical pellets.

$$\tilde{\varepsilon} = 0.375 + 0.34\frac{D_p}{D} \tag{2.46}$$

The pressure loss gradient contains three constants c_1, c_2, and c_3 that are defined by the chosen empirical model. Each model is constrained by its own range of Reynolds number and bed porosity and may also have restrictions based on pellet geometry. Several potential models can be seen below in Table 2.1.

Model	c_1	c_2	c_3	$Re^* = Re/(1-\tilde{\varepsilon})$	$\tilde{\varepsilon}$	Pellet Shape
Ergun	150	1	1.75	$0.67 < Re^* < 2300$	$0.4 < \tilde{\varepsilon} < 0.65$	various
Brauer	160	0.1	3.1	$2 < Re^* < 20000$	$0.331 < \tilde{\varepsilon} < 0.681$	spheres
Tallmadge	150	0.16	4.2	$0.1 < Re^* < 10000$	$0.34 < \tilde{\varepsilon} < 0.41$	spheres

Table 2.1: Pressure Drop through Porous Media Models [13]

In order to replicate the Pasini et al. model, the Ergun model will be used although it will be shown later that the Ergun model assumptions are violated for the simulated catalyst bed conditions.

Returning to the formulation of H_2O_2 concentration at the catalytic surface, it is now possible to substitute in the equation for the pressure loss gradient.

$$\frac{\mathrm{d}p_{\text{loss}}}{\mathrm{d}x} = \left(150\frac{1-\tilde{\varepsilon}}{Re_p} + 1.75\right)\frac{1-\tilde{\varepsilon}}{\tilde{\varepsilon}^3}\frac{\rho u^2}{D_p} \cong C_d \rho u^2 \frac{\pi\sqrt{2}}{D_p} \tag{2.47}$$

$$\Rightarrow C_d \cong \frac{1}{\pi\sqrt{2}}\left(150\frac{1-\tilde{\varepsilon}}{Re_p} + 1.75\right)\frac{1-\tilde{\varepsilon}}{\tilde{\varepsilon}^3} \tag{2.48}$$

Using the definition of the diffusion coefficient, it may be rewritten to obtain an equation

for the mass flux of H_2O_2 at the catalyst surface $\tilde{\dot{m}}^{(s)}_{H_2O_2}$.

$$C_d = \dot{m}^{(s)}_{H_2O_2}/\rho u(Y_{H_2O_2} - Y^{(s)}_{H_2O_2}) \tag{2.49}$$

$$\dot{m}^{(s)}_{H_2O_2} = C_d \rho u(Y_{H_2O_2} - Y^{(s)}_{H_2O_2}) \tag{2.50}$$

$$\Rightarrow \tilde{\dot{m}}^{(s)}_{H_2O_2} = C_d \rho u(Y_{H_2O_2} - Y^{(s)}_{H_2O_2}) \frac{1}{A}\frac{\mathrm{d}S_p}{\mathrm{d}x} \tag{2.51}$$

$$\tilde{\dot{m}}^{(s)}_{H_2O_2} = C_d \rho u(Y_{H_2O_2} - Y^{(s)}_{H_2O_2}) \frac{\pi\sqrt{2}}{D_p} = \mathcal{M}_{H_2O_2}\dot{r} \tag{2.52}$$

By assuming that equimolar counterdiffusion, binary mixture diffusion such that the movement of each molecule of species A is countered by that of species B [14], occurs at the impermeable catalytic surface and noting that this condition is equivalent to equimass diffusion due to H_2O_2 having the same molar mass both in the fluid phase and on the catalytic surface, the mass fraction of H_2O_2 on the catalytic surface can be written as follows:

$$Y^{(s)}_{H_2O_2} = \frac{\mathcal{M}_{H_2O_2} C^{(s)}_{H_2O_2}}{\mathcal{M}_{H_2O_2} C^{(s)}_{H_2O_2} + \mathcal{M}_P(C - C^{(s)}_{H_2O_2})} \tag{2.53}$$

in which $\mathcal{M}_P$ is the molar mass of the mixture.

Combining expressions for $\tilde{\dot{m}}^{(s)}_{H_2O_2}$, $Y^{(s)}_{H_2O_2}$, and $\dot{r}$ results in Equation 2.54 below.

$$C_d \rho u \left[Y_{H_2O_2} - \frac{\mathcal{M}_{H_2O_2} C^{(s)}_{H_2O_2}}{\mathcal{M}_{H_2O_2} C^{(s)}_{H_2O_2} + \mathcal{M}_P(C - C^{(s)}_{H_2O_2})} \right] \frac{\pi\sqrt{2}}{D_p} \tag{2.54}$$
$$= \mathcal{M}_{H_2O_2} A_{f2} e^{-E_{f2}/\mathcal{R}T} N_s \frac{K_1 C^{(s)}_{H_2O_2}}{1 + K_1 C^{(s)}_{H_2O_2}}$$

By applying the assumptions consistent with 1D, steady, homogeneous, creeping flow to governing equations results in several key relations. Applying the assumptions to conservation of mass results in the following:

$$\oint_S \rho \boldsymbol{u} \cdot \mathrm{d}\boldsymbol{S} = 0 \Rightarrow \frac{\mathrm{d}(\rho u)}{\mathrm{d}x} = 0 \Rightarrow \rho u = G \equiv \text{constant} \Rightarrow u = \frac{G}{\rho} \tag{2.55}$$

$$G = \frac{\dot{m}}{A} \Rightarrow u = \frac{\dot{m}}{\rho A} = \frac{\dot{V}}{A} \tag{2.56}$$

By conservation of species:

$$\oint_S C_j \boldsymbol{u} \cdot \mathrm{d}\boldsymbol{S} = \int_V (\nu_j'' - \nu_j')\dot{r}\mathrm{d}V \tag{2.57}$$

$$\Rightarrow \frac{\mathrm{d}(C_j u)}{\mathrm{d}x} = u\frac{\mathrm{d}C_j}{\mathrm{d}x} + C_j\frac{\mathrm{d}u}{\mathrm{d}x} \cong u\frac{\mathrm{d}C_j}{\mathrm{d}x} = (\nu_j'' - \nu_j')\dot{r} \tag{2.58}$$

Additionally, by conservation of momentum for a 1D calculation:

$$\oint_S \rho \boldsymbol{u}\boldsymbol{u} \cdot \mathrm{d}\boldsymbol{S} = -\oint_S p \mathrm{d}\boldsymbol{S} + \oint_S \tau \cdot \mathrm{d}\boldsymbol{S} \tag{2.59}$$

$$\Rightarrow \rho u \frac{\mathrm{d}u}{\mathrm{d}x} = -\frac{\mathrm{d}p}{\mathrm{d}x} - \frac{\mathrm{d}p_{\text{loss}}}{\mathrm{d}x} \cong 0 \tag{2.60}$$

$$\Rightarrow \frac{\mathrm{d}p}{\mathrm{d}x} = -\frac{\mathrm{d}p_{\text{loss}}}{\mathrm{d}x} \tag{2.61}$$

Assuming negligible viscous dissipation, that the stagnation enthalpy of the flow is defined by the enthalpies of formation and initial flow conditions, and that only losses are due to radial heat loss, the following can be found by conservation of energy:

$$\oint_S \rho h_t \boldsymbol{u} \cdot \mathrm{d}\boldsymbol{S} = -\frac{1}{A}\frac{\mathrm{d}\Delta Q}{\mathrm{d}x} \tag{2.62}$$

$$\Rightarrow \rho u \frac{\mathrm{d}h_t}{\mathrm{d}x} = \frac{1}{A}\frac{\mathrm{d}H_t}{\mathrm{d}x} = -\frac{1}{A}\frac{\mathrm{d}\Delta Q}{\mathrm{d}x} \tag{2.63}$$

$$\Rightarrow \frac{\mathrm{d}H_t}{\mathrm{d}x} = -\frac{\mathrm{d}\Delta Q}{\mathrm{d}x} \tag{2.64}$$

In the original formulation of this model by Pasini et al., the flow is entirely adiabatic and thus the specific stagnation enthalpy h_t is constant throughout the domain. Heat transfer in the model and its impact on the results will be discussed later in the paper. The differential concentration for a species j can be expressed as shown below.

$$\mathrm{d}C_j = \frac{\mathrm{d}\dot{n}_j}{\dot{V}} = \frac{\nu_j^{''} - \nu_j^{'}}{\dot{V}}\mathrm{d}\lambda \tag{2.65}$$

Substituting in the result from the conservation of species in Equation 2.58:

$$\frac{\mathrm{d}C_j}{\mathrm{d}x} = (\nu_j^{''} - \nu_j^{'})\frac{\dot{r}}{u} = \frac{\nu_j^{''} - \nu_j^{'}}{\dot{V}}\frac{\mathrm{d}\lambda}{\mathrm{d}x} \tag{2.66}$$

$$\Rightarrow \frac{\mathrm{d}\lambda}{\mathrm{d}x} = \frac{\dot{V}}{u}\dot{r} \tag{2.67}$$

From the derivations above, the governing ordinary differential equations (ODEs) of the model can be fully expanded into the forms seen in Equations 2.68 and 2.69. Boundary conditions for each of the ODEs can also be prescribed. As was mentioned previously, the inlet pressure p_i is a prescribed user input. Additionally, it will be assumed that no reaction

takes place prior to the mixture entering the catalyst bed.

$$\frac{\mathrm{d}\lambda}{\mathrm{d}x} = \frac{\dot{V}}{u} A_{f2} e^{-E_{f2}/\mathcal{R}T} N_s \frac{K_1 C^{(s)}_{\mathrm{H_2O_2}}}{1 + K_1 C^{(s)}_{\mathrm{H_2O_2}}}, \quad \lambda(0) = 0 \tag{2.68}$$

$$\frac{\mathrm{d}p}{\mathrm{d}x} = -\left(150\frac{1-\tilde{\varepsilon}}{Re_p} + 1.75\right)\frac{1-\tilde{\varepsilon}}{\tilde{\varepsilon}^3}\frac{\rho u^2}{D_p}, \quad p(0) = p_i \tag{2.69}$$

The two ODEs above can be numerically integrated to determine the spatial evolution of all flow properties as all non-constant flow properties are directly or indirectly functions of p and λ. A uniform grid Runge-Kutta 4 [15] was chosen as the ODE solver in this model. A description of how Runge-Kutta 4 is implemented is as follows:

$$\boldsymbol{f}(p,\lambda) = \begin{Bmatrix} \frac{\mathrm{d}p}{\mathrm{d}x}(p,\lambda) \\ \frac{\mathrm{d}\lambda}{\mathrm{d}x}(p,\lambda) \end{Bmatrix}, \quad \boldsymbol{y} = \begin{Bmatrix} p \\ \lambda \end{Bmatrix} \Rightarrow \boldsymbol{f}(\boldsymbol{y}) = \begin{Bmatrix} \frac{\mathrm{d}p}{\mathrm{d}x}(\boldsymbol{y}) \\ \frac{\mathrm{d}\lambda}{\mathrm{d}x}(\boldsymbol{y}) \end{Bmatrix}$$

$$\begin{aligned}
\boldsymbol{f}_1 &= \boldsymbol{f}(\boldsymbol{y}^{(k)}) \\
\boldsymbol{f}_2 &= \boldsymbol{f}(\boldsymbol{y}^{(k)} + \frac{1}{2}\boldsymbol{f}_1 dx) \\
\boldsymbol{f}_3 &= \boldsymbol{f}(\boldsymbol{y}^{(k)} + \frac{1}{2}\boldsymbol{f}_2 dx) \\
\boldsymbol{f}_4 &= \boldsymbol{f}(\boldsymbol{y}^{(k)} + \boldsymbol{f}_3 dx) \\
\boldsymbol{y}^{(k+1)} &= \boldsymbol{y}^{(k)} + \frac{dx}{6}\left(\boldsymbol{f}_1 + 2\boldsymbol{f}_2 + 2\boldsymbol{f}_3 + \boldsymbol{f}_4\right)
\end{aligned}$$

Figure 2.1 contains a block diagram depicting the overall solution methodology of the problem and illustrates the order in which flow properties are computed.

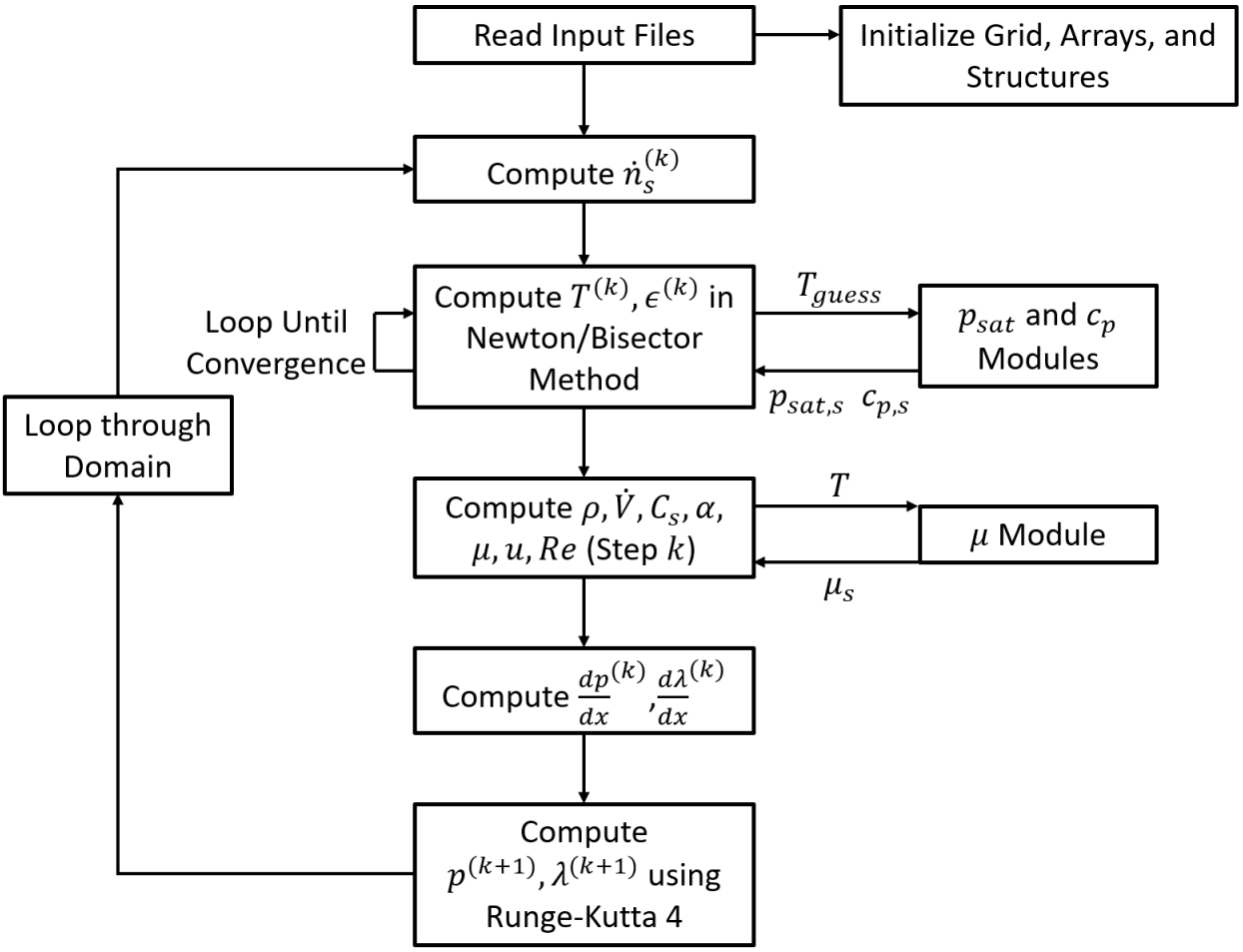

Figure 2.1: Model Solution Methodology Block Diagram

Upon termination of the outermost loop, the simulation is complete and has generated axial profiles for flow properties throughout the catalyst bed. Temperature profile $T(x)$ and pressure profile $p(x)$ are used in conjunction with experimental data to calibrate the chemistry coefficients N_s, K_1, and E_{f2}. It is worth noting that it would be equally valid to hold N_s constant and use A_{specific} as a tuning parameter. This is due to the fact that both N_s and A_{f2} directly appear only in Equation 2.68 in which they are directly multiplied together and thus functionally operate as a single tuning parameter.

2.1.2 HAN-H_2O Model

Modifications were made to the H_2O_2 model described in the previous subsection in order to model the flow of a HAN-H_2O mixture through a catalyst bed. Primarily, modifications consisted of changing thermophysical and material data to that of the new product and reactant species as a majority of the computational procedures are identical between the two models. The HAN-H_2O model follows the solution methodology outlines in Figure 2.1 with the only computational differences taking place within some of blocks regarding how several properties are computed. As in the H_2O_2 model, the HAN-H_2O model is governed by a two-step global reaction with catalytic interaction involving HAN ($H_4N_2O_4$):

$$\mathrm{H_4N_2O_4 + S \underset{k_{b1}}{\overset{k_{f1}}{\rightleftharpoons}} S - H_4N_2O_4(ad) \xrightarrow{k_{f2}} 2\,H_2O + \frac{2}{3}\,NO_2 + \frac{2}{3}\,N_2O} \tag{2.70}$$

with the overall global reaction written as:

$$\mathrm{H_4N_2O_4 \rightarrow 2H_2O + \frac{2}{3}NO_2 + \frac{2}{3}N_2O} \tag{2.71}$$

The above global reaction neglects several reaction products of HAN decomposition (NH_3, NO, HNO_3, hydroxylamine) and includes the N_2O species which, while predicted by theory, was undetected in the experiments in Chambreau et al. [16]. Despite these approximations, the global reaction in Equation 2.71 was deemed sufficient for the reduced-order model to avoid the complexity of including a higher fidelity reaction mechanism.

In modeling the decomposition of H_2O_2, one set of chemistry coefficients was prescribed to fully define an overall volumetric decomposition reaction (A_{f2}, E_{f2}, N_s, K_1). In the HAN model, decomposition has been separated into thermal and catalytic decomposition defined by coefficient sets [$A_{f2,th}$, $E_{f2,th}$] and [$A_{f2,c}$, $E_{f2,c}$, N_s, K_1] respectively. In this case, the advancement parameter gradient becomes:

$$\frac{\mathrm{d}\lambda}{\mathrm{d}x} = \frac{\dot{V}}{u}\left(\dot{r}_c + \dot{r}_{th}\right) \tag{2.72}$$

$$\dot{r}_c = A_{f2,c} e^{-E_{f2,c}/\mathcal{R}T} N_s \frac{K_1 C^{(s)}_{\mathrm{H_4N_2O_4}}}{1 + K_1 C^{(s)}_{\mathrm{H_4N_2O_4}}} \tag{2.73}$$

$$\dot{r}_{th} = A_{f2,th} e^{-E_{f2,th}/\mathcal{R}T} C_{\mathrm{H_4N_2O_4}} \tag{2.74}$$

It is stated in Koopmans et al. [17] that the solid-liquid catalyst interaction surface area per unit volume A_{sl} must be multiplied with the preexponential factor in Equation 2.73 to convert from a surface reaction rate to a volumetric reaction rate. In the case that using such a factor in this model is necessary (when the units of $A_o = A_{f2}N_s$ are m/s), the solid-fluid interfacial surface area per unit volume between the catalytic surface and the fluid phases A_{sf} will be used in place of A_{sl}. The equation for A_{sf} is derived from the summation of the solid-liquid interfacial area and solid-gas interfacial area equations shown in Koopmans et al. [17] and can be found below in Equation 2.75.

$$A_{sf} = 4\tilde{\varepsilon}\frac{\pi(D/2)^2 L}{D_p} = \tilde{\varepsilon}\frac{\pi D^2 L}{D_p} \tag{2.75}$$

For the purposes of this model, a surface reaction rate to volumetric reaction rate conversion parameter is not necessary as the units of the preexponential factor found in literature already result in a volumetric reaction rate. Tuning parameter values used will be shown in a later section. Similar to the H_2O_2 model, the N_s and $A_{f2,c}$ are a coupled set of tuning parameters and thus functionally act as one.

Further deviation from the H_2O_2 model occurs in the pressure gradient in Equation 2.69. The pressure model implemented in the referenced equation is the Ergun model which is not suitable for use with the low bed-to-pellet diameter ratio geometry found in both the Pasini et al. [9] and Jung et al. [10] catalyst beds. For $D/D_p < 40$, wall effects become a non-negligble source of drag on the flow in the bed [12]. For this reason, in addition to predicted violation of the Reynolds number constraints, the Ergun model was replaced with that presented in Cheng [18] which is designed to more accurately predict pressure drops through packed beds with low bed-to-pellet diameter ratios. Pressure drop across the bed

takes the same form but with empirically-based geometry-dependent coefficients:

$$\frac{\mathrm{d}p_{\mathrm{loss}}}{\mathrm{d}x} = \left(c_1 \left[\frac{1-\tilde{\varepsilon}}{Re_p} \right]^{c_2} + c_3 \right) \frac{1-\tilde{\varepsilon}}{\tilde{\varepsilon}^3} \frac{\rho u^2}{D_p} \tag{2.76}$$

$$c_1 = \left[185 + 17 \frac{\tilde{\varepsilon}}{1-\tilde{\varepsilon}} \left(\frac{D}{D-D_p} \right)^2 \right] \frac{1}{M^2} \tag{2.77}$$

$$c_2 = 1 \tag{2.78}$$

$$c_3 = \left[1.3 \left(\frac{1-\tilde{\varepsilon}}{\tilde{\varepsilon}} \right)^{1/3} + 0.03 \left(\frac{D}{D-D_p} \right)^2 \right] \frac{1}{M} \tag{2.79}$$

$$\text{where} \quad M = 1 + \frac{2}{3} \left(\frac{1}{1-\tilde{\varepsilon}} \right) \frac{D_p}{D} \tag{2.80}$$

2.1.3 Heat Transfer Model

An effort was made to expand upon the heat transfer capabilities of the catalyst bed model as the model described in Pasini et al. [9] is entirely adiabatic. The model at hand has the capability of including 1D radial heat transfer and may be applied to both the H_2O_2 and HAN-H_2O models. The domain can be split into cells centered on each node (with half-sized cells on the initial and terminal nodes) as shown in Figure 2.2.

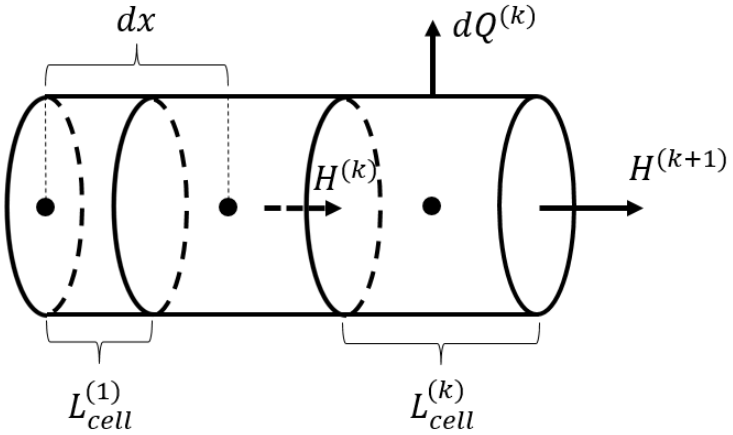

Figure 2.2: Domain Diagram with Energy Balance of Cell k

The temperature at an arbitrary node k is defined by the enthalpy of the fluid element within the cell k as seen in Equation 2.81.

$$T^{(k)} = T^{(k)}(H^{(k)}) \tag{2.81}$$

The differential heat lost or gained by cell k is dependent on the heat rate as a function of temperature as well as the fluid residence time within the cell as in Equations 2.82 and 2.83. Enthalpy of cell $k+1$ is then computed using conservation of energy within cell k to account for energy lost or gained through radial heat transfer as shown in Figure 2.2 and Equation 2.84.

$$q^{(k)} = q^{(k)}(T^{(k)}) \tag{2.82}$$

$$\mathrm{d}Q^{(k)} = q^{(k)}\mathrm{d}t^{(k)} \quad \text{where} \quad \mathrm{d}t^{(k)} = L_{cell}^{(k)}/u^{(k)} \tag{2.83}$$

$$H^{(k+1)} = H^{(k)} - \mathrm{d}Q^{(k)} \tag{2.84}$$

Heat transfer is modeled as conduction through a 2-layer wall with radiation and natural convection taking place at the external surface as can be seen in Figure 2.3 with the corresponding thermal circuit seen in Figure 2.4. Finding an appropriate convection correlation proved quite difficult so the Nusselt number correlation for free convection over a long, horizontal cylinder from Incropera et al. [19] was used despite violating the assumption of the cylinder being long. Properties of air are taken at the film temperature at each x-location. Contact resistance between the different material layers 1 and 2 in the wall is neglected. Additionally, it is assumed that there is perfect convection at the internal surface of catalyst bed and that the temperature at the wall is equal to that calculated for the fluid at each node.

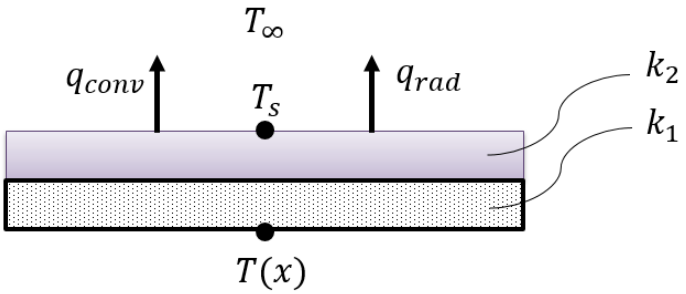

Figure 2.3: Radial Heat Transfer Physical Diagram

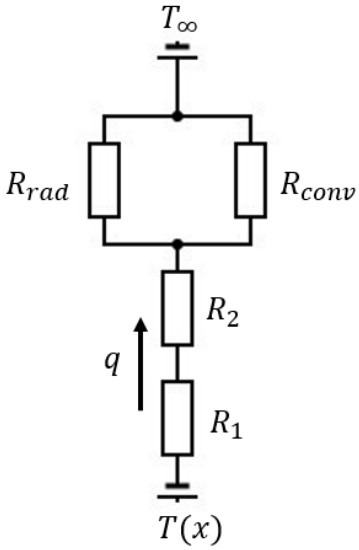

Figure 2.4: Radial Heat Transfer Thermal Circuit

Heat transfer in the axial direction, which would likely have the greatest impact on energy of the system, is incapable of being computed due to the sequential determination of fluid properties along the x-direction. In other words, the temperatures at each node are not solved simultaneously and thus each $T^{(k)}$ is solved in sequential order starting with $T^{(0)}$ at $x = 0$. Similarly, all other fluid properties are solved in the same manner. Therefore, $T^{(k+1)}$ is always unknown when solving for $T^{(k)}$ and the heat transfer between cells k and $k + 1$ cannot be calculated. A diagram showing qualitative heat transfer in the catalyst bed can be seen in Figure 2.5 with red arrows showing the direction of heat flux. The diagram assumes that $T_\infty < T_i < T_f$ which is a reasonable assumption for a majority of operational cases.

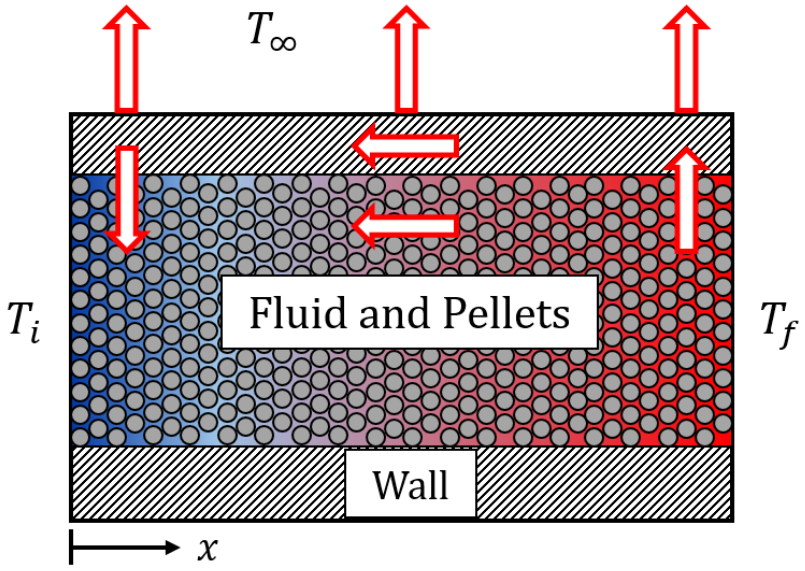

Figure 2.5: Qualitative Heat Transfer Pathway in Catalyst Bed

Due to the application of monopropellant thrusters in space propulsion, experiments may be run with an insulated thruster to prevent convection from taking place on the external surface and thus better replicate the in-space environment. In this case, the thermal circuit should be modified to have an insulated condition in place of natural convection and radiation.

2.2 Benchmarks for Validation

2.2.1 H_2O_2 Model Validation

Original validation of the model by Pasini et al. was performed by comparing the model predicted pressure and temperature at the exit of the catalyst bed to experimental data which yielded good agreement. Tuning parameters $\tilde{\varepsilon}$ and E_{f2} yielded physically realistic values as well, further supporting the validity of the model. Yet more validation for the model was attained through comparison of predicted temperature and pressure to experimental data at several locations along the length of the catalyst bed for various test cases by Jung et al. [10]. For each test condition, the pressure and temperature data at each x-location is

the average of multiple tests at that condition. Each test case shows good agreement in temperature with more significant deviations in pressure. Because of the variation in both location of data acquisition and catalyst bed test condition, the Jung et al. cases were chosen to validate the code for the model described above.

Geometric inputs taken from Jung et al. can be found in Table 2.2.

D (cm)	L (cm)	D_p (cm)	$\tilde{\varepsilon}$
2.9	2.94	0.159	0.394

Table 2.2: Catalyst Bed Geometry

The value for D_p was determined by taking the average pellet diameter for 10-16 mesh (pellet diameters ranging from 0.118 - 0.2 cm) [10]. Porosity $\tilde{\varepsilon}$ is computed using Equation 2.46. If one refers to Table 2.1, it can be seen that this value of porosity violates the assumptions for using the Ergun model. Test cases are defined by the values of the input conditions for the experiment with the exception of the Large Bed case which implemented a different catalyst bed geometry. Conditions for each test case are shown in Table 2.3. Each test case analyzed in this study uses the same mesh size and initial temperature T_i of 300 K. Initial pressure p_i was not explicitly stated in Jung et al. but was taken from the plots provided.

	Test Case	$\dot{m}$ (kg/s)	Y	p_i (bar)	L (cm)	D (cm)
(1)	Standard	0.067	0.9	25.3	2.94	2.9
(2)	Large Bed	0.067	0.9	12.7	3.3	4.58
(3)	Low Concentration	0.067	0.8	19.9	2.94	2.9
(4)	High Concentration	0.067	0.95	28.0	2.94	2.9
(5)	Low Mass Flow Rate	0.0335	0.9	14.0	2.94	2.9
(6)	High Mass Flow Rate	0.0938	0.9	31.8	2.94	2.9

Table 2.3: Selection of Experimental Conditions from Jung et al. [10]

The following series of figures shows the temperature and pressure profiles generated by the code written for this study compared to the model and experimental data generated by Jung et al. for the first 5 test cases. The blue and red dotted vertical lines demarcate the transitions from Region I to II and Region II to III respectively. Figures 2.6 and 2.7 show the standard test case axial temperature profile with labeled regions and axial pressure profile respectively. Region I is characterized by rapid temperature increase to the boiling condition followed by quasi-isothermal vaporization in Region II. Finally, the gas mixture exhibits asymptotic temperature increase to the complete decomposition temperature in Region III.

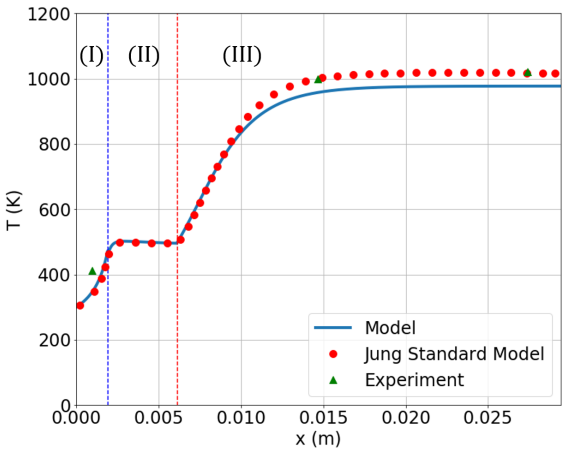

Figure 2.6: Standard Test Case Temperature Profile

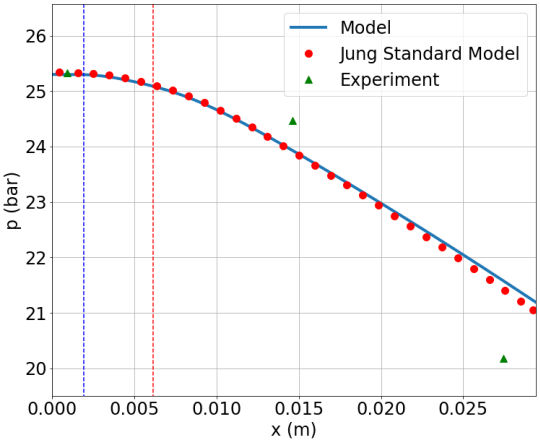

Figure 2.7: Standard Test Case Pressure Profile

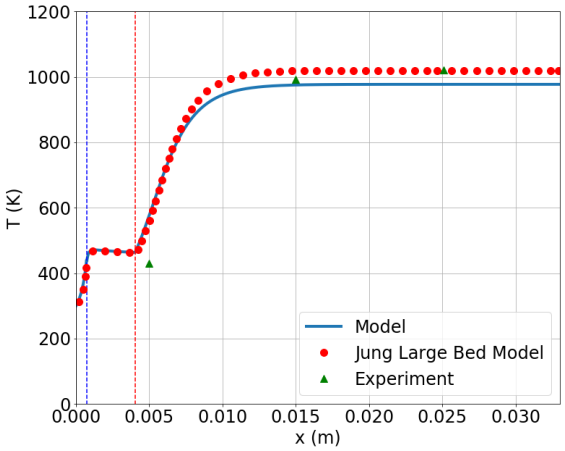

Figure 2.8: Large Bed Test Case Temperature Profile

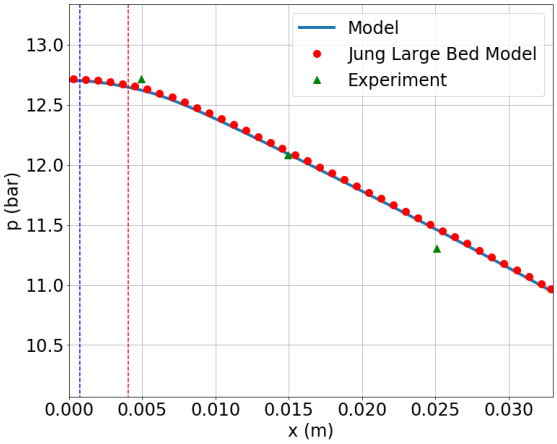

Figure 2.9: Large Bed Test Case Pressure Profile

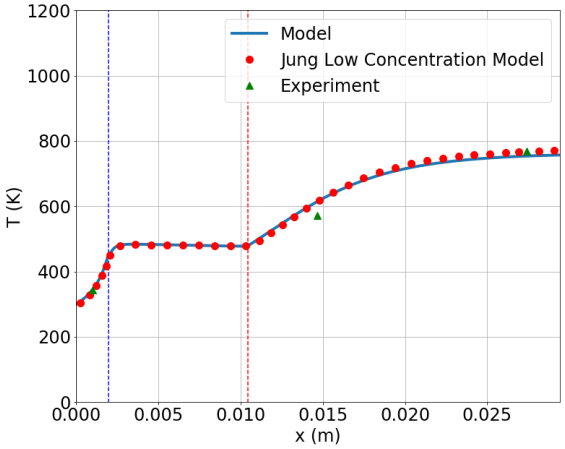

Figure 2.10: Low Concentration Test Case Temperature Profile

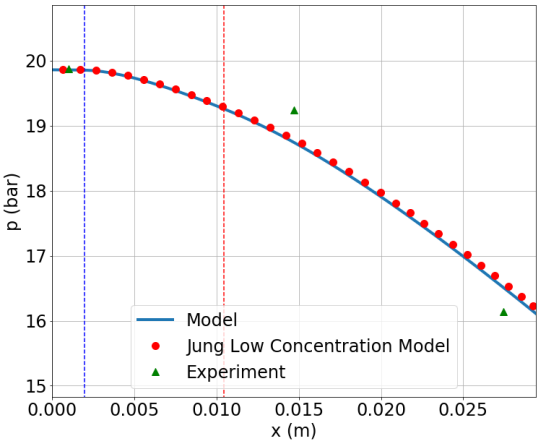

Figure 2.11: Low Concentration Test Case Pressure Profile

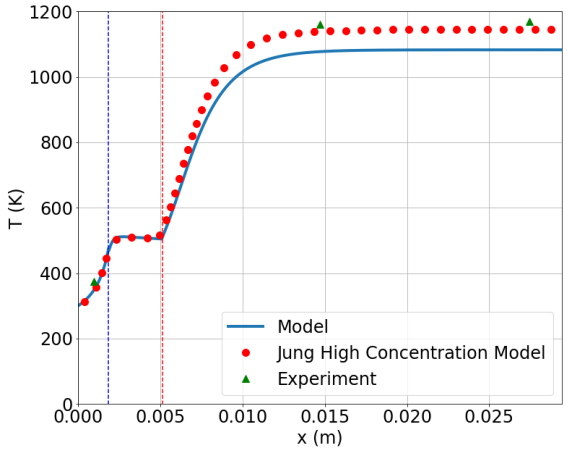

Figure 2.12: High Concentration Test Case Temperature Profile

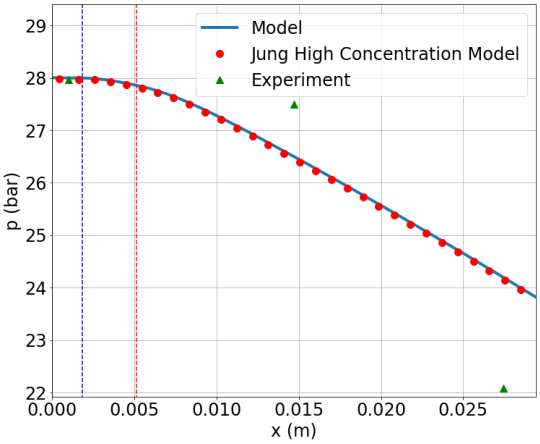

Figure 2.13: High Concentration Test Case Pressure Profile

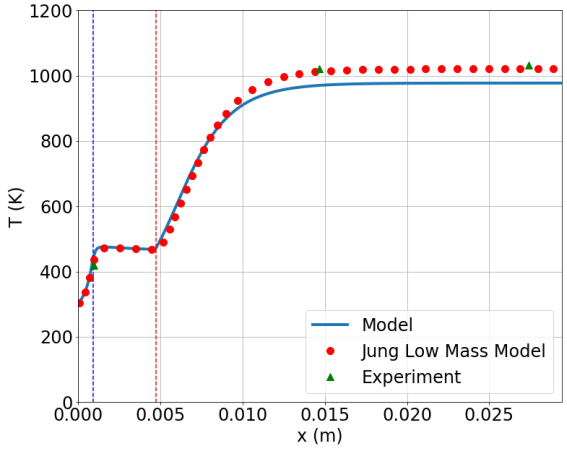

Figure 2.14: Low Mass Flow Rate Test Case Temperature Profile

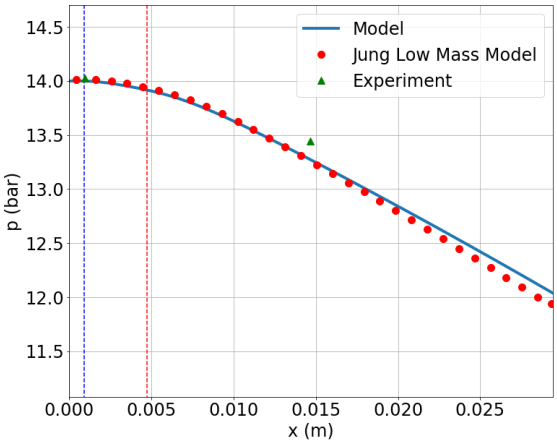

Figure 2.15: Low Mass Flow Rate Test Case Pressure Profile

It can be seen in the figures above that the model created for this study agrees reasonably well with that shown in Jung et al. although each test case exhibits minor deviations, particularly in the temperature value at the end of the catalyst bed. This phenomenon persists even if the heat transfer model is removed to restore a fully adiabatic model. Final

temperature for the Jung et al. model was stated to be 1020 K for the standard case, equal to the adiabatic decomposition temperature for the 90% H_2O_2 mixture. For the standard case, this study's model yielded a temperature of 977 K for both the final temperature and the direct computation of the adiabatic decomposition temperature as shown in Equation 2.88. Due to the temperature dependence of $c_{p,s}$, a nonlinear solver is still required to obtain the adiabatic decomposition temperature T_{ad}.

$$\dot{n}_{\mathrm{H_2O_2}} h_{\mathrm{H_2O_2}} + \dot{n}_{\mathrm{H_2O}} h_{\mathrm{H_2O}} + \dot{n}_{\mathrm{O_2}} h_{\mathrm{O_2}} = H_o - \Delta Q \tag{2.85}$$

$$\text{where} \quad \dot{n}_{\mathrm{H_2O_2}} = 0,\ \dot{n}_{\mathrm{H_2O}} = \dot{n}^{(i)}_{\mathrm{H_2O_2}},\ \dot{n}_{\mathrm{O_2}} = \frac{1}{2}\dot{n}^{(i)}_{\mathrm{H_2O_2}},\ \Delta Q = 0,\ \epsilon = 1 \tag{2.86}$$

$$\begin{aligned} &\dot{n}^{(i)}_{\mathrm{H_2O_2}} \left[h_{\mathrm{H_2O}} + \frac{1}{2} h_{\mathrm{O_2}} \right] = \\ &\dot{n}^{(i)}_{\mathrm{H_2O_2}} \left[h^{\circ}_{\mathrm{H_2O_2},(l)} + c_{p\mathrm{H_2O_2},(l)} (T_i - T^{\circ}) \right] + \dot{n}^{(i)}_{\mathrm{H_2O}} \left[h^{\circ}_{\mathrm{H_2O},(l)} + c_{p\mathrm{H_2O},(l)} (T_i - T^{\circ}) \right] \end{aligned} \tag{2.87}$$

$$\begin{aligned} &\dot{n}^{(i)}_{\mathrm{H_2O_2}} \left[h^{\circ}_{\mathrm{H_2O},(g)} + c_{p\mathrm{H_2O},(g)} (T_{ad} - T^{\circ}) + \frac{1}{2} h^{\circ}_{\mathrm{O_2}} + \frac{1}{2} c_{p\mathrm{O_2}} (T_{ad} - T^{\circ}) \right] \\ &= \dot{n}^{(i)}_{\mathrm{H_2O_2}} \left[h^{\circ}_{\mathrm{H_2O_2},(l)} + c_{p\mathrm{H_2O_2},(l)} (T_i - T^{\circ}) \right] + \dot{n}^{(i)}_{\mathrm{H_2O}} \left[h^{\circ}_{\mathrm{H_2O},(l)} + c_{p\mathrm{H_2O},(l)} (T_i - T^{\circ}) \right] \end{aligned} \tag{2.88}$$

Due to the consistent offset in the temperatures, this is believed to be due to a difference in the values of the reference enthalpies between this study and Jung et al. Additionally, the temperature discrepancy is small in magnitude for the low concentration test case. This is to be expected as lowering the concentration of H_2O_2 is essentially reduces the energy concentration of the flow thereby reducing the decomposition temperature, reaction rate, and percentage final reaction advancement. By making minor modifications ($\lessapprox 3\%$) to the reference enthalpies, the model in this study is capable of matching that of Jung et al. nearly exactly. Despite the better matching capabilities, the modified reference enthalpies will not be implemented in this study and the difference between the models will be attributed to variations in thermochemical data.

It should be noted that in the high mass flow rate test case the model at hand exhibits poor agreement regardless of the enthalpies used while Jung et al. agrees well with the experimental data. This can be seen in Figures 2.16 and 2.17.

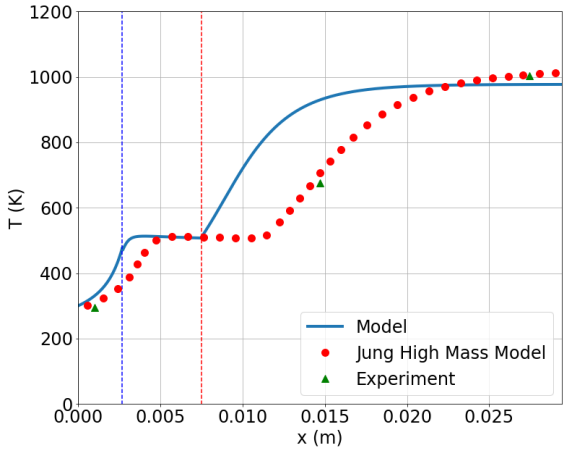

Figure 2.16: High Mass Flow Rate Test Case Temperature Profile

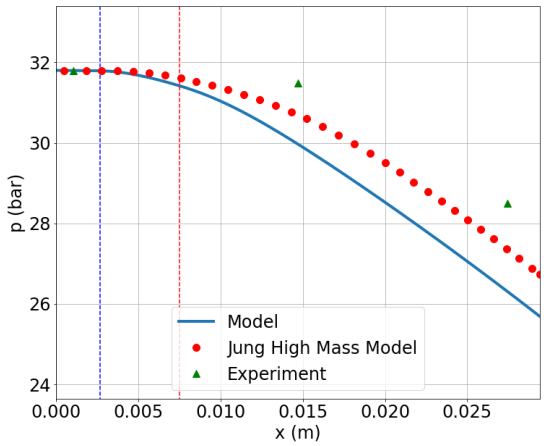

Figure 2.17: High Mass Flow Rate Test Case Pressure Profile

The origin of the deviation between the results of the two models for the high mass flow rate case is unknown. The model used in this study exhibits a significantly greater reaction rate than the Jung et al. model as indicated by the more rapid increase in the axial temperature profile in Regions I and III as well as a shorter Region II. It was discovered by trial-and-error that good agreement in both the axial temperature and pressure profiles between the two models could be achieved by decreasing the reaction rate through a 33% reduction to the advancement parameter gradient for the model at hand. Due to the good agreement with the other 5 test cases, the model in this study has been deemed sufficiently validated.

Initial determination of the tuning parameters was performed by minimizing the nondimensional error between the temperature and pressure profiles generated by the model and Jung et al. for a 3D parameter sweep in N_s, K_1, and E_{f2}. This was done by finding each x-location closest to that of the points taken from the Jung et al. model data and determining the error as follows:

$$\text{error} = \frac{\|x_{\text{expected}} - x_{\text{predicted}}\|}{\|x_{\text{expected}}\|} \tag{2.89}$$

where the quantity x is either T or p. The Jung et al. values are treated as expected values and the predicted values are generated by the model at hand. The final error values for a set of input parameters was determined by using trapezoidal integration on the calculated relative errors. Error surfaces in T and p with each surface representing a different activation energy value can be seen in Figures 2.18 and 2.19.

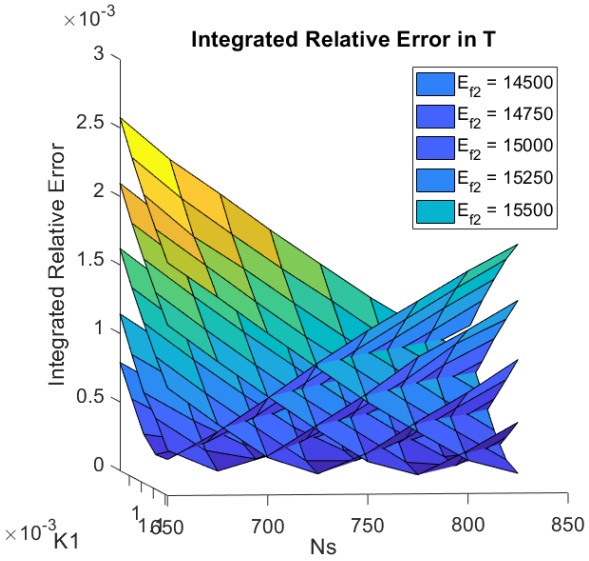

Figure 2.18: Integrated Relative Error in T for Standard Case

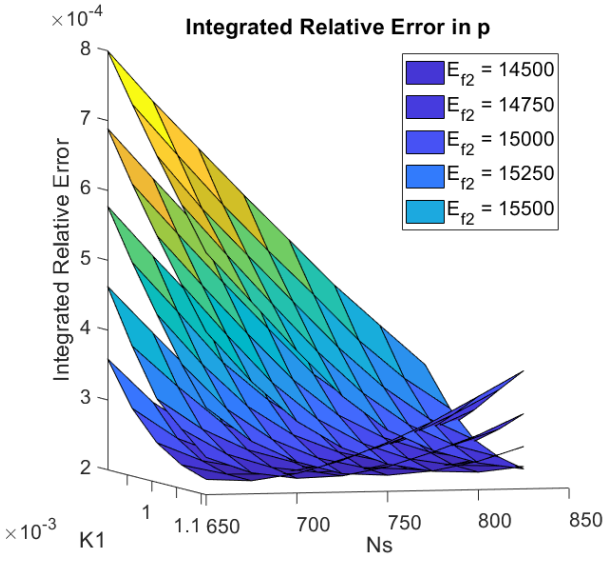

Figure 2.19: Integrated Relative Error in p for Standard Case

A comparison between the values used in Jung et al. and this study can be seen in Table 2.4.

Parameter	Jung et al. [10]	Model
A_{specific}	21.9934	21.9934
E_{f2} (J/mol)	15000	14900
N_s (m^{-3})	1000*	780
K_1 (m^3/mol)	0.001*	0.00104

Table 2.4: Comparison of Tuning Parameters from Jung et al. [10] for H_2O_2 Model

Values marked with an "*" indicate that a scaling based on a unit transformation was

performed. The units of N_s and K_1 were not explicitly stated in Jung et al. but it is assumed that they were L^{-1} and L/mol respectively. Another potential source of the unit discrepancy could be that N_s is in fact measured in m^{-3} but the advancement parameter gradient in Jung et al. is measured in mol/s·mm as opposed to mol/s·m. The greatest deviation occurs in N_s which is likely due to the error minimization favoring a solution with a faster reaction rate in order to compensate for the lower reference enthalpy values used.

2.2.2 HAN-H_2O Model Validation

Similar data for validation of the HAN-H_2O model was not available and thus proper validation of the model and tuning of the chemistry parameters was not possible. As a consequence, available chemistry parameters values were taken from literature and the remaining parameters were adjusted to generate a physically reasonable temperature profile. Values were taken from a study conducted by Esparza et al. [20] in which thermogravimetric analysis (TGA) and differential scanning calorimetry (DSC) were used to determine the catalytic and thermal decomposition preexponential factors and activation energies for an aqueous HAN solution. Values implemented in the model and as reported in Esparza et al. are shown in Table 2.5. Thermal decomposition parameters used were determined by DSC while the catalytic parameters were determined using TGA. Parameters with "**" are not taken from literature but tuned "by eye". Not all requisite thermophysical data, such as viscosity and reference enthalpy in the gas phase, was available for HAN. Additionally, as an ionic liquid, the vapor pressure of HAN is very low [3]. Therefore, the model used in this study may not be sufficient in modeling the decomposition of HAN in the catalyst due to the strong dependence on species vapor pressures when assessing the flow's operational region. This is especially true considering that specific reaction mechanisms and mixture behaviors may be unaccounted for. Esparza et al. [20] notes that for low heating rates, H_2O in the mixture was vaporized prior to the onset of decomposition which indicates that the mixture model may not be a sufficient representation of this system.

Parameter	Esparza et al. [20]	Model
$A_{f2,th}$ (1/s)	$3.55 \cdot 10^3$	$3.55 \cdot 10^3$
$E_{f2,th}$ (kJ/mol)	57.5 ± 3.5	54.0
$A_{f2,c}$ (1/s)	$3.31 \cdot 10^5$	$3.31 \cdot 10^5$
$E_{f2,c}$ (kJ/mol)	63.9 ± 2.5	61.4
K_1** (m^3/mol)	–	0.0104
N_s** (m^{-3})	–	85

Table 2.5: Tuning Parameters for HAN-H_2O Model

In the current version of the HAN-H_2O model, the total pressure p is computed as follows:

$$p = p_{H_2O,(g)} + p_{N_2O} + p_{NO_2} \tag{2.90}$$

It should be noted that there is no term for HAN as it is assumed that $p_{sat,\mathrm{HAN}} \approx 0$ due to its low vapor pressure although this neglects the gas phase contribution of HAN as well. Previous studies have indicated that HAN-H_2O mixture propellants require catalyst bed preheating temperatures ranging from 300° to 400° Celsius [21]. Catalyst bed preheating in the model at hand is emulated using the initial mixture temperature. An initial temperature of $T_i = 673$ K was used to generate the plot see in Figure 2.20.

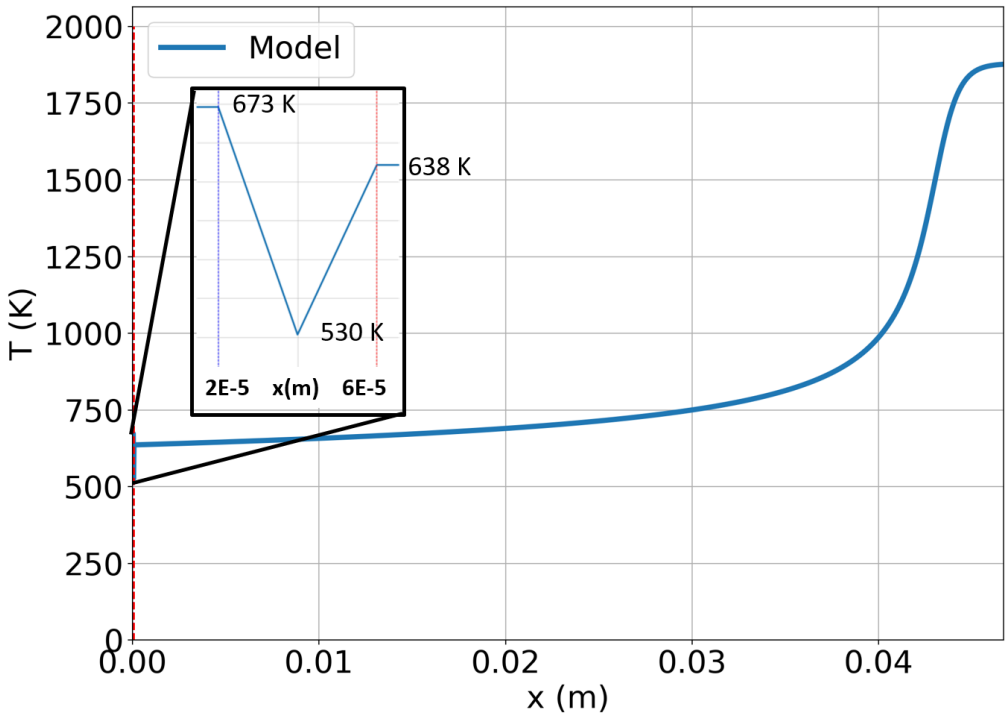

Figure 2.20: $Y = 80\%$ HAN-H_2O Mixture Temperature Profile with Magnification on Discontinuity

As one can see in Figure 2.20, Regions I and II collapse into the first few spatial nodes. This is because the initial temperature is significantly higher than the boiling temperature for the mixture at the initial conditions. This causes the model to jump from Region I to Region II in the first node. Then immediately following this step, the evaporation parameter ϵ jumps to 1 thereby initiating Region III in which the flow remains until the terminal node. Without an alternate set of equations for determining the evaporation parameter and mixture temperature, there is no apparent way to resolve the large discontinuity at the beginning of the simulation with the given material properties.

2.3 Additional Model Results

Several additional model outputs from the standard test case will be shown in this section. Figure 2.21 contains a plot of the axial profile of the reaction advancement parameter λ or the molar flow rate of H_2O_2 consumed. The parameter is normalized to the initial molar flow rate of H_2O_2 to show the percentage of reaction completion.

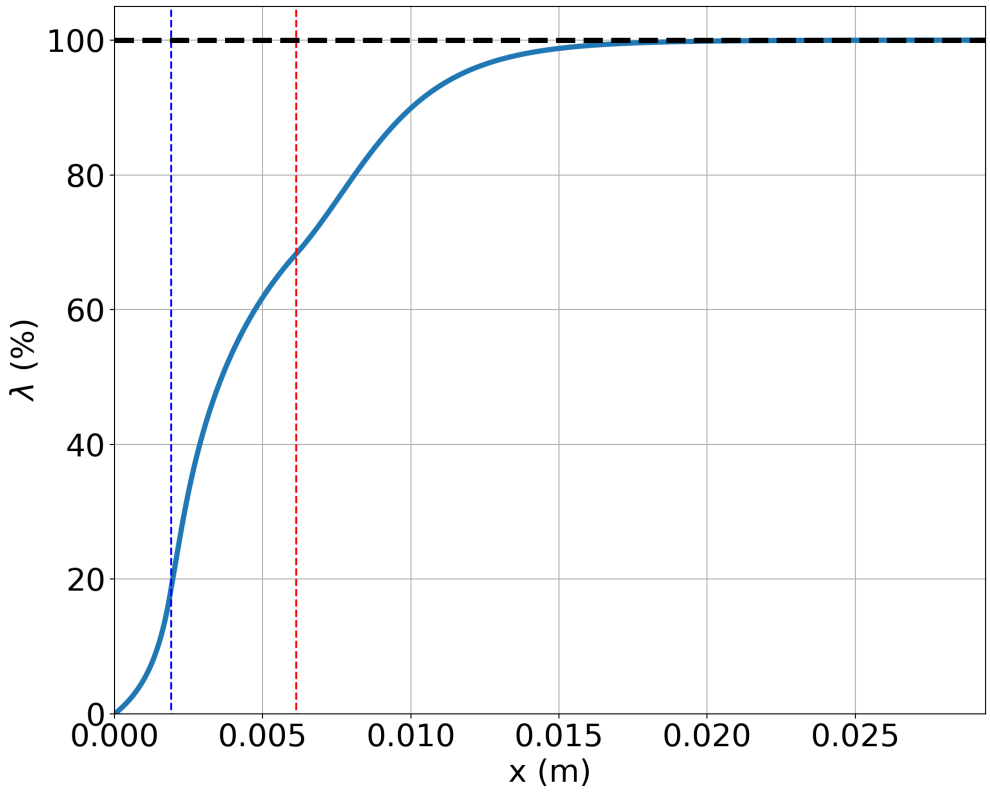

Figure 2.21: Axial Profile of Reaction Advancement Parameter for Standard Case

As a fluid element traverses the catalyst bed, the reaction advancement parameter asymptotically approaches 100%, as marked by the black dotted line.

It is also possible to observe the species and mixture concentrations as functions of axial distance from the catalyst bed inlet. Concentration profiles can be seen in Figure 2.22 with

a magnified view of the concentrations at the transition between Regions I and II in Figure 2.23.

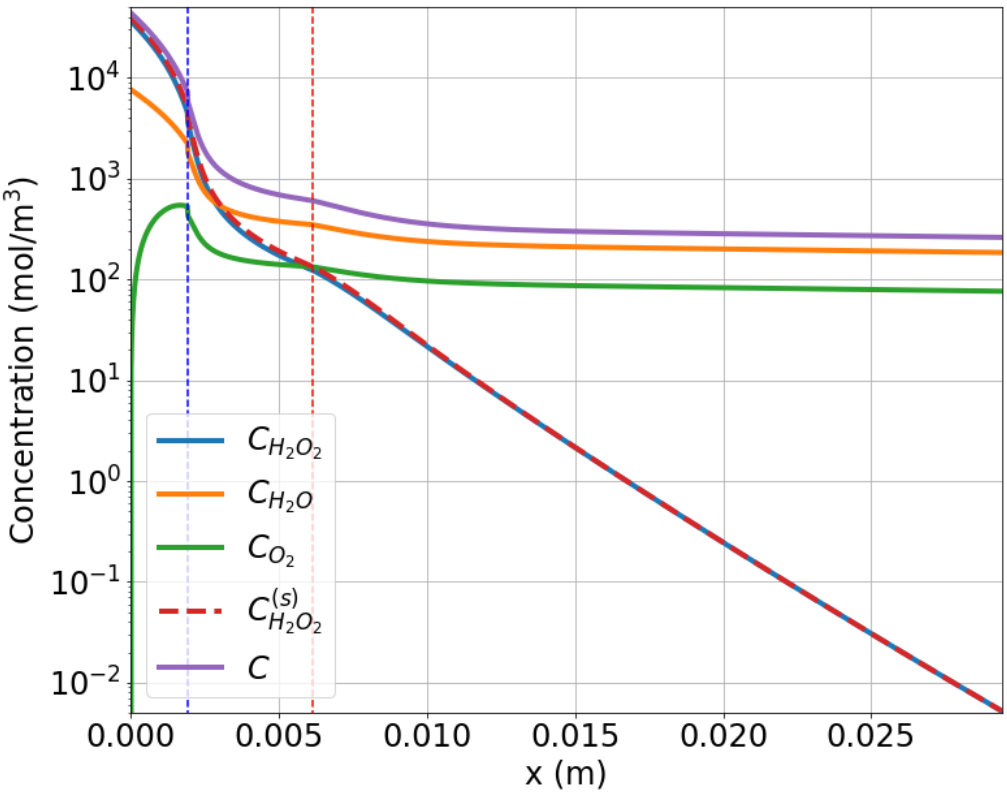

Figure 2.22: Axial Profile for Species and Mixture Concentrations

It can be seen in Figure 2.22 that the concentrations of H_2O_2 in the bulk mixture flow and at the catalytic surface are nearly identical and follow the same evolutionary trends. Almost immediately after the transition to Region III (demarcated by the red, dotted line), the concentrations of H_2O and O_2 become roughly constant while the concentration of H_2O_2 exhibits a logarithmic decrease. This is due to the stabilization of the volumetric flow rate and logarithmic decrease of the H_2O_2 concentration at the catalytic surface. Assuming a constant T and u, that the bulk flow and catalytic surface concentrations of H_2O_2 are equal,

and noting that:

$$\frac{K_1 C^{(s)}_{\mathrm{H_2O_2}}}{1 + K_1 C^{(s)}_{\mathrm{H_2O_2}}} \approx K_1 C^{(s)}_{\mathrm{H_2O_2}} \quad \text{for} \quad K_1 C^{(s)}_{\mathrm{H_2O_2}} \ll 1$$

the following proportionality can be found by substituting $\lambda = -\dot{n}_{\mathrm{H_2O_2}}$:

$$\frac{\mathrm{d}C_{\mathrm{H_2O_2}}}{\mathrm{d}x} \propto -C_{\mathrm{H_2O_2}} \tag{2.91}$$

The above proportionality is approximately true for a majority of Region III for the standard case.

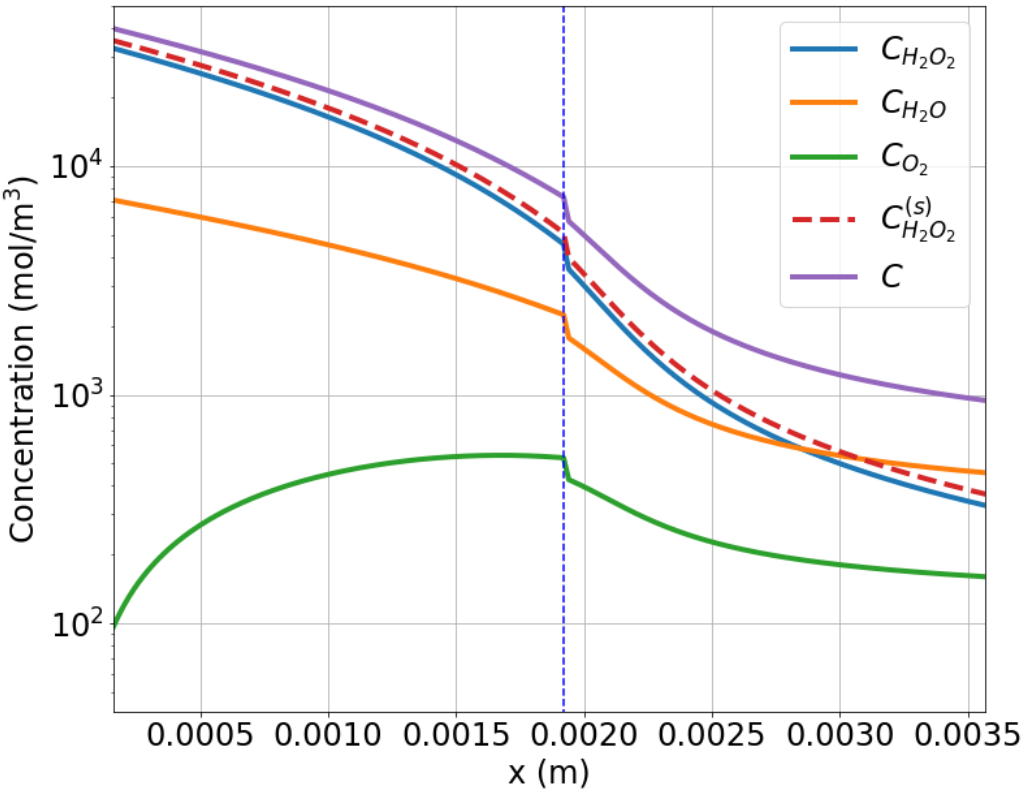

Figure 2.23: Axial Profile for Species and Mixture Concentrations with Magnification at Region Transition

Figure 2.23 shows the transition between Regions I and II and the resulting discontinuity in species concentrations. This is due to the sudden increase in the evaporation parameter

which directly results in an increase in the volumetric flow rate which appears in the denominator of the concentration equation.

While it has already been shown that the simulation violates the assumptions of the Ergun model on the basis of porosity, it can also be seen that the Reynolds number limit of 2300 is exceeded by nearly an order of magnitude.

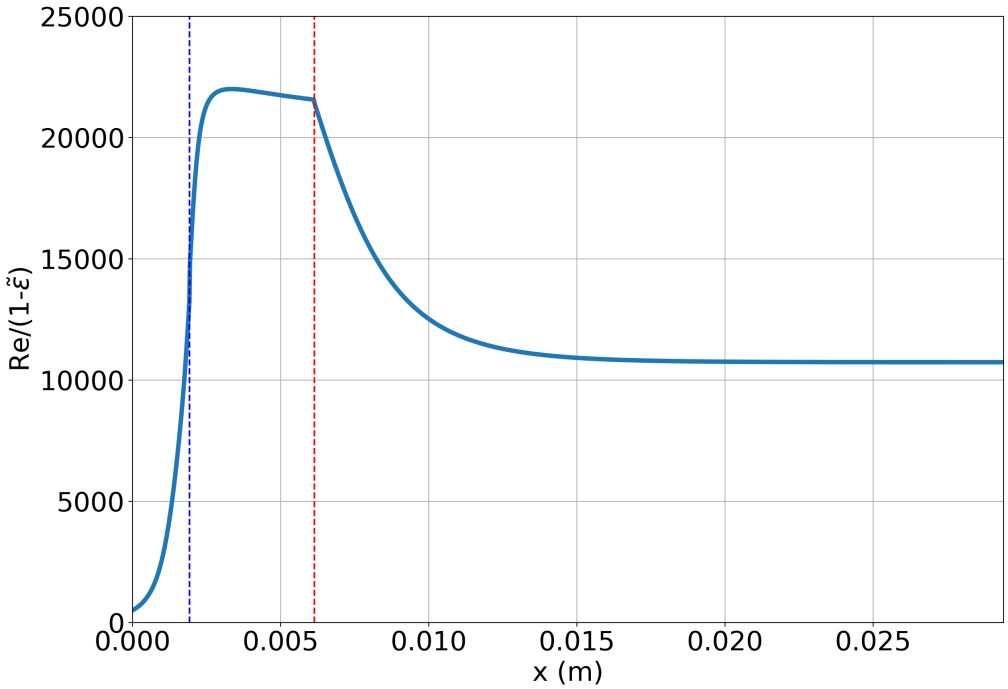

Figure 2.24: Axial Profile of Re^* for Standard Case

By observing the relevant heat transfer quantities, the effects of the current heat transfer model can be assessed and the importance of including the model can be evaluated. A plot containing the axial profiles of enthalpy loss rate, differential time (or residence time of a fluid element within a cell), and the different enthalpy lost from each cell can be seen below.

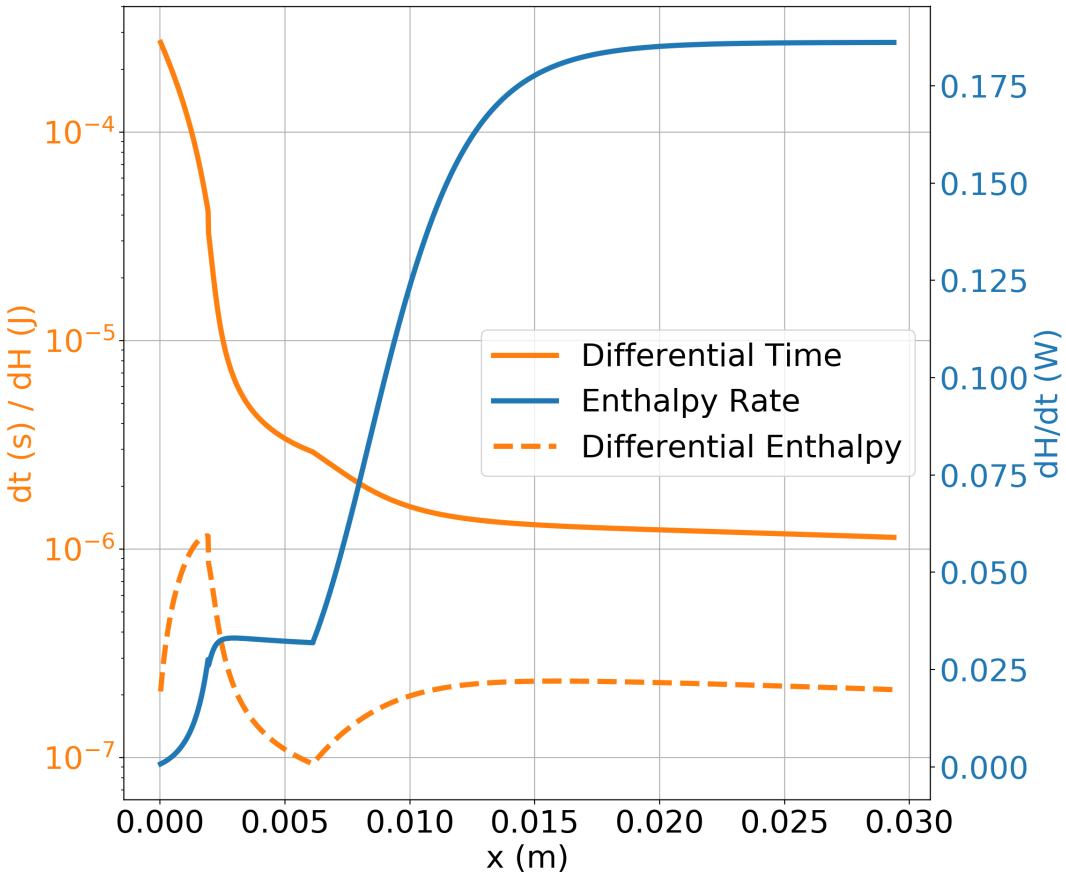

Figure 2.25: Axial Profiles of Heat Transfer Quantities

The total enthalpy loss from the system is $\Delta H = 3.64$ mJ and the total residence time of a fluid element within the catalyst bed is 16.7 ms. With the current configuration of the heat transfer model, the enthalpy loss of the system is negligible and it would suffice to assume that the catalyst bed is adiabatic. One reason for the negligible enthalpy loss from the system is that residence time within a cell decreases with x while the enthalpy loss rate increases. The majority of the residence time within the catalyst bed occurs when heat transfer rates are very small. Because of the insignificance of the enthalpy loss, the heat transfer model is not used for a majority of the non-deterministic analyses performed on the overall model.

Once again, radial heat transfer is not expected to be the most influential form of heat

transfer in the system but axial heat transfer was not capable with the solution methodology at hand. An attempt was made to approximate steady axial heat transfer by solving for the axial temperature profile and then computing the uniform outer surface temperature T_s that would satisfy conservation of energy of the system i.e. $H_{in} = H_{out} + \Delta Q$. In doing so, the expected heat transfer phenomena were observed. Enthalpy was entering the fluid from the walls near the inlet where fluid temperatures were low and exiting from the fluid to the walls near the outlet where temperatures were high. Additionally, heat transfer to the environment occurred for the entire length of the catalyst bed. While this heat transfer model approximated the expected phenomena, the effects on the flow properties were still negligible and successive iterations of the simulation were required making the process more computationally expensive.

CHAPTER 3

Non-Deterministic Analysis

3.1 Justification for Various Approaches

Due the complex nature of the monopropellant catalyst bed system, the outputs of interest exhibit nonlinear relationships with the controllable inputs, even when analyzed with a reduced-order model. Additionally, due to the variability in material property data, it is critical to understand the model's sensitivity to thermophysical and thermochemical inputs as well as the impact that uncertainty in these properties has on the quantities of interest (QOI). Attempting to quantify the system behavior using a safety factor-based analysis may result in the establishment of erroneous bounds on the QOIs. Imposing deterministic input boundaries without investigating the intermediate domain also prohibits understanding any, potentially counter-intuitive, intermediate behavior of the system and its outputs. For this reason, it is essential to implement some form of non-deterministic analysis. It should be noted that in this context a non-deterministic analysis does not imply that the model being studied is not defined by a deterministic algorithm, instead it implies that uncertainty in model inputs can be emulated by randomly sampling values from a defined distribution.

Uncertainty quantification (UQ) techniques were used in this study to gain a better understanding of system behavior through the spread and skew in QOI distributions for uncertain inputs. Having a deeper understanding of system sensitivity to the inputs facilitates the design of higher-fidelity models and better performing thrusters while analyzing the QOI distributions allows for better quantification of thruster performance by providing thrust and specific impulse envelopes. Additionally, this study implements polynomial chaos expansion (PCE) as a method for generating a sufficiently accurate and efficient surrogate model in

order to reduce computational time associated with all forms of non-deterministic analyses performed. Sensitivity analysis was performed on a global scale using variance-based decomposition allowing for the procedural quantification of sensitivities that were previously only quantitatively observed. Bayesian inference was used to generate confidence intervals for tuning parameters and QOI based on available experimental data and fabricated mock data.

3.2 Uncertainty Quantification Theory

Uncertainty quantification in this study was conducted primarily through observing QOI distributions in histograms or by demarcating some percentage of samples away from the median in axial property profiles. This was done for various sets of input variables such as physical inputs that may be varied in experiment or thermochemical data in the model. There is no explicit underlying theory for the QOI distributions generated in this study. Input variables were assigned uncertain distributions and QOI distributions were a result of sampling the model or a surrogate model. Sampling techniques used will be discussed later in the thesis.

PCE is a type of stochastic expansion that utilizes multivariate orthogonal polynomial bases to form a surrogate model. This method creates a functional relationship between system response functions and a set of random input variables. The form of the polynomial relationship is dependent on the input distributions with linkages between the two based on the Askey scheme [22].

The generalized form of PCE begins with the chaos expansion of the response function R as follows:

$$R = a_0 B_0 + \sum_{i_1=1}^{\infty} a_{i_1} B_1(\xi_{i_1}) + \sum_{i_1=1}^{\infty} \sum_{i_2=1}^{i_1} a_{i_1 i_2} B_2(\xi_{i_1}, \xi_{i_2}) + \sum_{i_1=1}^{\infty} \sum_{i_2=1}^{i_1} \sum_{i_3=1}^{i_2} a_{i_1 i_2 i_3} B_3(\xi_{i_1}, \xi_{i_2}, \xi_{i_3}) + ... \tag{3.1}$$

Each nested summation term above represents the term in the polynomial of order equal to the multiplicity of the nesting. The above chaos expansion can be simplified by converting

from order-based indexing to term-based indexing as seen below:

$$R = \sum_{j=0}^{\infty} \alpha_j \Psi_j(\boldsymbol{\xi}) \tag{3.2}$$

where summation over $a_{i_1 i_2 \ldots i_n}$ corresponds to α_j and summation over $B_n(\xi_{i_1}, \xi_{i_2}, ..., \xi_{i_n})$ corresponds to $\Psi_j(\boldsymbol{\xi})$. $\Psi_j(\boldsymbol{\xi})$ is a multivariate polynomial that contains products of the 1D orthogonal polynomial base terms and $\boldsymbol{\xi}$ is the random variable vector. Lastly, as one would expect when dealing with finite calculations, the expansion is truncated to order P as shown below:

$$R \cong \sum_{j=0}^{P} \alpha_j \Psi_j(\boldsymbol{\xi}) \tag{3.3}$$

In effect, this generates a multivariate polynomial approximation of the response function to random input variables.

3.3 Sensitivity Analysis Theory

Sensitivity analysis on the model was primarily performed through variance-based decomposition, otherwise known as Sobol inidices. Sobol indices compute the variance in a response function R for a given variable or combination of variables allowing for both direct effects and nonlinear combination effects to be observed. Sobol indices may be computed as main-effect indices or total-effect indices. The former is a measure of an input variable x_i's direct effect on the uncertainty in the response function whereas the latter is a measure of the variable's total effect on the response function uncertainty as it is a summation of the variable's direct effect and its nonlinear combination effect contributions. Both indices provide a quantitative measure of global sensitivity over the domain on interest. Equations 3.4 and 3.5 respectively contain the equations for the main-effect index S_i and total-effect index T_i as seen in the DAKOTA Theory Manual [22]. The derivations of these equations will not be shown in this

text but may be found in Tang et al. [23].

$$S_i = \frac{\mathrm{Var}_{x_i}[E(R|x_i)]}{\mathrm{Var}(R)} \tag{3.4}$$

$$T_i = \frac{E(\mathrm{Var}(R|x_{\sim i}))}{\mathrm{Var}(R)} = \frac{\mathrm{Var}(R) - \mathrm{Var}(E[R|x_{\sim i}])}{\mathrm{Var}(R)} \tag{3.5}$$

In the above equations, response function R is a function of m-dimensional input vector $\boldsymbol{x} = [x_1, ..., x_m]$ and $x_{\sim i} = (x_1, ..., x_{i-1}, x_{i+1}, ..., x_m)$ or all x except for x_i. It should also be noted that by definition $\sum_{i=1} S_i = 1$ while $\sum_{i=1} T_i \geq 1$. Methods for computing higher-order interaction indices are more involved and thus will not be shown in this text but may be found in Sobol [24].

3.4 Bayesian Inference Theory

Bayesian inference is a method for updating the probability of a hypothesis given the availability of new data. The cornerstone and namesake of Bayesian inference is Bayes' theorem, seen in Equation 3.6, which relates a new probability of interest to known probabilities.

$$\mathrm{prob}(X|Y, I) = \frac{\mathrm{prob}(Y|X, I) \cdot \mathrm{prob}(X|I)}{\mathrm{prob}(Y|I)} \tag{3.6}$$

For the context of the discussion regarding Bayesian inference, X is a hypothesis in the form of a set of input variables, Y is evidence or experimental data, and I represents additional conditions implicit within the model. The meaning of each term in Bayes' theorem is summarized in Table 3.1 [25]. Each term represents the probability of some argument given that another argument or set of arguments is true. For example, $\mathrm{prob}(A|B, C)$ is the probability of argument A given that both arguments B and C are true.

Term	Nomenclature	Definition
$\text{prob}(X\|Y,I)$	posterior probability	What is known given the data
$\text{prob}(X\|I)$	prior probability	What is known without the data
$\text{prob}(Y\|X,I)$	likelihood function	How well data matches hypothesis
$\text{prob}(Y\|I)$	marginal likelihood	Probability of data after marginalizing parameters

Table 3.1: Summary of Terms in Bayes' Theorem

In this study, Bayesian inference is used for the purposes of parameter estimation in which only the relative magnitudes of the posterior probabilities for each hypothesis are relevant. It can be seen in Equation 3.4 that marginal likelihood is independent of the hypothesis X and thus is constant for all values of X. Therefore, for the purposes of parameter estimation, the marginal likelihood can be neglected resulting in the following:

$$\text{prob}(X|Y,I) \propto \text{prob}(Y|X,I) \cdot \text{prob}(X|I) \tag{3.7}$$

Note that while the marginal likelihood can be neglected in the study at hand, the term is non-negligible when performing model comparison through Bayesian inference as the implicit conditions I will change between models.

The goal of this Bayesian analysis is to generate a distribution of posterior probabilities for a series of hypotheses. This is referred to as the posterior distribution. Additionally, there is an assumed distribution of prior probabilities or prior distribution. This can be based on previous knowledge or information regarding the system (e.g. having measured the weight of an object in a previous study, one may assume some Gaussian distribution based on the measurement and precision of the scale). Lastly, there is the likelihood function which is also evaluated for each hypothesis. Formulation of the likelihood function is determined by the user and may take many different forms, admittedly lending itself to some degree of subjectivity. Discussion of this subjectivity will take place later in the text.

Following the generation of the posterior, confidence intervals for both inputs and outputs can be determined. A confidence interval in the study at hand is defined as the set of

highest probability samples containing some fraction β of the integrated area of the posterior probability density function. Mathematically, this is written as:

$$\int_C \text{prob}(x)\text{d}x = \beta \int_a^b \text{prob}(x)\text{d}x \tag{3.8}$$

where C is the potentially discontinuous confidence interval. Limits a and b are the lower and upper bounds of the domain. For finite computations, the relation is as follows:

$$\sum_C \text{prob}(x_j)\Delta x_j = \beta \sum_{i=1}^{n} \text{prob}(x_i)\Delta x_i \tag{3.9}$$

If using random sampling, it may be further assumed that all Δx_i are approximately equal for all samples and thus:

$$\sum_C \text{prob}(x_j) = \beta \sum_{i=1}^{n} \text{prob}(x_i) \tag{3.10}$$

An example of the 50% confidence interval ($\beta = 0.5$) for a bimodal distribution can be seen in Figure 3.1. The blue shaded region is within the confidence interval while the bold dotted line indicates the maximum probability hypothesis, also know as the maximum likelihood estimate. It can be seen in Figure 3.1 that the confidence interval is capable of being discontinuous. While the example shown is for a one-dimensional input vector, the definition of confidence interval is equivalent for n-dimensional input vectors.

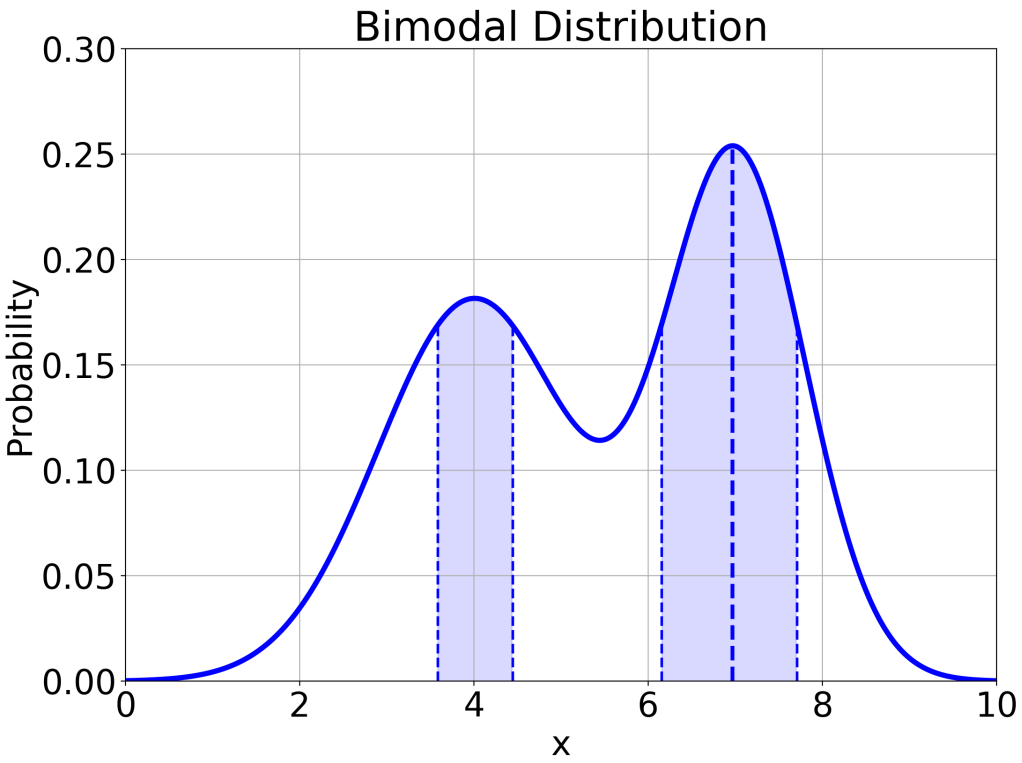

Figure 3.1: Example of 50% Confidence Interval for Bimodal Distribution

Confidence intervals for multidimensional posterior distributions computed through various means will be shown later in the text. While one can quantitatively observe the differences between these posterior distributions and their confidence intervals, it is desirable to have a quantitative measure of the difference. The quantitative difference between the distributions will be determined using the first Wasserstein metric, otherwise known as the Earth Mover's Distance (EMD). The EMD is a representation of the minimum cost of transforming a source distribution into a target distribution based on the distances between the distribution elements and their respective weights [26]. Define distributions $P = \{(p_1, w_{p1}), ..., (p_m, w_{pm})\})$ with m elements and $Q = \{(q_1, w_{q1}), ..., (q_n, w_{qn})\})$ with n elements where p_i and q_j are the respective cluster representatives and w_{pi} and w_{qj} are the cluster weights. Ground distance d_{ij} is the distance between between clusters p_i and q_j. Optimal transport is achieved by determining the flow f_{ij} between clusters p_i and q_j by

minimizing the following quantity subject to several constraints:

$$\sum_{i=1}^{m}\sum_{j=1}^{n} f_{ij}d_{ij} \tag{3.11}$$

The EMD is then determined by normalizing the same quantity by the total flow:

$$\mathrm{EMD}(P,Q) = \frac{\sum_{i=1}^{m}\sum_{j=1}^{n} f_{ij}d_{ij}}{\sum_{i=1}^{m}\sum_{j=1}^{n} f_{ij}} \tag{3.12}$$

EMD calculations in this study were conducted using the Python Optimal Transport library by Flamary and Courty [27].

3.5 Galaxy and DAKOTA Features

The bulk of the uncertainty quantification and sensitivity analysis performed in this study was done so using Galaxy Simulation Builder (GSB), a software that acts as a job coordinator and graphical user interface for DAKOTA (Design Analysis Kit for Optimization and Terascale Applications). Many of the implemented techniques are built-in to the program which greatly simplified execution of the analysis. Descriptions of some critical features within the program are given below.

GSB is capable of a wide variety of UQ techniques including generating response function PCEs. In preparing for analysis using PCE, several key parameters must be specified, namely the method of coefficient estimation and emulator samples. The method of coefficient estimation is dependent on the type of grid used to sample the high fidelity model and includes options such as tensor-product quadrature or Smolyak sparse grids [28]. Additionally, one must specify the order of estimation. In general, more sampling points are required for high order estimations. The emulator samples is the number of random input sets delivered to the PCE that has been trained on the high fidelity samples. Sample inputs used in the PCE are randomly sampled from the specified input distribution and each input variable may belong to a different type of distribution. The resulting evaluations are used for computing the Sobol indices if indicated to do so and can be output to a text file by GSB. Histograms can be generated simply by specifying bin bounds, referred to as response levels,

prior to executing the simulation. Upon completion, GSB produces a text file containing the probability density for each bin. It is also possible to have GSB generate a text file containing the PCE coefficients themselves with the functional form depending on the chosen input distributions. This can be used to recover the polynomial approximation. Main-effect and total-effect Sobol indices can also be printed to a text file by GSB but the number of higher order nonlinear combination effects calculated depends on the grid type used.

While GSB does possess its own Bayesian inference algorithms, for the purposes of this study, Bayesian inference was performed outside GSB. Regardless, some GSB-generated data was used for generating tuning parameter posterior distributions and confidence intervals in the property profiles. Because PCEs are a computationally inexpensive method of generating output data for a large number of random input samples, it was an advantageous method for constructing appropriately dense distributions for confidence intervals.

Uncertainty quantification and sensitivity analysis were the driving reasons for using GSB but the optimization methods also presented some utility for the study at hand. Both local and global optimization algorithms are available. The first implementation of the optimization functionality in the study at hand was to further refine the tuning parameter values using local optimization. Details of the optimization can be found in the following section.

CHAPTER 4

Results from Non-Deterministic Analysis

4.1 Optimization Results

Using the CONMIN conjugate gradient descent local optimization method in GSB, the model tuning parameters were further refined from the values determined by the aforementioned parameter sweep. Optimization algorithms require the establishment of a figure of merit (FOM) to be minimized in the optimization process. The FOM for the purposes of this optimization was a weighted average of the trapezoidal integration of the relative error, as described in Section 2.2.1, in pressure and temperature data between this paper's model and the Jung et al. model. The mathematical description of the FOM can be seen below with the integrated relative error shown as E^*.

$$\text{FOM} = \omega_T E_T^* + \omega_p E_p^* \tag{4.1}$$

where ω_T and ω_p are the weights for temperature and pressure with the values of 90% and 10% respectively. Temperature was given a greater weight because the Jung et al. model exhibited much better agreement with experimental temperature data than with experimental pressure data. The results of the optimization can be found in Table 4.1.

	FOM	E_{f2} (J/mol)	K_1 (m^3/mol)	N_s (m^{-3})
Pre-Optimization	2.77%	14900	0.00104	780
Post-Optimization	2.58%	15061	0.001079	794.6

Table 4.1: Pre-Optimization and Post-Optimization Tuning Parameter Values

In addition to refining the tuning parameters, optimization techniques were implemented

to determine the reference enthalpy values that replicated the Jung et al. model results the best as well as the pressure model coefficients that best predict the experimental pressure data for the standard case. For the enthalpy value optimization, a four-dimensional optimization ($h^{\circ}_{H_2O_2,(l)}, h^{\circ}_{H_2O_2,(g)}, h^{\circ}_{H_2O,(l)}, h^{\circ}_{H_2O,(g)}$) was conducted using the same FOM as described before. As a homogeneous diatomic molecule, the O_2 reference enthalpy was not used as variable input but fixed at the conventional value of 0. A two-stage global-to-local optimization was used to robustly explore the input domain while achieving a sufficient level of refinement. Global optimization was conducted using the COLINY DIRECT algorithm with the optimum input set being seeded as the initial point for the local optimization CONMIN algorithm. Results of the optimization can be found in Table 4.2 with reference enthalpies, or heats of formation, in units of J/mol. Standard case temperature and pressure profiles with the optimized reference enthalpies can be found in Figures 4.1 and 4.2.

	FOM	$h^{\circ}_{H_2O_2,(l)}$	$h^{\circ}_{H_2O_2,(g)}$	$h^{\circ}_{H_2O,(l)}$	$h^{\circ}_{H_2O,(g)}$
Pre-Optimization	2.58%	-187341	-135453	-285825	-241831
Percent Change	-84.5%	+2.7%	-3.6%	+0.004%	+2.8%
Post-Optimization	0.399%	-192362	-130610	-285837	-248622

Table 4.2: Pre-Optimization and Post-Optimization Reference Enthalpy Values in J/mol

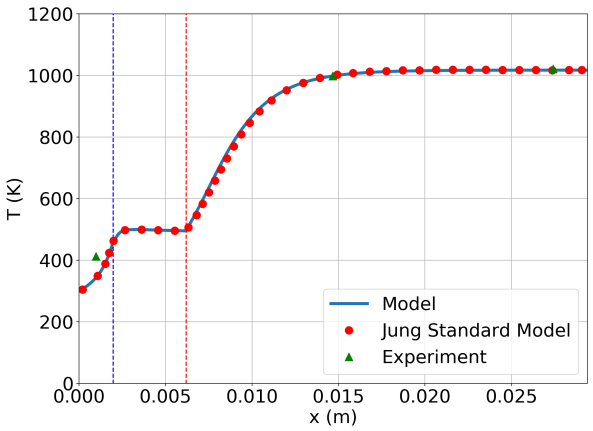

Figure 4.1: Standard Test Case Temperature Profile with Optimized Reference Enthalpies

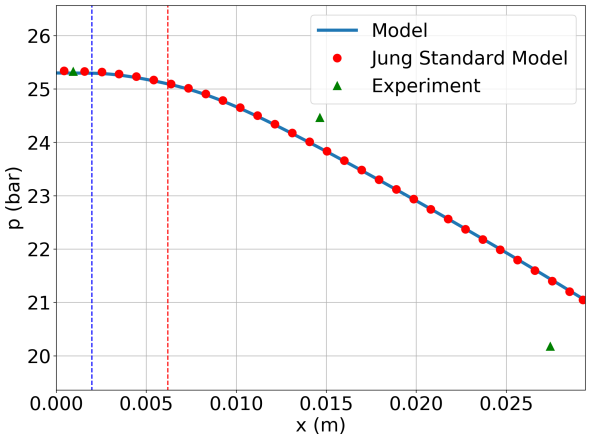

Figure 4.2: Standard Test Case Pressure Profile with Optimized Reference Enthalpies

The figure of merit is significantly reduced by making small adjustments to the reference enthalpy values used in the model. While temperature and pressure profiles with the optimal enthalpy set are shown only for the standard case, as similar improvement occurs in the remaining test cases aside from the high mass flow rate case. The largest deviation occurs in the reference enthalpy of gaseous H_2O_2 which, as we will see in Section 4.3, has an insignificant impact on the adiabatic decomposition temperature of the mixture. Because 2/3 experimental data points for temperature, the dominant quantity in determining the FOM, are nearly equal to the adiabatic decomposition temperature, one would expect that $h^{\circ}_{H_2O_2,(g)}$ would consequently have an insignificant impact on the FOM. Therefore, it is posited that $h^{\circ}_{H_2O_2,(g)}$ could be fixed at the original value and a similar FOM would be attained. Even with an identical reference enthalpy set, variations in the model resulting in a nonzero FOM would be expected due to discrepancies in other thermochemical and thermophysical data used in the models. Investigation into the optimum enthalpy set was conducted primarily to substantiate the argument that the difference in temperature predictions between the models was primarily due to the reference enthalpy set which, given the results shown above, appears to be the case. The post-optimization enthalpy values will not be used any further in this study.

Similar to the enthalpy optimization, an investigation of the optimum set of pressure model coefficients was investigated using a two-stage global-to-local optimization. Starting from the Ergun model coefficients [13], a global optimization was conducted using the NCSU DIRECT algorithm with the FOM being the integrated relative error between the model predicted pressure and a curve fit through experimental pressure data from the Jung et al. [10] standard case. Again, results from the global optimization were seeded in the local CONMIN optimization. Results of the optimization can be found in Table 4.3 with the pressure profiles compared in Figure 4.3.

	FOM	c_1	c_2	c_3
Ergun	8.38%	150	1	1.75
Post-Optimization	1.40%	299	0.0414	3.355

Table 4.3: Ergun Model and Post-Optimization Pressure Model Coefficients

Figure 4.3 shows that the optimized pressure drop model results in the pressure curve passing through the experimental data point closest to the outlet. While this is an improvement in the prediction of the overall pressure drop through the bed, the pressure prediction for the central data point deviated further than that of the Ergun model [13]. From this is can be deduced that the given method of computing the pressure gradient is insufficient for predicting the pressure drop through the catalyst bed. The pressure gradient equation is incapable of generating a pressure curve that could reasonably approximate the experimental pressure data. Several features of the pressure gradient and its derivation may contribute to this predictive deficiency. First and foremost, the model at hand is a mixture model meaning that the gas and liquid phase properties are either assumed to be equal, such as temperature and pressure, or are lumped through a weighted average based on the evaporation parameter or void fraction. This neglects interfacial friction between the two phases and local effects caused by property variations such as differences in catalyst interactions between the phases. As was mentioned previously, Zoltani [13] states that wall effects in a packed bed become non-negligible for bed-to-pellet diameter ratios less than 40. Additionally, the Ergun packed

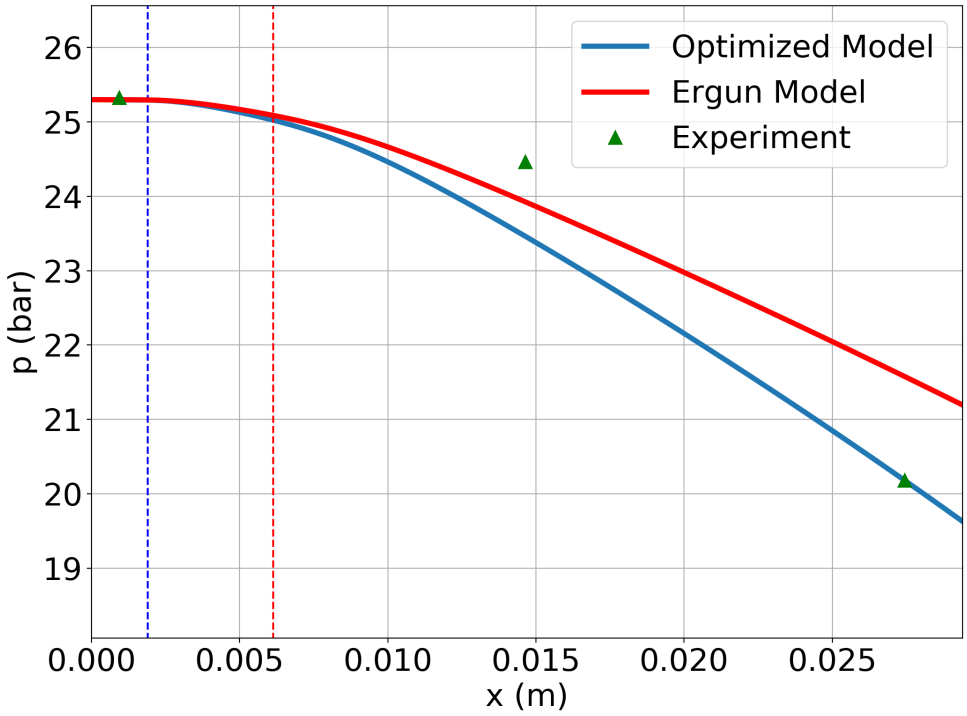

Figure 4.3: Standard Case Pressure Profiles for Ergun Model and Optimized Model

bed pressure drop model was developed for steady gas flow with constant axial velocity [13] while the catalyst bed model is two-phase flow with a continually varying axial velocity.

4.2 Uncertainty Quantification Results

Uncertainty quantification on the system was initially conducted by generating histograms for outputs of interest for different physical input distributions. To replicate experimental uncertainty, each of the physical inputs (T_i, p_i, $\dot{m}$, and Y) was assigned a Gaussian distribution with the mean located at the test case value. It should also be noted that for a syringe-based fluid injection system, there will be a coupling between the mass flow rate of propellant and the inlet pressure. Primary QOI for these studies are the ending temperature and pressure drop through the bed as these quantities define the chamber properties and

thus are paramount for predicting thruster performance. Having not been provided any data regarding the precision of the instruments used to conduct the thruster tests in Jung et al., the uncertainties in the input quantities will be assigned as standard deviations σ based on percentages of the mean value μ. Several histograms for a standard deviation of 1% of the mean using values from the standard case can be seen below. The scaled probability density value on the ordinate axis is the probability density value normalized as if the width of each bin was unity.

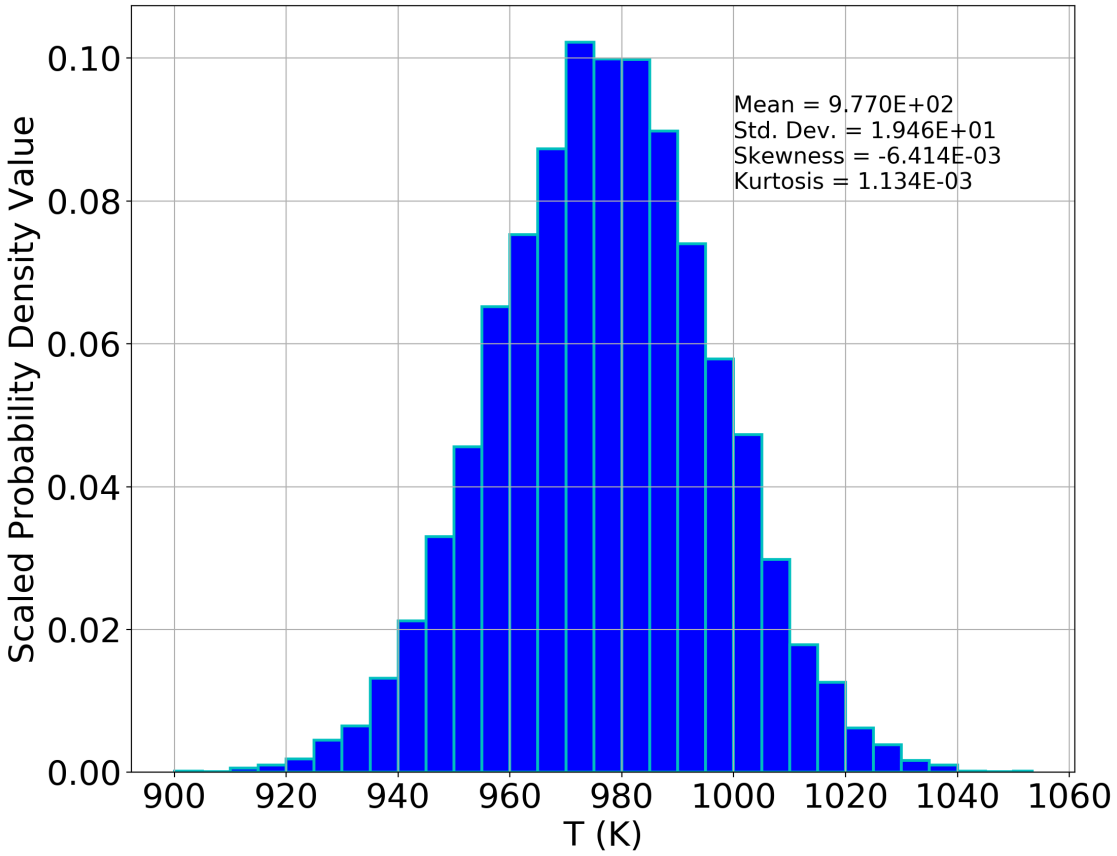

Figure 4.4: Distribution of T_{end} for $\sigma = 0.01\mu$ in $T_i,\ p_i,\ \dot{m}$, and Y

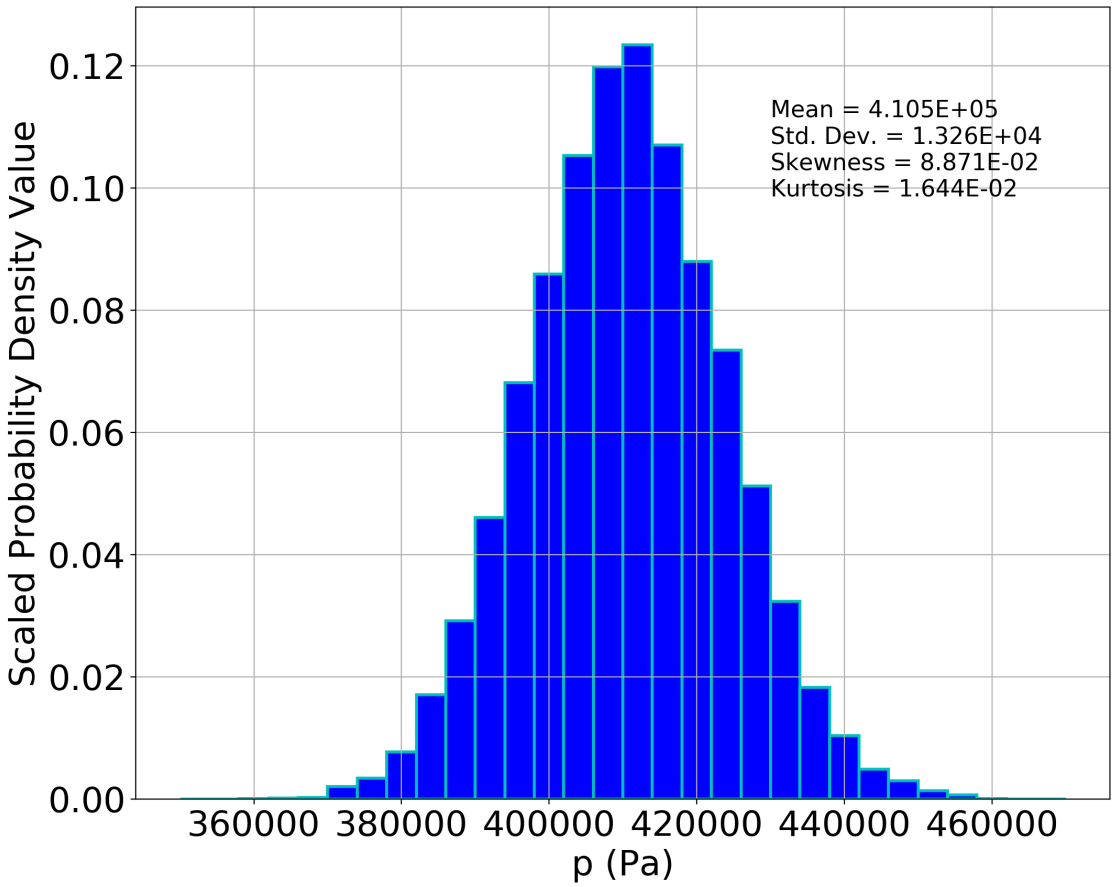

Figure 4.5: Distribution of p_{loss} for $\sigma = 0.01\mu$ in $T_i,\ p_i,\ \dot{m}$, and Y

It can be seen that the distributions of T_{end} and p_{loss} for the given set of inputs are Gaussian with very little skew. Standard deviations in T_{end} and p_{loss} are 19 K and 0.133 bar respectively. With a 1% standard deviation in the inputs, any nonlinear behavior in the two outputs above has yet to make itself apparent. This may be because the magnitude of the uncertainty is too small for the input distributions to undergo any significant nonlinear transformations within the system and thus only a linear scaling is observed. Figures 4.6 and 4.7 below contain histograms of the pressure loss through the bed for different input distributions as described in their respective captions.

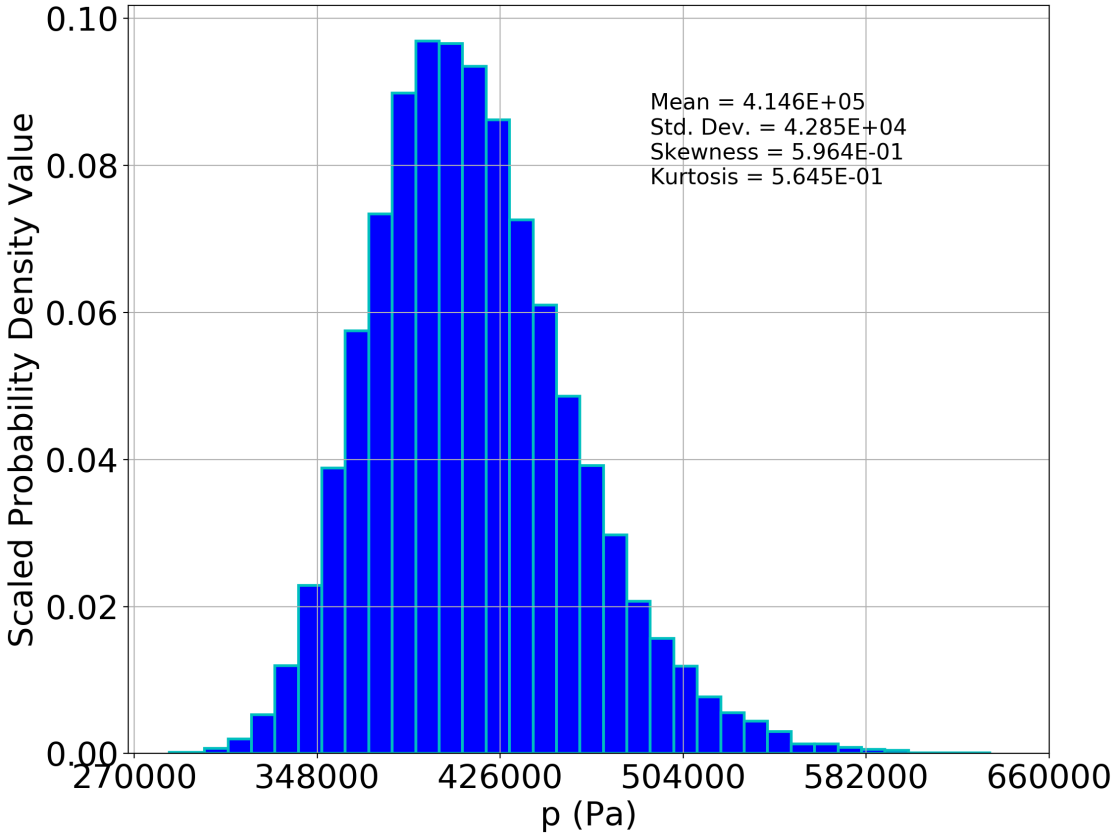

Figure 4.6: Distribution of p_{loss} for $\sigma = 0.01\mu$ in $T_i,\ Y,\ \dot{m}$, and $\sigma = 0.10\mu$ in p_i

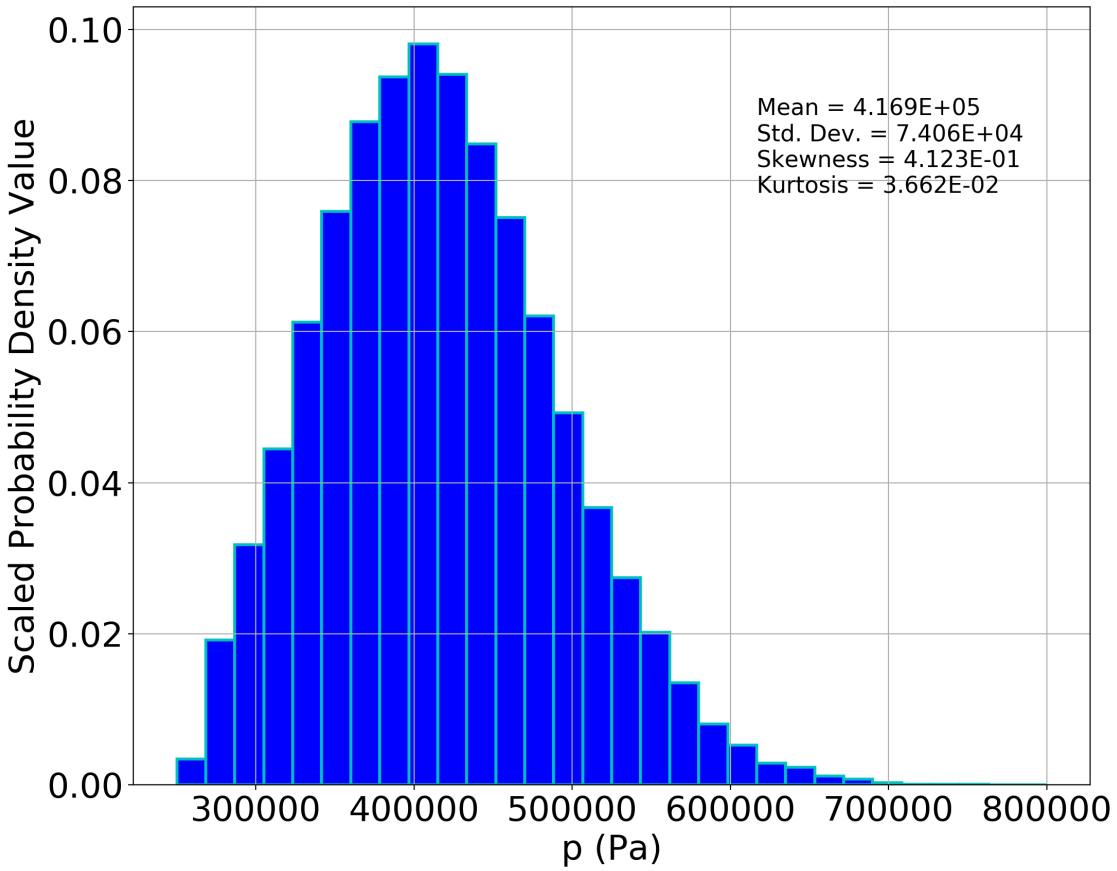

Figure 4.7: Distribution of p_{loss} for $\sigma = 0.01\mu$ in $T_i,\ Y,\ p_i$, and $\sigma = 0.10\mu$ in $\dot{m}$

Unlike the uniform standard deviation case, both figures above show skew in the distributions caused by the increased uncertainty magnitude. Skew in the distribution is an artifact of the nonlinear scaling of the pressure drop with inlet pressure and mass flow rate in the catalyst bed. Incremental increases in the aforementioned inputs result in progressively greater pressure drops seen by the distribution tail extending in the direction of increasing pressure loss. Both standard deviation and skew of the pressure loss increase to a greater degree when the uncertainty is greater for the mass flow rate than for the inlet pressure. From a qualitative perspective, this indicates that the pressure drop through the bed has a higher sensitivity to perturbations in mass flow rate than for those in the inlet pressure. Quantitative confirmation of the statement will be shown in Section 4.3. A more direct comparison of the pressure loss histograms described above can be seen in Figure 4.8.

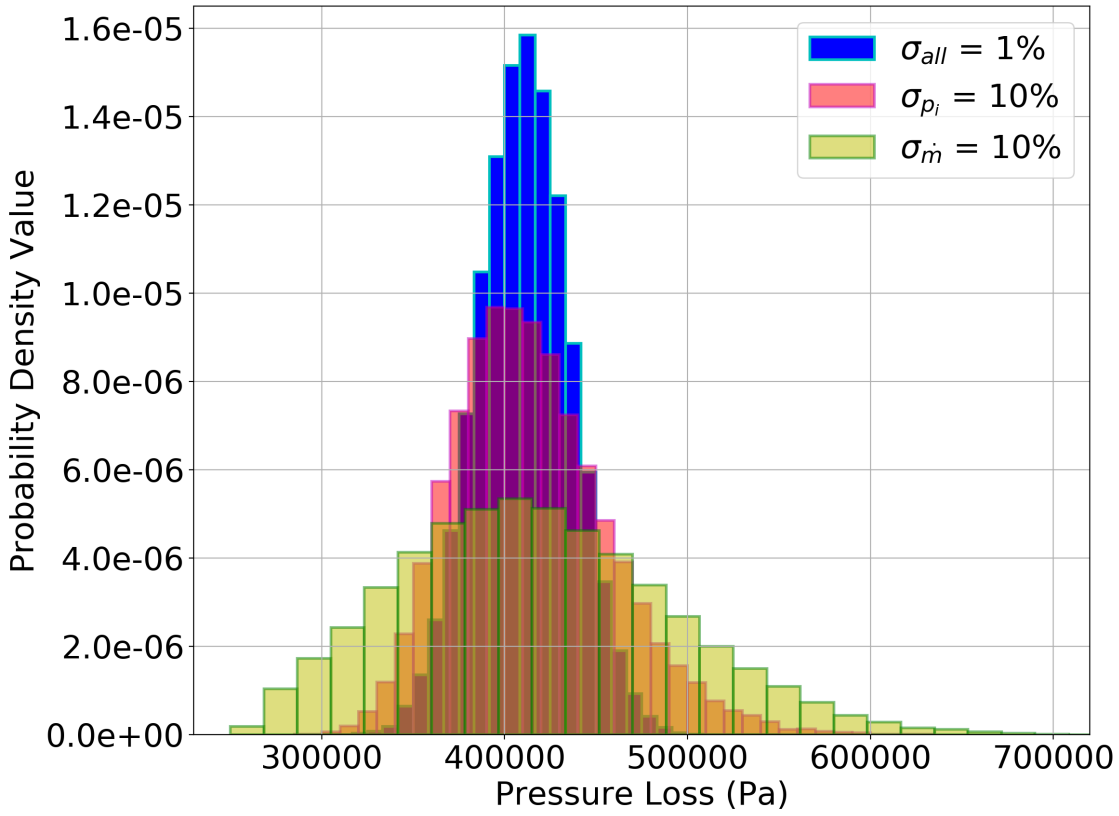

Figure 4.8: p_{loss} Distributions for Various Input Distributions

Again, increased sensitivity to the mass flow rate can be observed. A large uncertainty in mass flow rate results in a much greater uncertainty in the pressure drop as compared to the two other distributions.

While the ending temperature and pressure drop are key parameters for determining overall thruster performance, it is also important to characterize behavior of the catalyst bed by assessing the locations for region transitions. Region transition analysis was performed using uniform uncertainties in the four physical inputs mentioned before, each with large domains. Boiling location, the transition between Regions I and II, follows the distribution seen in Figure 4.9.

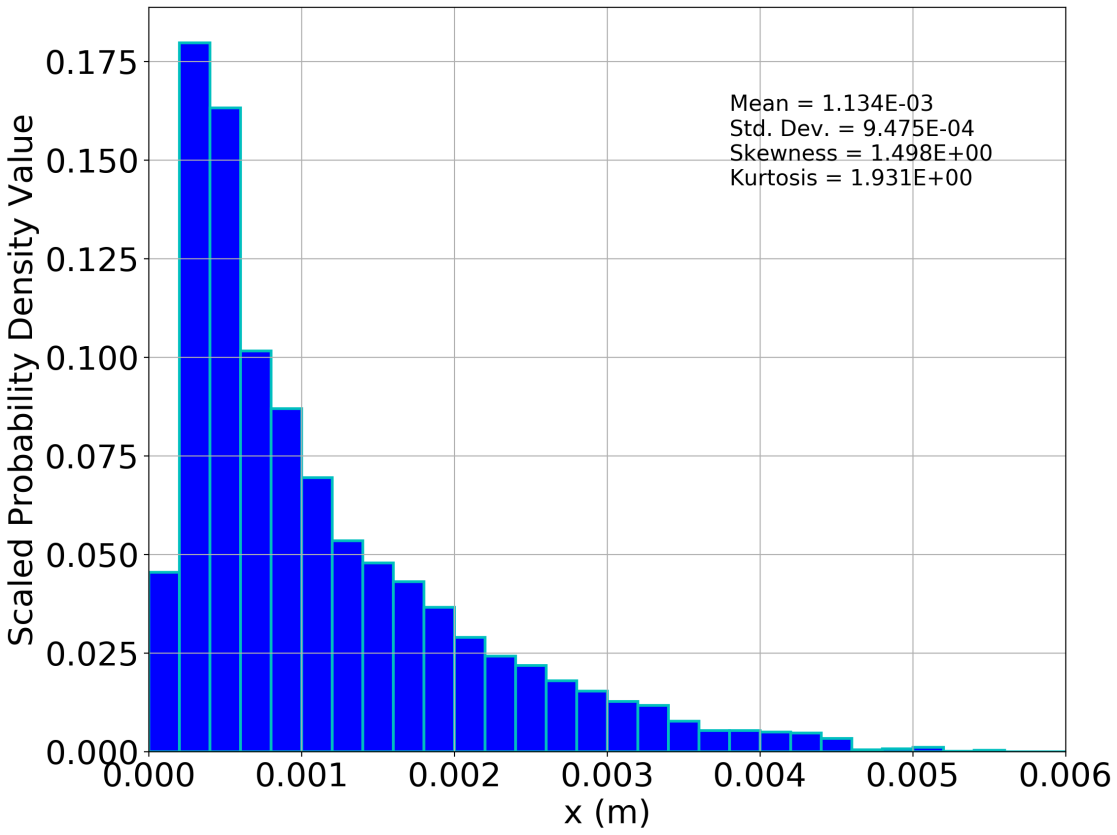

Figure 4.9: Distribution of Boiling Location for Uniform Uncertainties in T_i, Y, p_i, and $\dot{m}$

Figure 4.9 shows a highly skewed distribution with the maximum probability around 0.3 mm and a long tail in the positive x-direction. Even for a large variation in the inputs, there is a high likelihood of the boiling transition occurring within the first millimeter of the catalyst bed. The same plot could not be generated for the transition location between Region II and III for the same input distributions due to the fact that complete evaporation of the mixture was not guaranteed. A dummy value for the location was substituted to signify that the mixture had not fully evaporated which resulted in an inaccurate formulation of the PCE.

Another method of uncertainty quantification applied to the model in this study is to generate an expected value bounded by an envelope for the axial profiles for the fluid properties. This is done by generating the distributions for a property or properties at each node in the domain and then defining some metric by which an envelope can be constructed. Three

potential options were evaluated for their effectiveness in representing the expected uncertainty in the property profiles. The three options are: mean with standard deviation, median with sample distance, and maximum probability value (MPV) and confidence interval. The mean and standard deviation are self-explanatory in that the expected value is the mean and the envelope is defined by a standard deviation away from the mean. For the median method, the expected value is the median and the envelope is defined by a user-specified number of samples away from the median. This method yields two critical advantages over the mean with standard deviation method in that the median with sample distance rejects values incapable of being generated by the model and can also represent skew in the distribution through an asymmetric envelope. Even more refined than both previously described methods is the MPV with confidence interval method. Confidence intervals, as described in Section 3.4, account for probability of the values and represents the highest probability set of values thus creating the best representation of potential output values. Additionally, it is possible to generate discontinuous confidence intervals as one may expect for multimodal distributions which is not possible using the mean and median methods. Similar to the user-specified number of samples for the median method, the confidence interval method requires that the user specify the size of the confidence interval. A comparison of the three methods being implemented on a lognormal distribution can be seen in Figure 4.10.

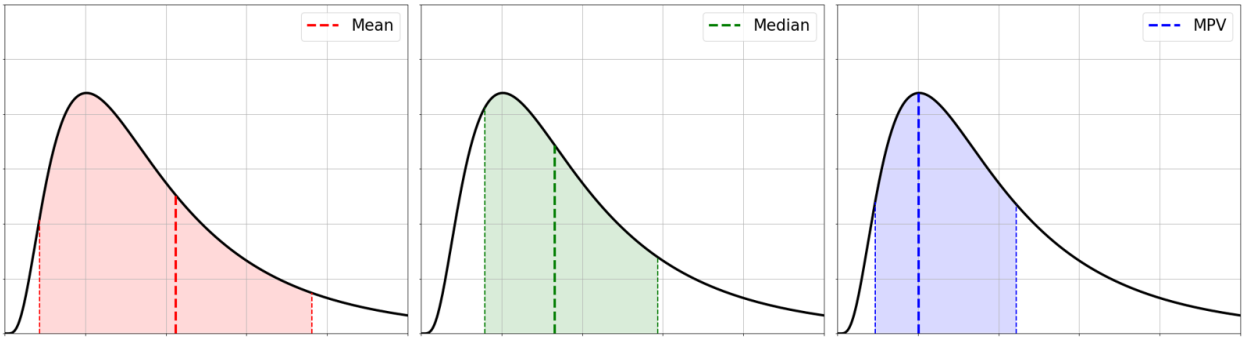

Figure 4.10: Comparison of Uncertainty Envelope Generating Methods (left-to-right: Mean with Standard Deviation, Median with Sample Distance, Maximum Probability Value with Confidence Interval)

Observing the figure, each envelope definition can be summarized as follows: the standard deviation is a fixed distance away from the mean, the sampling distance is a fixed area away from the median, and the confidence interval is the area composed of the highest probability samples, thus interval boundaries all have the same probability density. For symmetric distributions, the three methods yield similar results. All three methods for the plots above were calibrated such that each method bounded the same interval for a particular Gaussian distribution. The consequence of implementing the confidence interval method for the axial property profiles is the high computational cost due the requirement of binning the property values at each node to create a probability density function. For this reason, the required sampling density for this method is much greater than for the other two methods. Some difficulty was experienced in producing the requisite number of samples using GSB given the size of the data files and available computing capabilities. Due to these restrictions, the median with sample distance, denoted δ, was chosen as it requires minimal computational rigor, is capable of capturing skew in the output distributions, and multimodal distributions were neither expected nor found in creating histograms.

Axial uncertainty profiles in this study were generated using the results from a PCE for the QOI at each node. One important note is that the PCE is not an emulator trained to reconstruct the profile in x but instead is a polynomial approximation of the QOI at each separate node as a function of the random inputs. Therefore, the values at neighboring nodes are defined by distinct polynomials (although neighboring polynomial forms and coefficients should be similar in regions of continuous slope and value). Sample distances of 20% and 40% of the total number of samples are shown in each of the uncertainty profile plots. First, the uncertainty profiles for Gaussian-distributed physical inputs with standard deviation equal to 1% of the mean will be shown. The PCE was trained using 238 model simulations located on a third-order sparse grid with Sobol variance-based adaptation to refine the grid in dimensions with high variation and coarsen the grid in dimensions with low variation. Once the PCE had been trained, 5000 emulator samples were generated to produce the following plots.

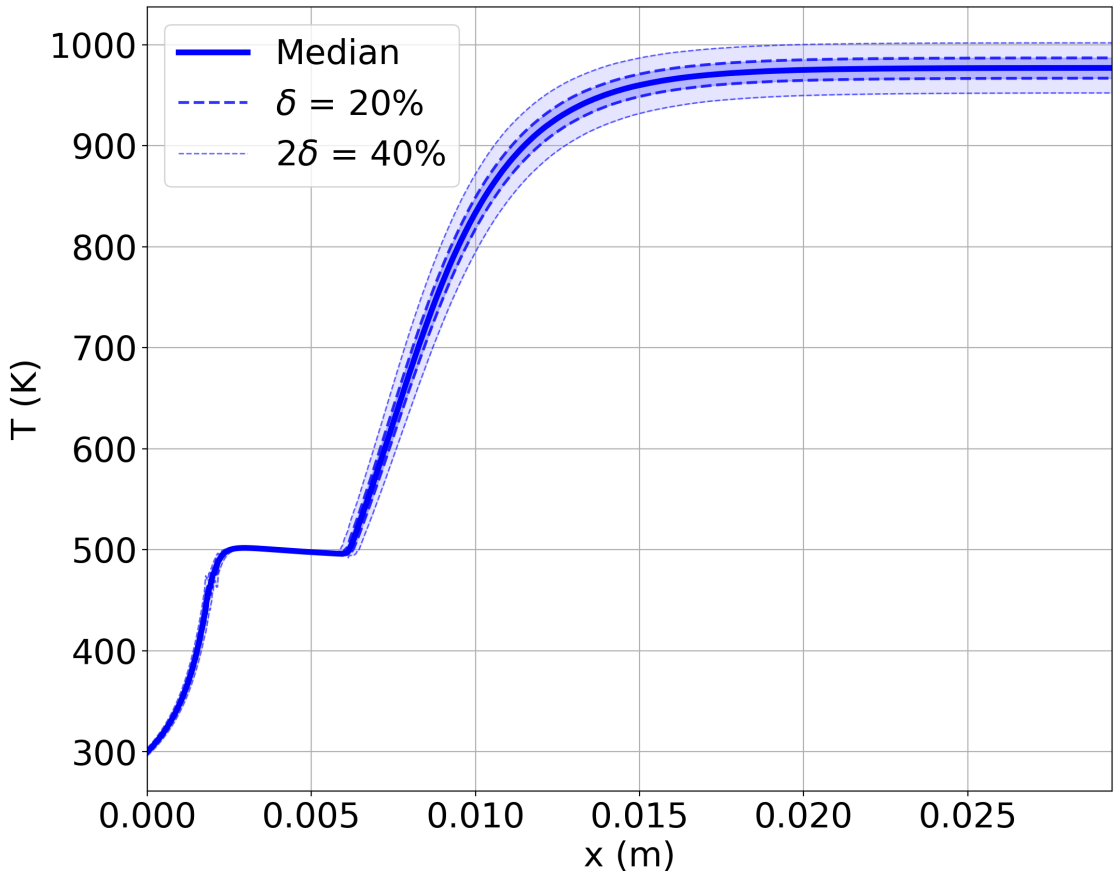

Figure 4.11: Axial Temperature Profile with Uncertainty for $\sigma = 0.01\mu$ in $T_i,\ p_i,\ \dot{m}$, and Y

From the figure above, it can be seen that 80% of the samples fall within approximately 950-1000 K for the ending temperature and the median ending temperature is 977 K, approximately equal to the deterministic solution for the standard case. This is consistent with the data presented in Figure 4.4. Even small variations in the physical inputs can result in significant variation in the decomposition temperature of the mixture and for that reason, it is critical to have adequate estimates of experimental uncertainties for each property. As was mentioned earlier in the text, QOI distributions are necessary for constructing distributions for relevant thruster quantities, such as thrust, thus it is important that one has accurate values for the form and characteristics of the input distributions. Figures 4.12 and 4.13 show profiles for pressure and the evaporation parameter respectively.

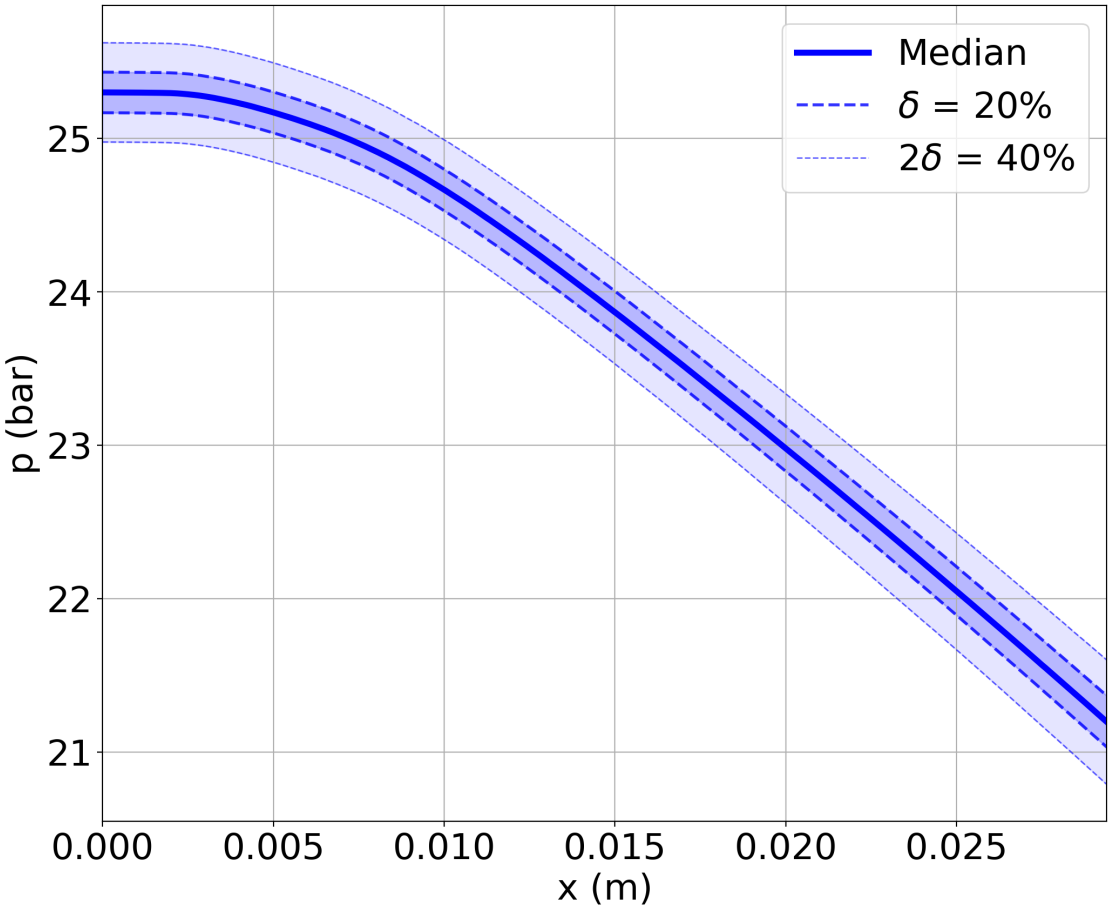

Figure 4.12: Axial Pressure Profile with Uncertainty for $\sigma = 0.01\mu$ in $T_i,\ p_i,\ \dot{m}$, and Y

As pressure drops through the bed, the uncertainty in the pressure remains approximately constant with only a small increase near the bed outlet. In this case, uncertainty in the mixture pressure appears to be dominated by the initial uncertainty in the inlet pressure.

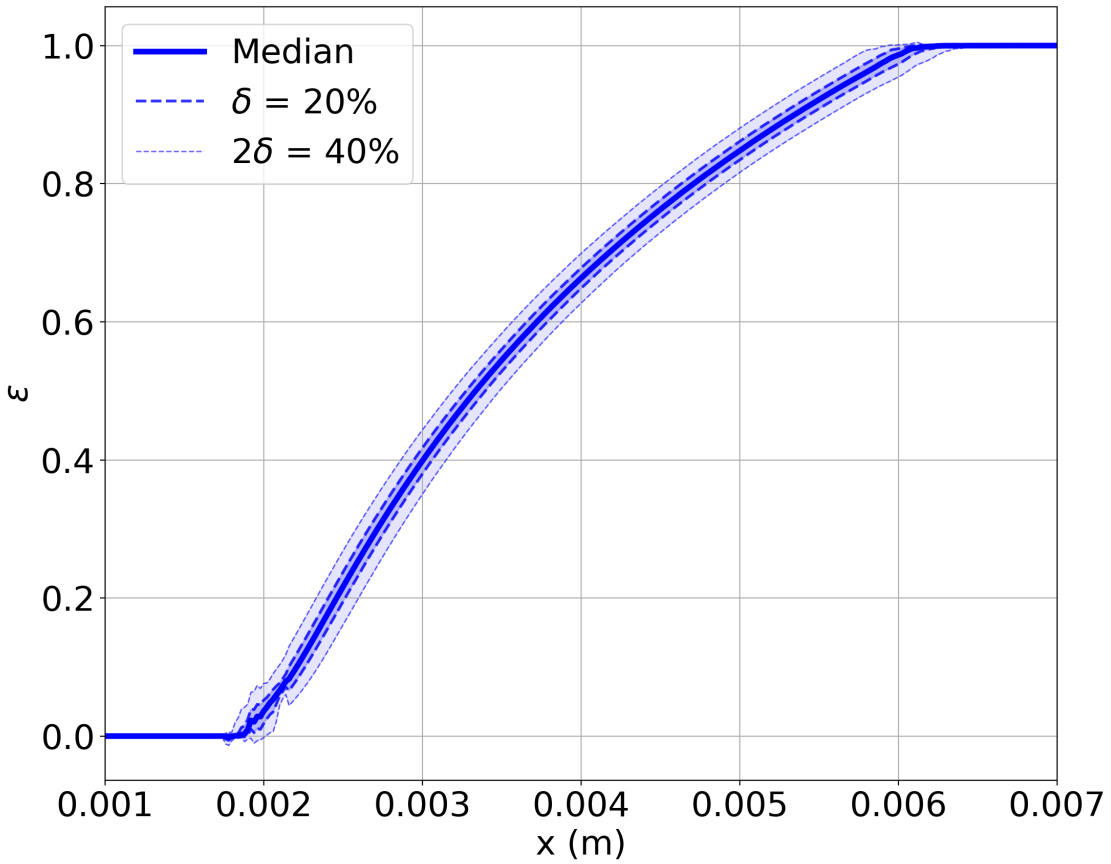

Figure 4.13: Axial Evaporation Parameter Profile with Uncertainty for $\sigma = 0.01\mu$ in $T_i,\ p_i,\ \dot{m}$, and Y

In the vicinity of $x = 0.002$ m, there is considerable noise in the evaporation parameter value and the bounds formed by the sample distances. Noise at this location is a consequence of the transition from Region I to II as there is a discontinuity in both the mixture temperature and evaporation parameter. It is important to note that this is not a polynomial oscillation that would arise as a consequence of mapping a polynomial to the evaporation parameter as a function of axial distance x. Instead, the noise is due to the shifting location of the boiling location x_b. Each node at which x_b is located for some subset of high fidelity samples has a discontinuous set of evaporation parameter values being mapped to a polynomial in the random input variables. This results in noisy predictions of the evaporation parameter when creating the emulator samples with the PCE. A similar effect can be seen

at $x \approx 0.006$ m where the transition between Regions II and III occur, albeit to a much lesser extent. Emulator noise as a result of transition discontinuities will be seen in many of the PCE generated plots to follow, in particular the axial temperature profiles. This noise can result in the uncertainty envelopes, or even the median values, containing nonphysical values that cannot be predicted by the model such as evaporation parameters less than 0 or greater than 1.

Similar plots were generated with fixed physical inputs and Gaussian distributed reference enthalpies. Once again, $h^{\circ}_{O_2}$ is held constant while the four remaining reference enthalpies are allowed to be varied. Following the format of the previous analysis, the variable reference enthalpies were assumed to have Gaussian distributions with the mean equal to the standard values and a standard deviation of 1% of the mean values. Effects of permutations in the reference enthalpies in mixture properties propagate from the enthalpy balance equation and thus are only directly seen by mixture temperature and evaporation parameter. Consequently, it was deemed only necessary to use a second-order sparse grid with 87 high fidelity simulations. Plots of mixture temperature and pressure can be seen in Figures 4.14 and 4.15 respectively.

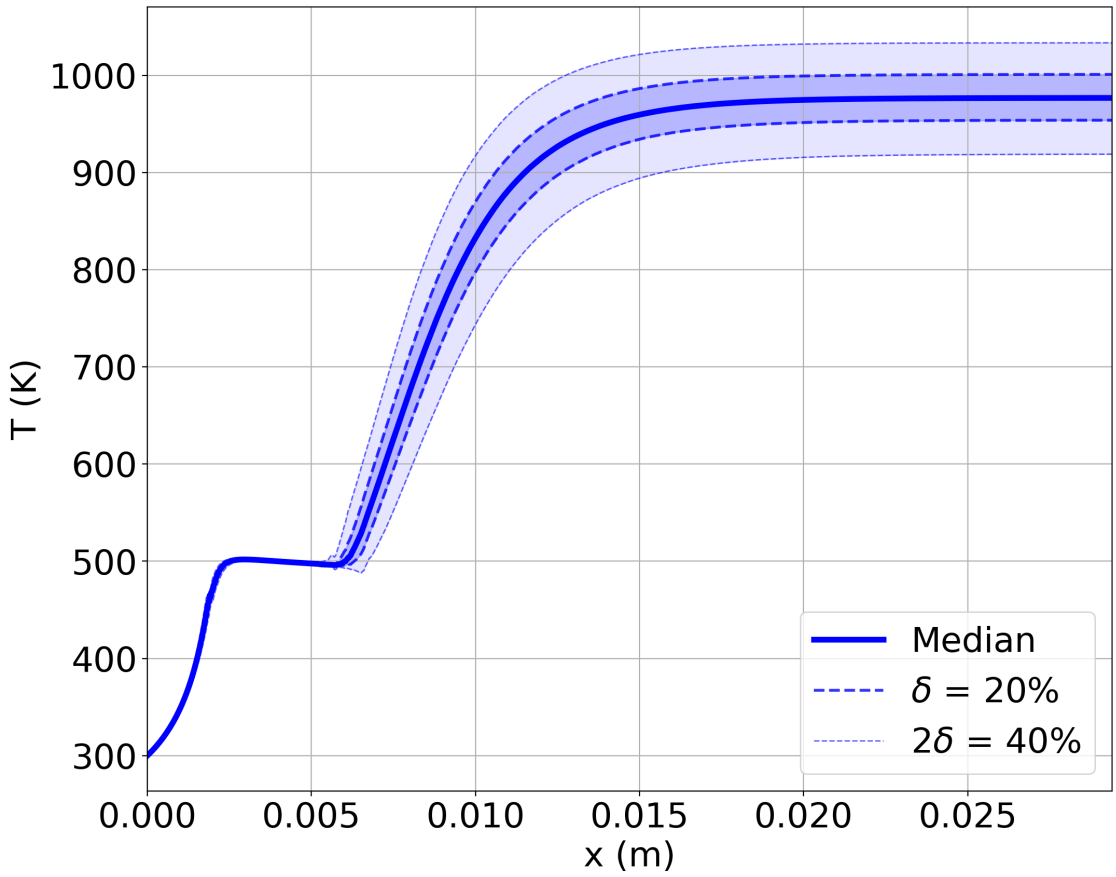

Figure 4.14: Axial Temperature Profile with Uncertainty for $\sigma = 0.01\mu$ in H_2O_2 and H_2O Reference Enthalpies

Mixture temperature in Region III has a strong dependence on the reference enthalpy set while there is minimal dependence in Regions I and II. Variation in temperature in Region I is small due to partial cancellation of the liquid reference enthalpies due the terms occurring on both sides of the enthalpy balance equation. While the same partial cancellation occurs in Region II to a lesser extent due to the presence of the gas phase, mixture temperature is further stabilized by the constraint of satisfying the summation of partial pressures with temperature-dependent saturation pressures. In Region III, the entire mixture is in the gas phase and enthalpy variations result in significant variation in temperature as the previously mentioned stabilizing effects are no longer present. For the ending temperature, 80% of the samples fall within approximately 60 K of the deterministic standard case value of 977 K.

This is once again consistent with the corresponding histogram which can be found in Figure B.1 in Appendix B.

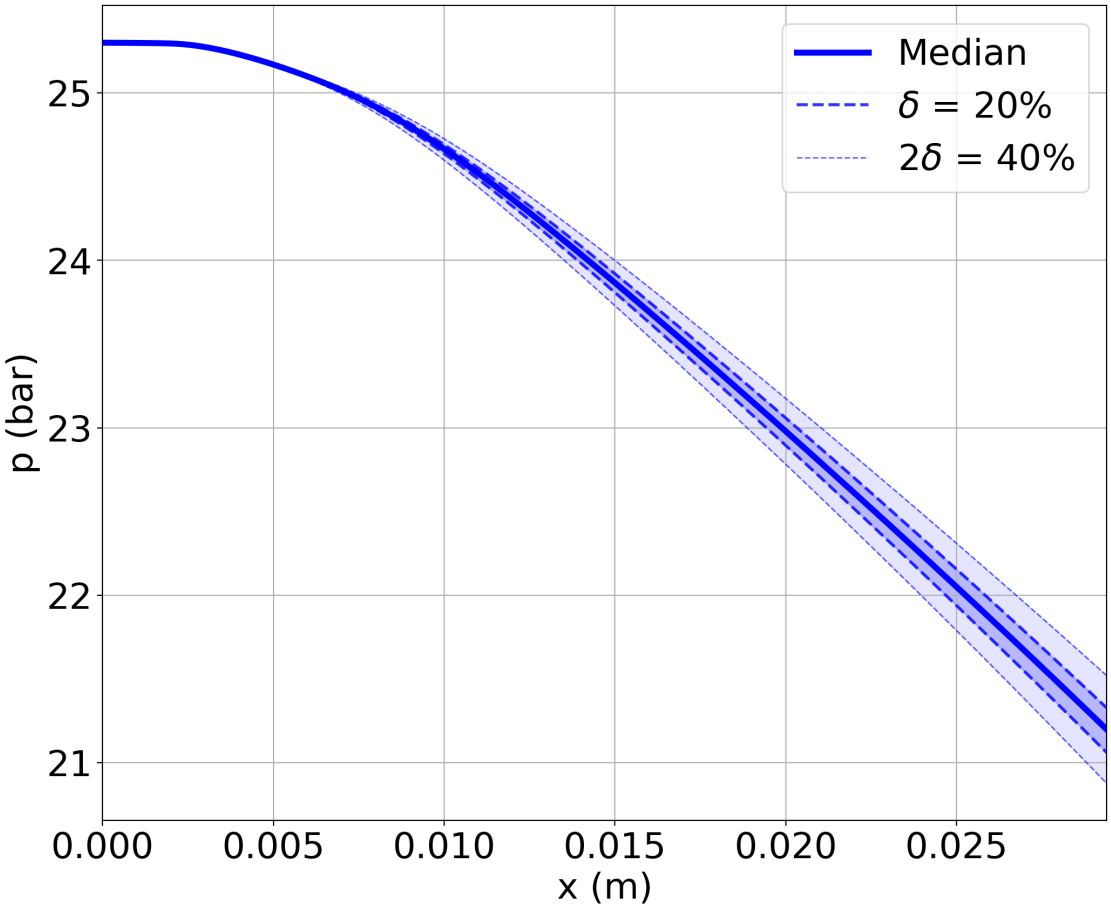

Figure 4.15: Axial Pressure Profile with Uncertainty for $\sigma = 0.01\mu$ in H_2O_2 and H_2O Reference Enthalpies

In contrast with the uncertainty profile for random physical inputs, there is no uncertainty in the inlet pressure in this case. Instead, the uncertainty envelope grows from zero uncertainty as x increases. The variation in the pressure is due to the direct effects of the enthalpies on the temperature and evaporation parameter as this impacts the pressure gradient equation through viscosity, density, and the void fraction. The 80% envelope for the ending pressure spans approximately 0.6 bar.

To further investigate the effects of uncertainty in thermophysical data on the model,

uncertainty profiles were created with the dynamic viscosities for each species as the random variables. Each viscosity was directly multiplied by a scaling factor to change the value. In other words, the viscosity profiles were only stretched and compressed; there was no modification of the relative scales of the polynomial coefficients that would further alter the temperature-dependent profile. Because the viscosities vary as the mixture progresses through the bed, the scaling factors that are multiplied with each viscosity act as the random input variables. The mean is the unchanged case, a scaling factor of 1, and the standard deviation is 0.1. A majority of the property profiles display no discernible uncertainty with the exception of the Reynolds number. As one would expect by the definition of the Reynolds number, the uncertainty results in a direct scaling of the Reynolds number. This can be seen below in Figure 4.16.

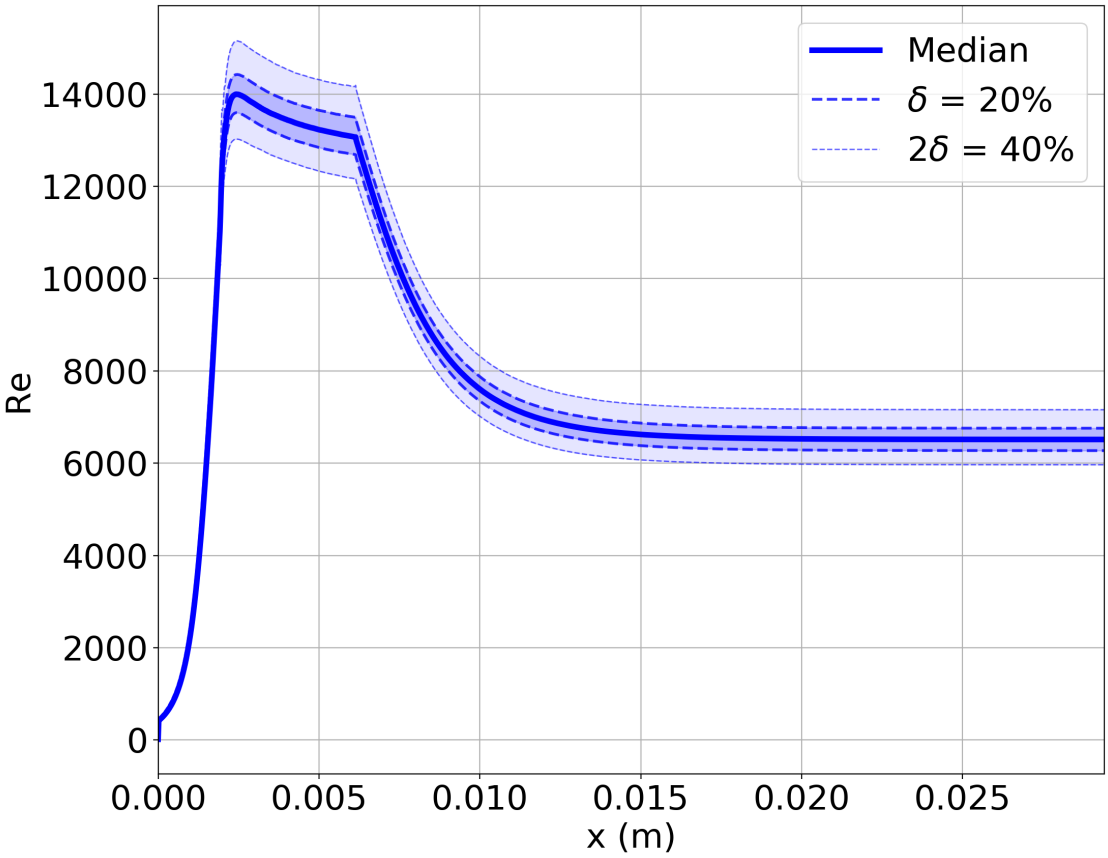

Figure 4.16: Axial Reynolds Number Profile with Uncertainty of $\sigma = 0.1$ in Species Dynamic Viscosity Scaling Factors

4.3 Sensitivity Analysis Results

Sobol indices [22] were generated to provide quantitative measures of how sensitive response functions are to multiple sets of random input variables. Visualizing the Sobol indices for each of the random variables and their nonlinear combination effects proved to be challenging due to the high dimensionality of the problem. Ultimately it was decided that the Sobol indices would be plotted on a heat map with each row corresponding to the order of effect, i.e. the first row contains first-order effects, the second row contains second-order effects, etc. Colors of the heat map scale with the base 10 logarithm of the corresponding Sobol index with lighter colors corresponding to higher sensitivities and vice-versa. The number under each set of variables, is the Sobol index corresponding to that variable subset. It is important to consider that the sensitivities shown above are only valid on the domain analyzed and while the Sobol indices represent global sensitivities within the system, there may be additional behaviors that alter the Sobol indices outside the current domain. Sobol indices for the ending temperature and pressure loss for physical inputs can be found in Figures 4.17 and 4.18.

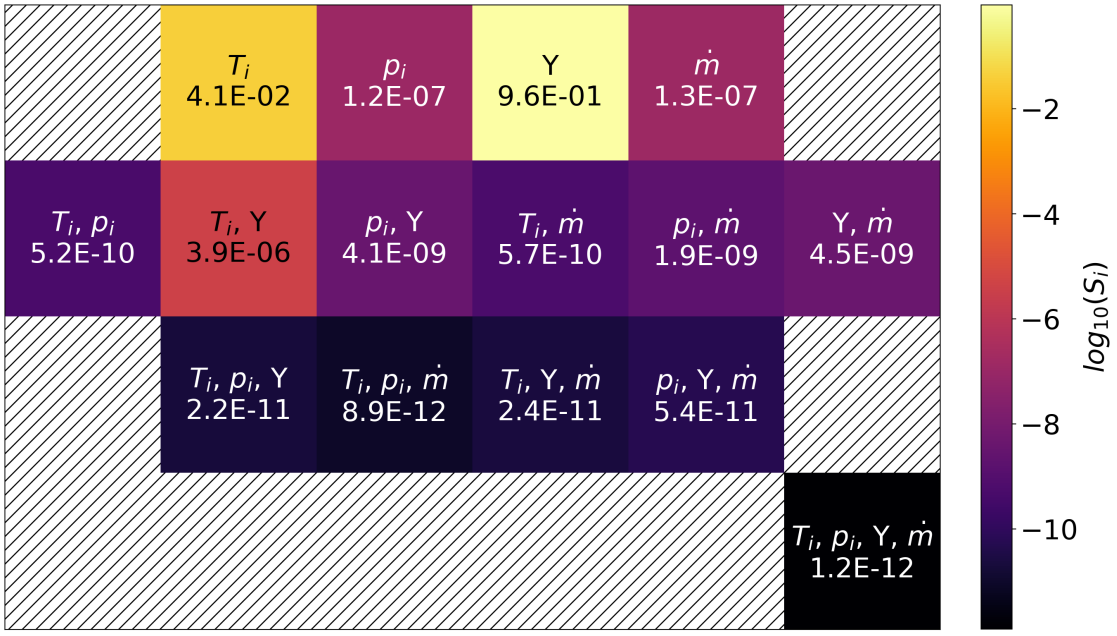

Figure 4.17: Sobol Index Grid for T_{end} for $\sigma = 0.01\mu$ in $T_i,\ p_i,\ \dot{m}$, and Y

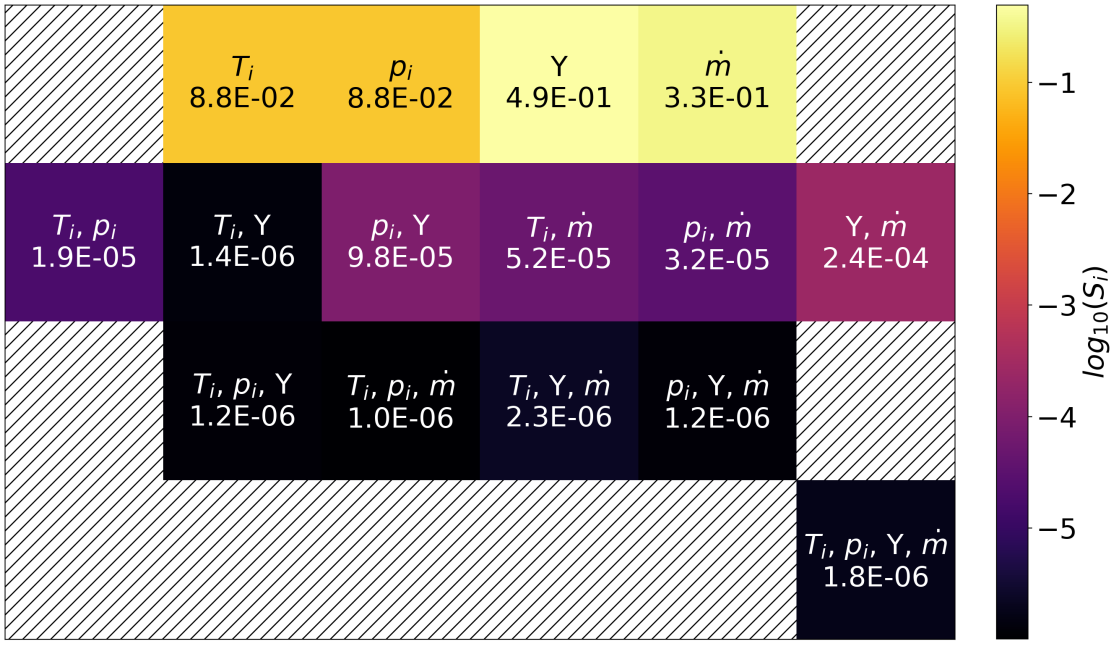

Figure 4.18: Sobol Index Grid for p_{loss} for $\sigma = 0.01\mu$ in $T_i,\ p_i,\ \dot{m}$, and Y

The first row contains the total-effect indices that sum the main-effect indices with all nonlinear combination indices to which the variable contributes. Figure 4.17 shows that the ending temperature is strongly dependent on the propellant concentration Y and weakly dependent on the input temperature T_i while exhibiting negligible dependence on both the input pressure and mass flow rate. It should be noted that these sensitivities are calculated for the domain of the specific input distributions and is not representative for sensitivities across all operating regimes. For example, it is possible to increase mass flow rate such that the final reaction advancement is significantly reduced thereby increasing the dependence of the end temperature of the mass flow rate of the mixture.

Based on the results shown in Figure 4.8, the claim was made that the pressure drop through the system has a greater sensitivity to mass flow rate than to the input pressure of the system. This claim is corroborated by the Sobol indices for pressure drop shown in Figure 4.18 as the total-effect index for mass flow rate is 0.33 whereas the index for inlet pressure is 0.088. As is true for the ending temperature, the highest sensitivity is to the propellant concentration. This is due to the strong influence that the concentration has on

temperature evolution throughout the catalyst bed acting in conjunction with the strong temperature-dependence of several terms within the pressure gradient equation.

Similar sensitivity analysis was performed for the reference enthalpy values used in the model. Sobol indices for ending temperature and pressure loss with reference enthalpy values as input variables can be seen in Figures 4.19 and 4.20 respectively.

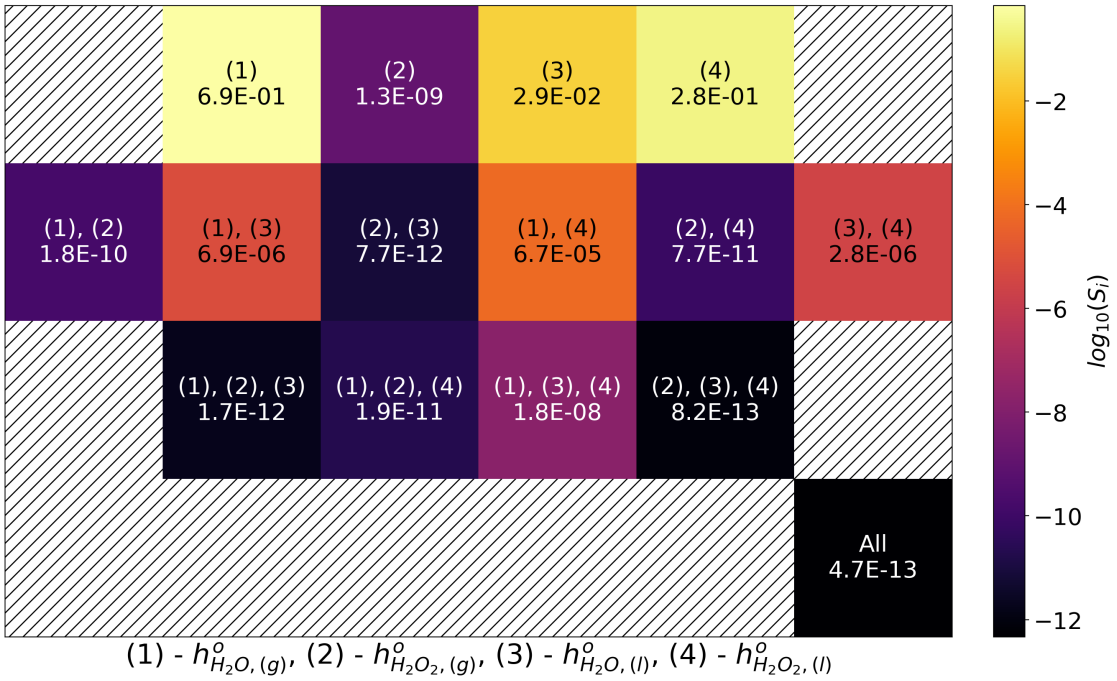

Figure 4.19: Sobol Index Grid for T_{end} for $\sigma = 0.01\mu$ in Reference Enthalpies

As can be seen above, the ending temperature is most sensitive to the reference enthalpies for gaseous H_2O and liquid H_2O_2. Simultaneously, the final temperature is negligibly dependent on the reference enthalpy for gaseous H_2O_2. These sensitivity values agree with qualitative expectations stemming from the decomposition temperature in Equation 2.88. In this equation, $h^\circ_{H_2O_2,(g)}$ does not make an appearance while gaseous H_2O and liquid H_2O_2 are the major contributing species to the final and initial enthalpies respectively. Ending temperature is at all sensitive to the reference enthalpy of gaseous H_2O_2 only due to its impact on the intermediate temperature calculations and thus the rate of reaction throughout the bed.

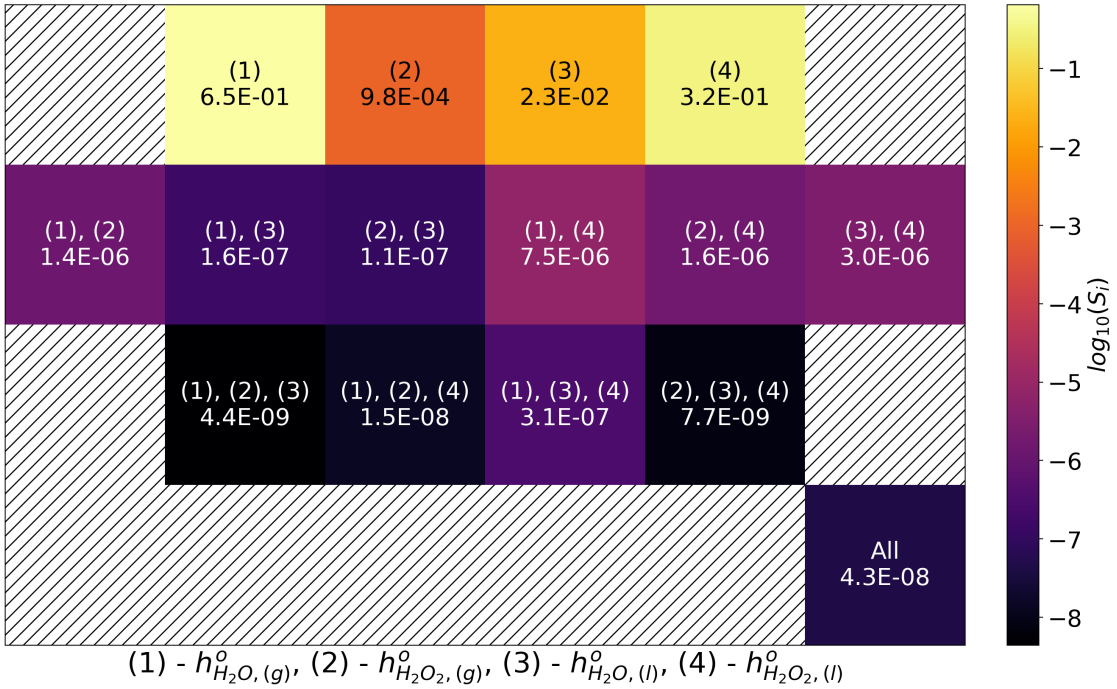

Figure 4.20: Sobol Index Grid for p_{loss} for $\sigma = 0.01\mu$ in Reference Enthalpies

Pressure loss exhibits nearly the same dependencies as the ending temperature with higher sensitivity to the reference enthalpy of gaseous H_2O_2. This is likely due to the pressure drop being the sum total of compounding pressure loss through each node. As was the case with the pressure drop sensitivity to the mixture concentration, there is no direct impact of the reference enthalpies on the pressure gradient equation. The influence is through the impact on temperature and how that effects the temperature-dependent thermophysical properties that arise in the pressure gradient equation.

Understanding which inputs are the primary drivers for region transitions and the overall shape of the temperature curve may also prove useful. As was the case before with the histograms, results from the sensitivity analysis were only generated for the boiling location and not the evaporation location due to non-evaporating input sets causing the formulation of an erroneous PCE. Sobol indices for the boiling location can be seen in Figure 4.21.

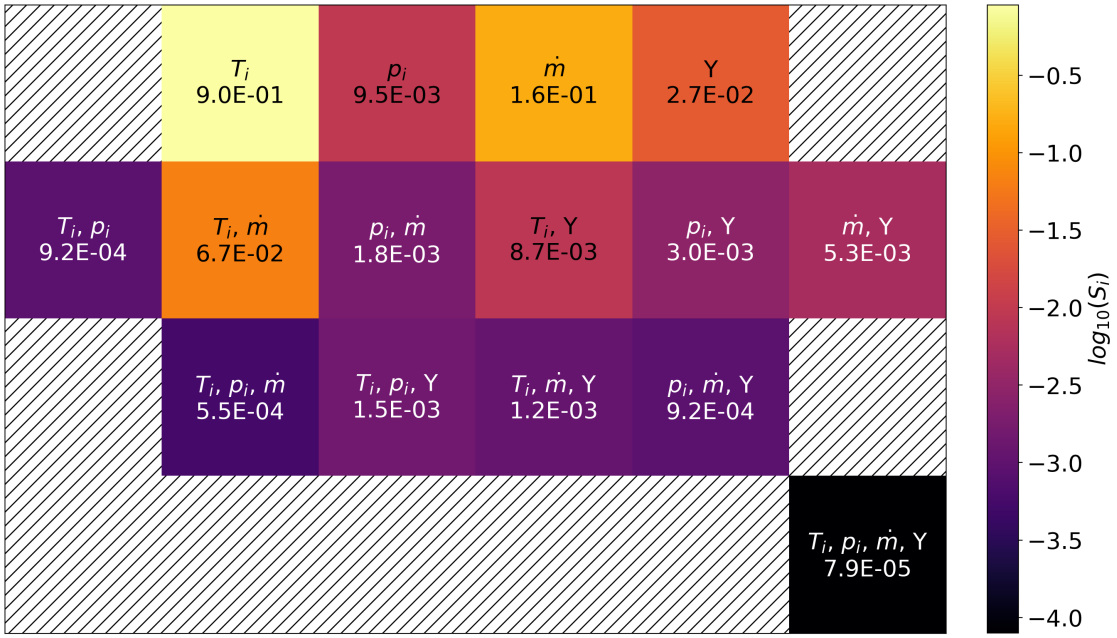

Figure 4.21: Sobol Index Grid for x_b for $\sigma = 0.01\mu$ in $T_i,\ p_i,\ \dot{m}$, and Y

The dominant variable affecting the location of transition from Region I to II is the inlet temperature with significant contributions from mass flow rate and the combination effect of the two. In a similar effort, a metric to describe the shape of the temperature curve was created. The aspect ratio AR is defined as follows:

$$AR = \frac{1}{w_1 w_2} \frac{x_{ev} - x_b}{L} \tag{4.2}$$

where w_1 and w_2 are coefficients in the following equation derived from a curve fit for the temperature curve in Region III.

$$T(x) = w_1 \left[1 - e^{-w_2 \Delta x^*}\right] \quad \text{where} \quad \Delta x^* = \frac{x - x_{ev}}{L} \tag{4.3}$$

Data for this analysis was generated using stochastic collocation, a stochastic expansion technique quite similar to PCE. More information on this technique can be found in the DAKOTA Theory Manual [22]. Sobol indices for the aspect ratio of the curve under uncertainty in the physical inputs can be seen in Figure 4.22.

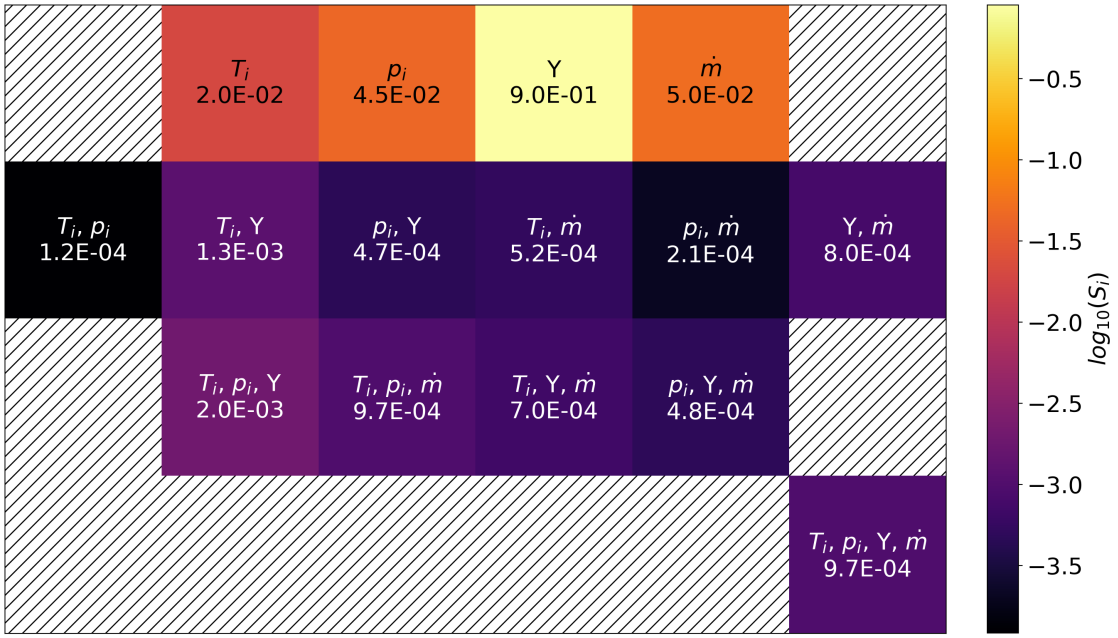

Figure 4.22: Sobol Index Grid for Aspect Ratio for $\sigma = 0.01\mu$ in $T_i,\ p_i,\ \dot{m}$, and Y

Once again, the dominating input for the response function is the concentration. Aspect ratio is closely linked to the concentration due to its strong impact on temperature and the resulting reaction advancement speed. Attempts were made to analyze the aspect ratio on a larger domain to obtain a more global set of sensitivities but as it depends on the evaporation parameter, determining the aspect ratio value for non-evaporating cases proved problematic.

To further evaluate aspect ratio sensitivities, an analysis was conducted while perturbing the tuning parameters in the model. The resultant sensitivities can be seen in Figure 4.23. The structure of the Sobol index grid is different from previous iterations as there were only 3 random inputs in the study. Aspect ratio of the temperature curve is primarily dictated by the activation energy E_{f2} with no significant nonlinear effects. It is also interesting to note that the adsorption equilibrium constant K_1 has the least effect which will be corroborated by the posterior distribution results in Section 4.4.

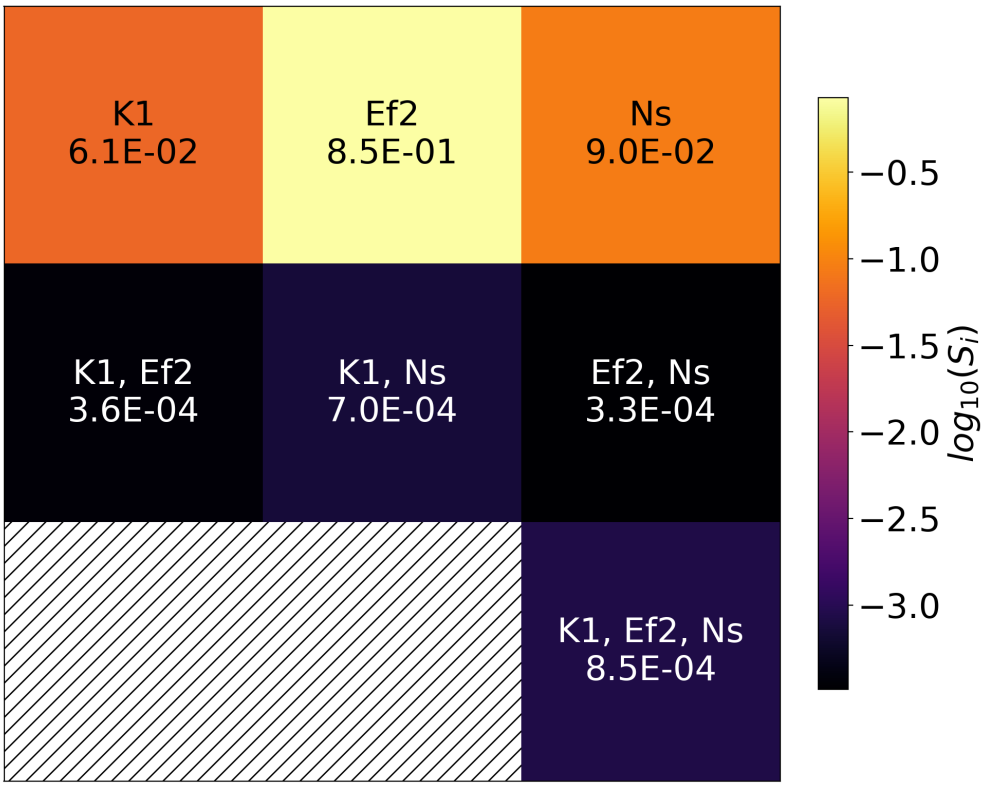

Figure 4.23: Sobol Index Grid for Aspect Ratio for $\sigma = 0.01\mu$ in E_{f2}, N_s, and K_1

4.4 Bayesian Inference Results

Bayesian inference was applied to the model in this study to establish confidence intervals in both the tuning parameters as well as the relevant output profiles for different experimental data sets. Data sets are composed of temperature data and pressure data at locations $\boldsymbol{x_T}$ and $\boldsymbol{x_p}$ respectively. Hypotheses for the Bayesian inference were randomly sampled sets of tuning parameters within a specified domain, equivalent to using uniform prior distributions. As was mentioned before, there is an element of subjectivity that arises due to the user defining the likelihood function. For the purposes of this inference, the likelihood function is the probability of the data at experimental temperature and pressure measurement locations $\boldsymbol{x_T}$ and $\boldsymbol{x_p}$ for Gaussian distributions defined by mean μ and standard deviation σ based on model predicted response function values. Mathematical representation of the likelihood

function, in which N represents the number of data points at a given location and N_T and N_p represent the number of temperature and pressure data points respectively, can be found along with a graphical representation below:

$$\text{prob}(Y|X,I) = 0.9\prod_{i}^{N_T}\text{prob}(Y_{T,i}|X,I) + 0.1\prod_{i}^{N_p}\text{prob}(Y_{p,i}|X,I)$$

$$\text{with} \quad \mu = T(\boldsymbol{x_T}), p(\boldsymbol{x_p}), \quad \sigma = \sqrt{\frac{1}{N-1}\sum_{k=1}^{N}(Y_k - \mu)^2}$$

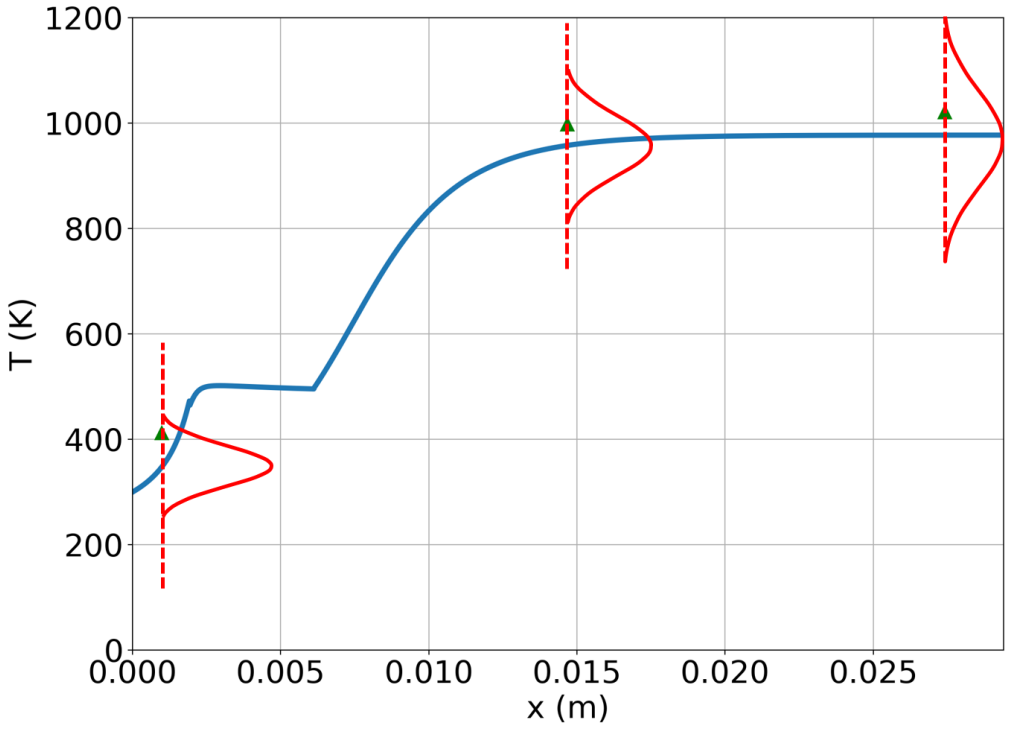

Figure 4.24: Example Model Temperature-Based Gaussian Distributions for Determining Likelihood Function

As was done when computing the error between the model at hand and that from Jung et al. [10], 90% weight was assigned to the temperature-based metric due its better predictive capabilities. Weights on the two likelihood functions were altered to see how this would

affect the resultant posterior distribution but a difference was negligible even for a pressure likelihood function weight of 99.99%. At each experimental data location, the mean of the Gaussian is the model-predicted value at that point and the standard deviation is based on each of the N experimental data points at that location. In the instance that there is only one data point at a given location, the mean is then treated as a data point to avoid a division-by-zero error. The standard deviation for the $N = 1$ case then becomes the following:

$$\sigma = \sqrt{\frac{1}{2-1}\left[(Y_1 - \mu)^2 + (\mu - \mu)^2\right]} = \sqrt{(Y_1 - \mu)^2}$$

Due to the sparsity of data at each location for a given test condition, additional mock data was created to provide better conditions for the formulation of the standard deviation at each experimental location as well as simply provide more input to the likelihood functions. Mock data sets included the experimental data for the standard case from Jung et al. and were designed not to glean exact numerical information but to have a representation of potential trends based on the form of the data.

Posterior probability distributions were generated using both data from direct simulation as well as surrogate data for various types of PCEs. Sampling details for each study can be seen in Table 4.4.

Samples	15000
E_{f2}	[12500, 17500]
N_s	[794, 1200]
K_1	[0.0008, 0.0012]

Table 4.4: Details of Monopropellant Model Bayesian Inference

Results from the Bayesian inference performed on the direct simulations can be seen in Figures 4.25 - 4.27. Each plot shows the 3D confidence interval distribution for a different set of orthogonal axes.

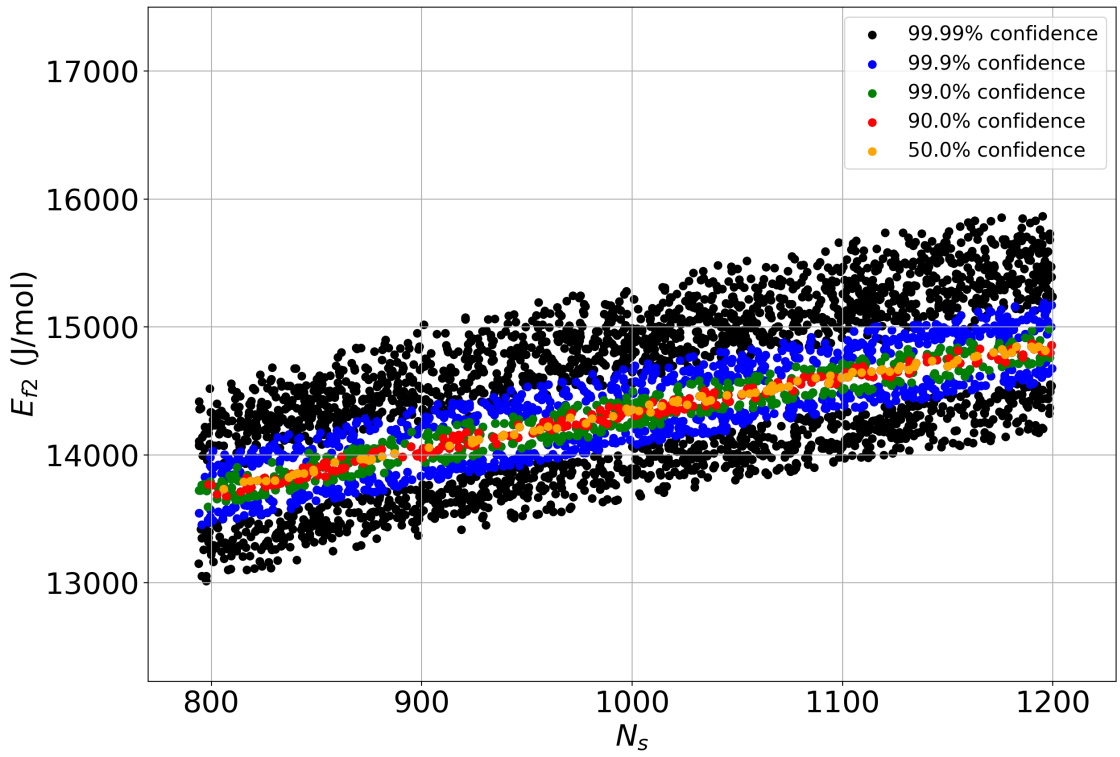

Figure 4.25: Posterior Probability Distribution for Direct Simulations in E_{f2} vs. N_s

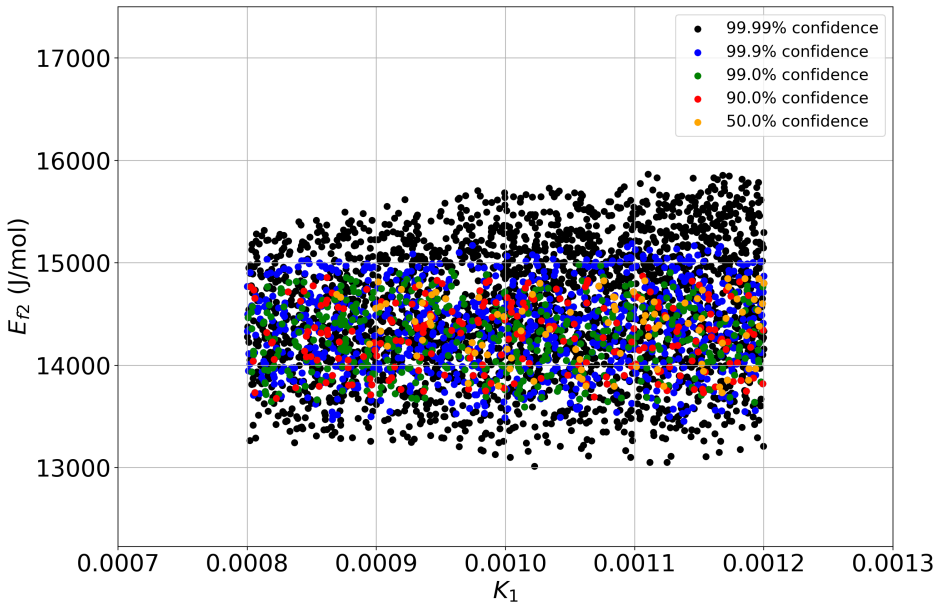

Figure 4.26: Posterior Probability Distribution for Direct Simulations in E_{f2} vs. K_1

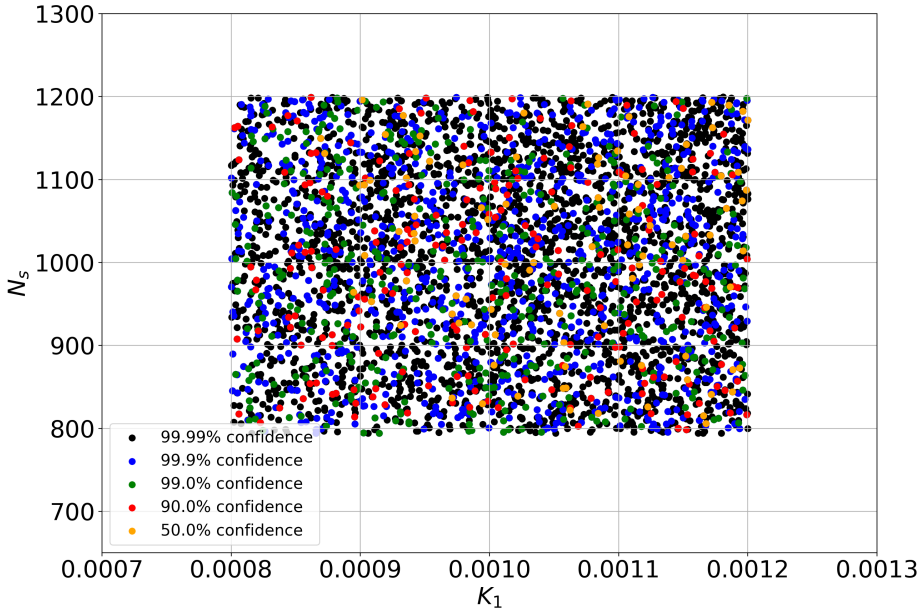

Figure 4.27: Posterior Probability Distribution for Direct Simulations in N_s vs. K_1

The posterior distributions above illuminate two key behaviors of the model. First, by observing Figure 4.25, it would appear that the optimal values of E_{f2} and N_s belong to a family of solutions based on the fact that none of the confidence intervals of the posterior distribution form closed shapes within the domain. This suggests that any combination of E_{f2} and N_s along a curve of the solution family will produce a sufficient solution. Referring to the reaction advancement gradient equation below, it can be seen that the tuning parameters E_{f2} and N_s can compensate for one another in achieving the optimal reaction rate.

$$\frac{\mathrm{d}\lambda}{\mathrm{d}x} = \frac{\dot{V}}{u} A_{f2} e^{-E_{f2}/\mathcal{R}T} N_s \frac{K_1 C^{(s)}_{\mathrm{H_2O_2}}}{1 + K_1 C^{(s)}_{\mathrm{H_2O_2}}}$$

It will be shown more clearly in Figure 4.31 that the relationship between the two tuning parameters is logarithmic which is to be expected based on the form of the reaction advancement equation. As N_s increases linearly, E_{f2} increases in a logarithmic trend to offset the increased reaction speed within a given confidence interval. While the exponential term does contain the spatially-varying temperature term, it appears that this has little effect on separating the logarithmic relation between E_{f2} and N_s. In order to achieve a set of optimal values not belonging to a family of solutions, an additional equation is required to decouple the two tuning parameters.

From the other two figures, it can be seen that the confidence intervals are not well defined and exhibit a great deal of overlap, even appearing totally random as in Figure 4.27. Based on this result, it is apparent that K_1 has very little impact on the results of the model. This is to be expected based on the form in which K_1 appears in the reaction advancement gradient. In effect, it could be removed from the tuning parameter optimization process to reduce the dimensionality of the problem with very little influence on the result.

As was mentioned previously, there were attempts to recreate these posterior distributions using PCE on several different grid types. The objective of this portion of the study was to determine how accurately each method could recreate the posterior distribution and in what fraction of the time. Table 4.5 contains completion times for each of the simulation methods with 15000 samples.

Simulation Method	Time (hours:minutes)
Direct Simulation	24:00
2^{nd} Order Sparse Grid	00:04
5^{th} Order Sparse Grid	01:22
Orthogonal Least Interpolation on Adaptively Sampled Grid	03:46

Table 4.5: Details of Monopropellant Model Bayesian Inference

Given the weak dependence on K_1, posterior distributions for the three surrogate models will only be shown for E_{f2} and N_s and can be seen in the figures below.

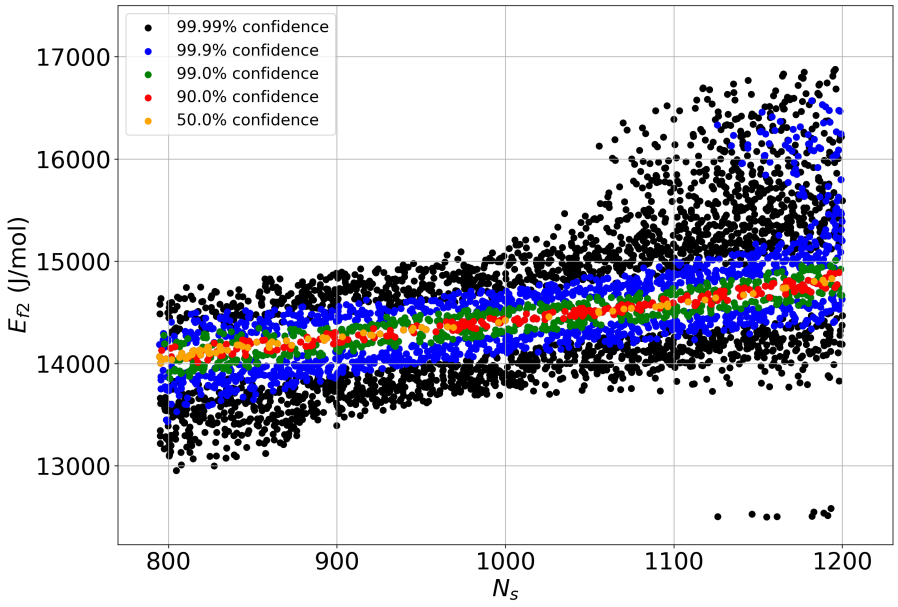

Figure 4.28: Posterior Probability Distribution for 2^{nd} Order Sparse Grid in E_{f2} vs. N_s

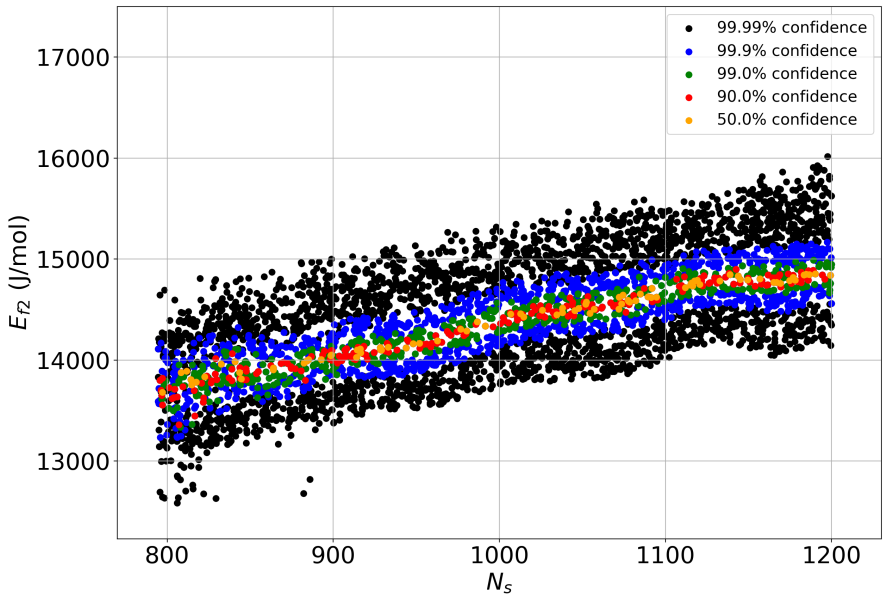

Figure 4.29: Posterior Probability Distribution for 5^{th} Order Sparse Grid in E_{f2} vs. N_s

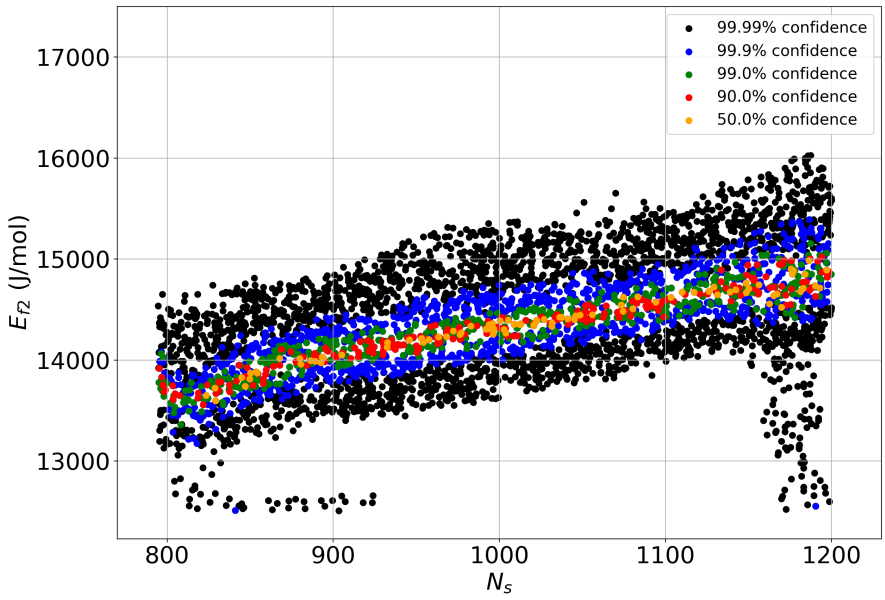

Figure 4.30: Posterior Probability Distribution for Orthogonal Least Interpolation on Adaptively Sample Grid in E_{f2} vs. N_s

Observing the figures above, using higher-order PCEs presents itself as an adequate method for rapidly generating posterior probability distributions. Quantitative comparison of PCE performance can be made by computing the Earth Mover's Distances (EMDs) between the directly simulated posterior distribution and the PCE generated posterior distributions. EMDs are computed comparing the 99.99% confidence intervals of the distributions with cluster representatives equal to the sample coordinates on the (N_s, E_{f2}) domain. Two EMDs were computed for each PCE, one in which each cluster was assigned an equal weight and one in which each cluster was weighted using the normalized posterior probability. The weighted EMD greatly increases the cost of moving high probability clusters while reducing the cost of moving low probability clusters. Table 4.6 contains the both EMD values for each PCE posterior.

Simulation Method	Uniform EMD (10^{-3})	Weighted EMD (10^{-3})
2^{nd} Order Sparse Grid	2.53	1.34
5^{th} Order Sparse Grid	0.169	0.486
Adaptively Sampled Grid	0.728	0.186

Table 4.6: PCE Generated Posterior Distribution to Direct Simulation Posterior Distribution EMDs

From the values presented in the table above, it can be seen that the 2^{nd} order sparse grid PCE results in EMDs approximately an order of magnitude larger than that of the other two methods and thus is the worst approximation of the directly sampled posterior. It is interesting to note that the 5^{th} order sparse grid has a lower uniform EMD than the adaptively sampled grid while the converse is true for the weighted EMD. This indicates that the posterior generated using the 5^{th} order sparse grid better represents the shape of the 99.99% confidence interval. This is to be expected due to the branching to solutions outside the expected family in the adaptively sampled case. On the other hand, the adaptively sampled case better reproduces the probability distribution of the directly sampled posterior distribution as it has a lower weighted EMD. While the solution branching near the domain

boundaries result in large ground distances for branches far from the directly simulated posterior, the weights of the distant clusters are orders of magnitude lower than those for the smaller confidence intervals.

A yet more accurate replication could likely be generated using a higher-order sparse grid or adaptively sampled grid although this inherently lends itself to longer computational times. For the 5^{th} order sparse grid, a reasonably accurate approximation of the confidence interval boundaries was generated in only $1/20^{\text{th}}$ of the computational time. Despite the potential benefits of applying PCE to Bayesian inference, its important to also consider the limitations of this technique. For all three PCE grid types, it appears that there is some degree of spread in the posterior near the domain bounds. This, in conjunction with the difficulty of formulating a polynomial approximation near a discontinuity in model behavior, means that PCE should only be applied to generate posterior distributions where the behavior of the model is stable and well-characterized and higher trust may want to be placed in an interior region of the PCE domain.

In order to further explore the behavior of the model, domain bounds were expanded roughly to the operating boundaries of the model for the activation energy E_{f2} and number of active sites N_s. Due to the simulations taking place close to the stability boundaries, it was deemed insufficient to use PCE to approximate the model results and thus it was necessary to use direct simulations. Details of the Bayesian inference can be found in Table 4.7.

Samples	20000
E_{f2}	[5000, 35000]
N_s	[250, 4500]
K_1	[0.0004, 0.0054]

Table 4.7: Details of Large Domain Direct Simulation Bayesian Inference

The posterior distribution resulting from the direct simulations described above can be seen below in Figure 4.31. The figure clearly shows the confidence intervals following a

logarithmic curve as was described earlier. One can also see that there is a series of points in the 99.99% confidence interval with lower activation energies that are separated from the main grouping of points. This offshoot occurs as the "probability benefit" of having even a marginally higher temperature for the last two data locations, by increasing the reaction rate, outweighs the cost of overshooting the data at the first location.

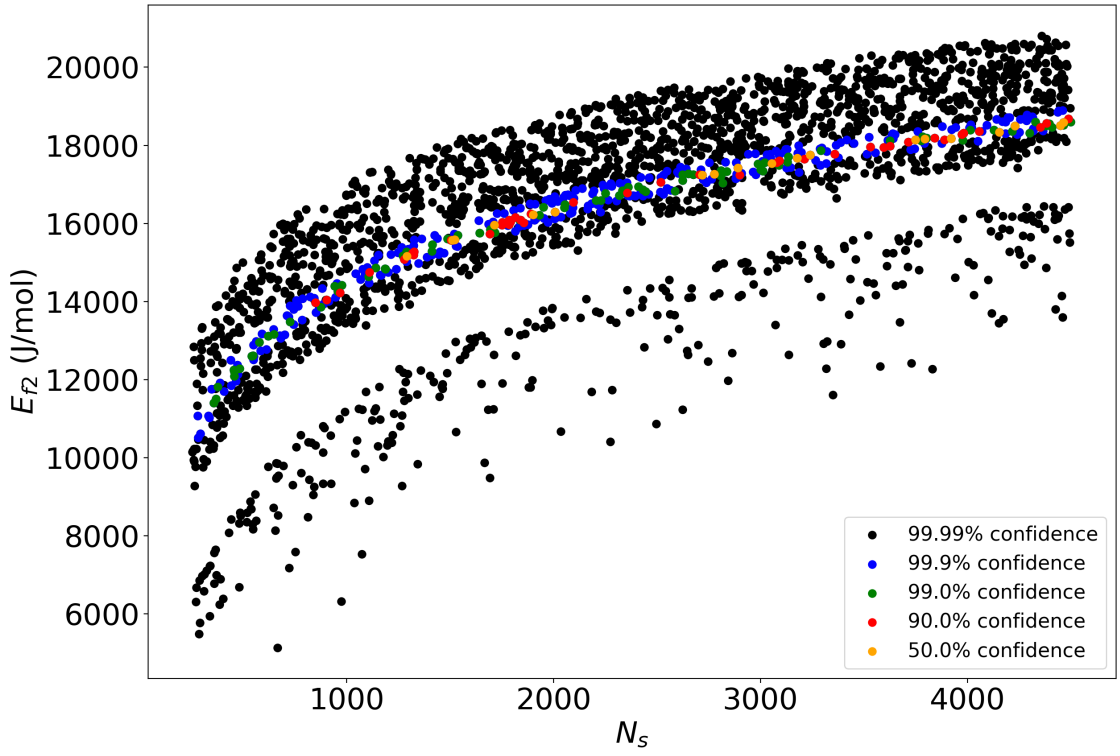

Figure 4.31: Posterior Probability Distribution for Large Domain Direct Simulations in E_{f2} vs. N_s

It is important to recall that each of the posterior distributions above were created using a representative mock data set. For the large domain direct simulations, the same Bayesian inference techniques were applied using the original standard case data set from Jung et al. [10] which can be seen in Figure 4.32.

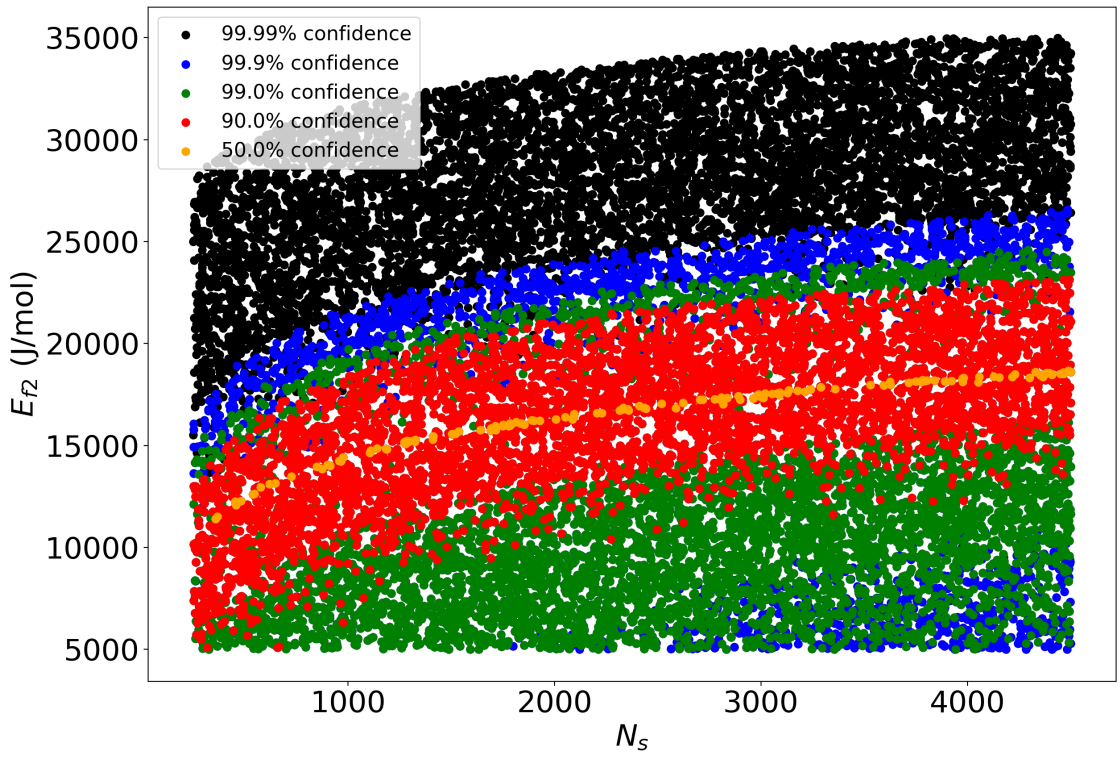

Figure 4.32: Posterior Probability Distribution for Large Domain Direct Simulations in E_{f2} vs. N_s for Standard Case Data Set [10]

Immediately it can be seen that the confidence intervals are much larger as compared to the posterior distribution for the mock data set. Because of the reduced number of data points, the probability penalty for unlikely hypotheses is much less significant. Despite this confidence interval broadening, the same general trends can be seen in both posterior distributions in that there is an apparent logarithmic trend. Using the 50% confidence interval, it is possible to construct a logarithmic curve of best fit to determine the relation between E_{f2} and N_s. The logarithmic curve is governed by the following equation:

$$E_{f2} = \psi_1 \log(N_s) + \psi_2$$

Curve fits for both the mock data set and the standard case data set can be seen in Figures

4.33 and 4.34 respectively. Values for the coefficients ψ_1 and ψ_2 for each curve fit can be found in Table 4.8.

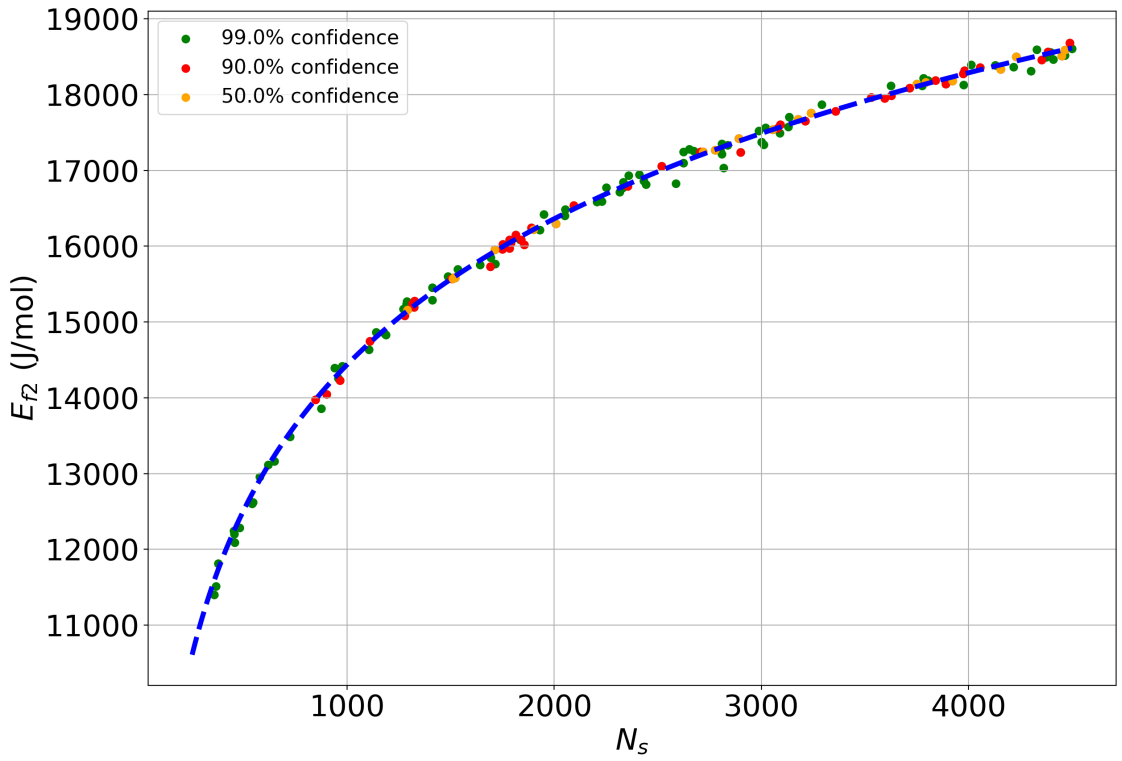

Figure 4.33: 50% Confidence Interval Curve Fit for Mock Data

While the best curve fit is based solely on the 50% confidence interval, simulations from the 90% and 99% confidence intervals are shown to further elucidate the logarithmic trend.

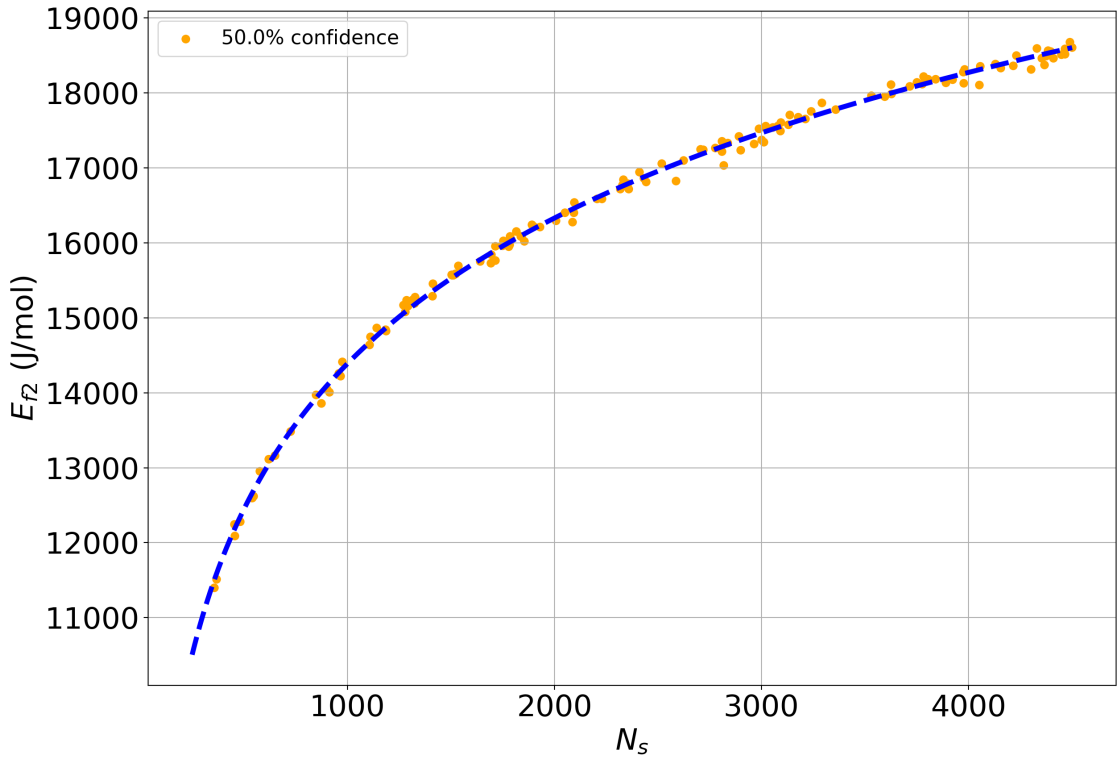

Figure 4.34: 50% Confidence Interval Curve Fit for Standard Case Data

Data Set	ψ_1	ψ_2
Mock Data	2778.3	-4755.1
Standard Case	2802.7	-4973.2

Table 4.8: 50% Confidence Interval Logarithmic Curve Fit Coefficients

Coefficients for the standard case were used to determine the activation energy values corresponding to $N_s = 500$ and $N_s = 3000$. These tuning parameter sets were then used to generate the respective temperature profiles which are compared on the same axes in Figure 4.35. In both simulations, K_1 was held at the nominal value of 0.001079.

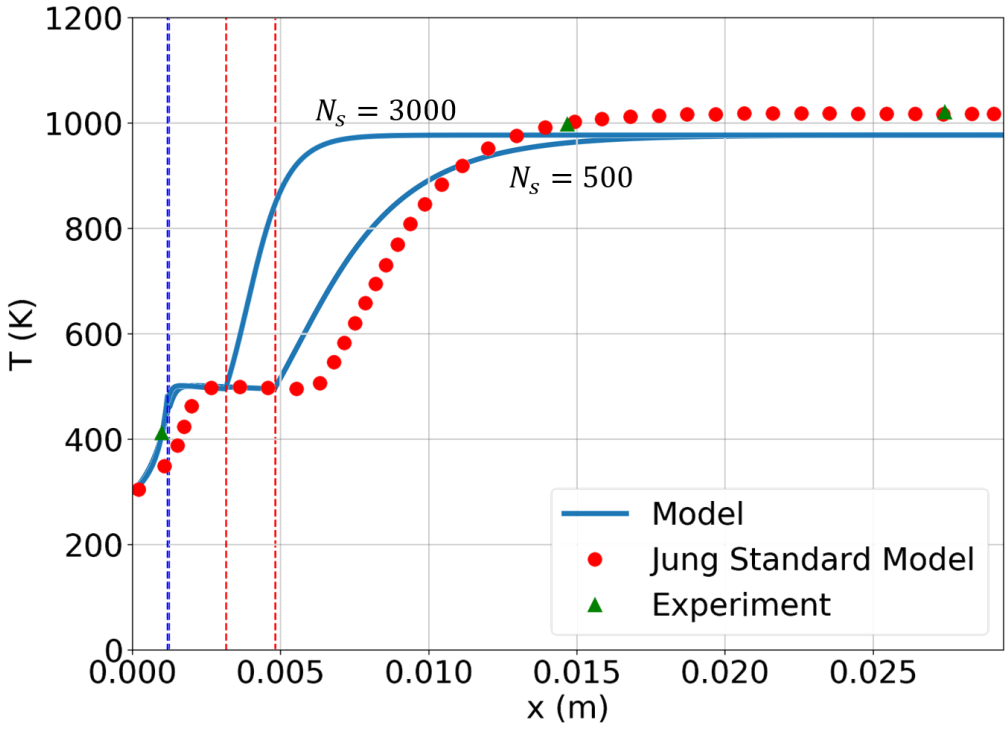

Figure 4.35: Comparison of Temperature Profiles for $N_s = 500$ and $N_s = 3000$ with Curve Fit E_{f2} (Jung Standard Case Model Data Shown for Reference)

Both profiles achieve temperatures approximately equal to that of the first experimental data point while the Jung et al. profile does not. This is likely due to the fact that the Jung et al. tuning parameters were calibrated across multiple test cases as opposed to solely the standard case as is being done in the study at hand. Further discussion of utilizing additional test cases can be found in Section 5. There is an extremely large variation in the potential temperature profiles that would constitute a high confidence result. At $x \approx 0.005$ m, there is a nearly 400 K difference between the two profiles. This is primarily due to the small temperature variation between the last two experimental data points. Because little changes between the second and third data point, there is no significant information gained from including the final point. However, if the second data point had a lower temperature and fell on the highly varied portion of the temperature curve in Region III (for example

$T = 700$ K), then variation between results for a confidence interval would be greatly reduced. While the figure shown above only demonstrates a comparison between two arbitrary curves based on the logarithmic fit, it is possible to show the same confidence intervals from the posterior distribution on the axial property profiles. This is done by taking the highest and lowest property values at each node corresponding to a set of tuning parameters within a given confidence interval. Confidence intervals are demarcated by gray dotted lines with gray infill and confidence intervals expand outward in the same fashion as for the posterior distributions i.e. 50%, 90%, etc. Once again, mock data sets were used in order to be able to customize the data spread and location and evaluate the corresponding effects on the confidence intervals. The axial temperature profile with confidence intervals generated with the original mock data can be seen in Figure 4.36. It is worth noting that the optimum profile is the temperature profile predicted by the maximum probability hypothesis and that each confidence interval may contain a percentage of samples different from the respective confidence interval's percentage. This is due to the confidence interval boundaries stemming from the tuning parameters as opposed to the property distribution at each node.

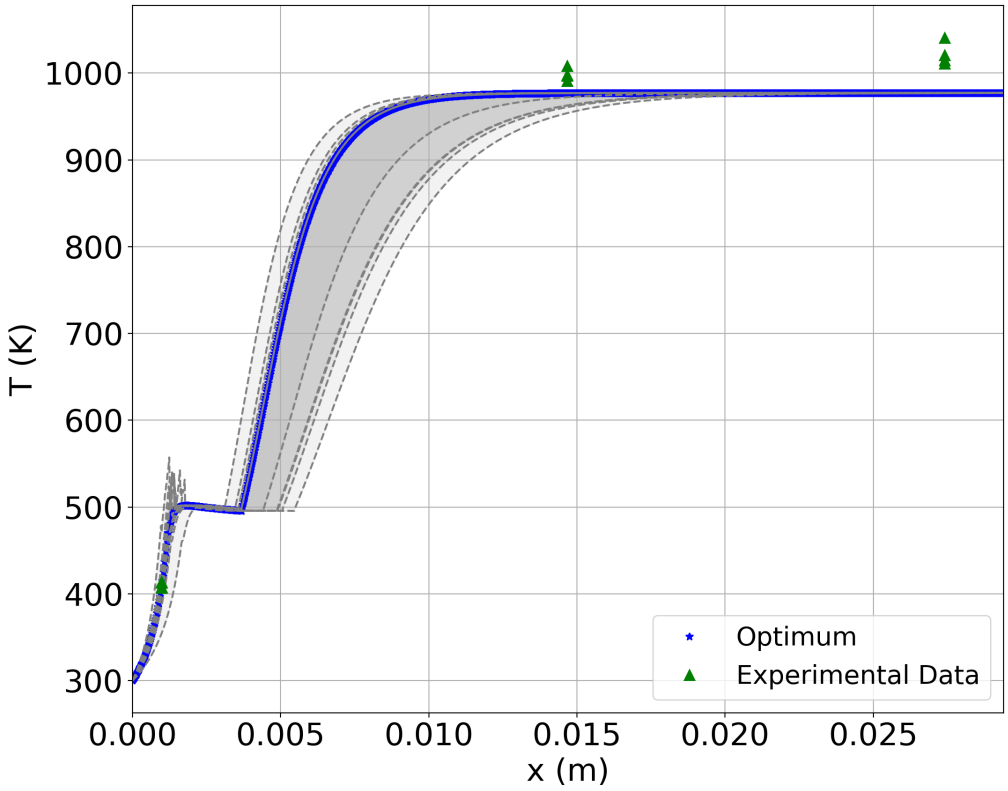

Figure 4.36: Axial Temperature Profile with Confidence Intervals for Mock Data

Noise in the temperature value around the Region I to Region II transition is due to the variation of values permitted by the discontinuity for a range of tuning parameter sets. It can be seen, similar to Figure 4.35, that there is high temperature variance around $x = 0.005$ m. By including additional experimental data in approximate accordance with the maximum probability profile to a region of low confidence, one would expect the confidence interval bounds to shrink. This phenomenon can be observed in Figure 4.37 in which an additional 4 synthetic data points were added for both temperature and pressure at $x = 0.006$ m.

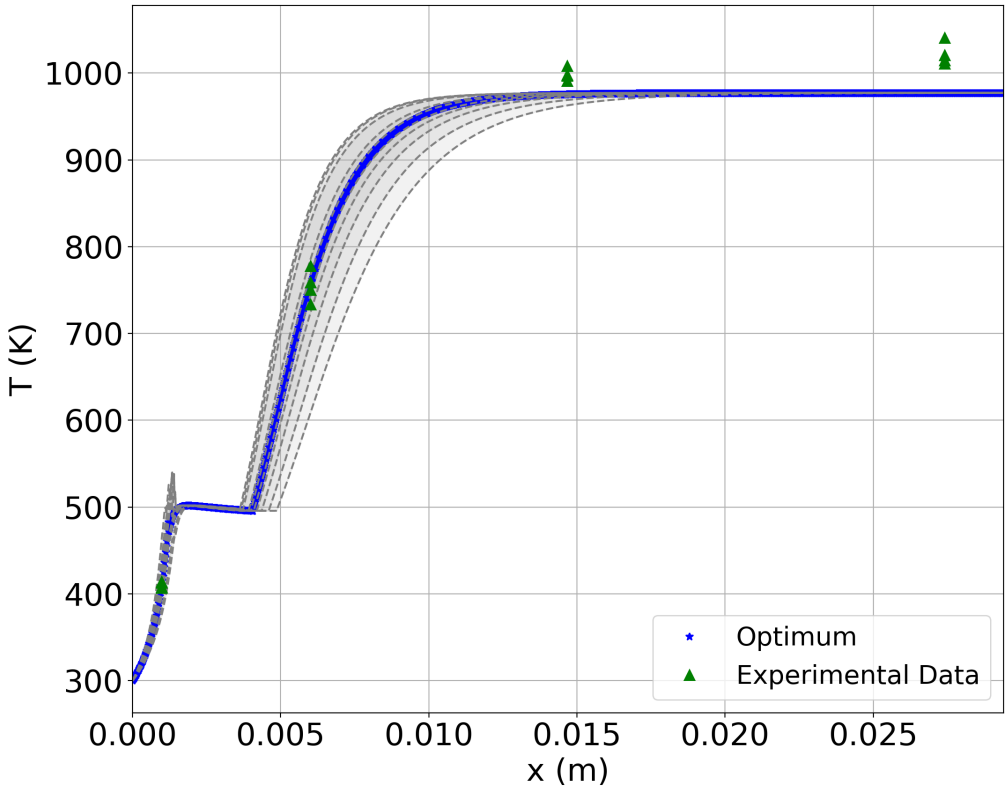

Figure 4.37: Axial Temperature Profile with Confidence Intervals for Mock Data with Optimal Low Confidence Data

In contrast to Figure 4.37, the confidence interval bounds expand in this instance that the additional data is outside the expected confidence intervals or the predictive capabilities of the model. If instead of adding data points close to the optimal profile, data points closer to the complete decomposition temperature are added, the variance in the confidence interval data bounds increases. This can be seen in Figure 4.38.

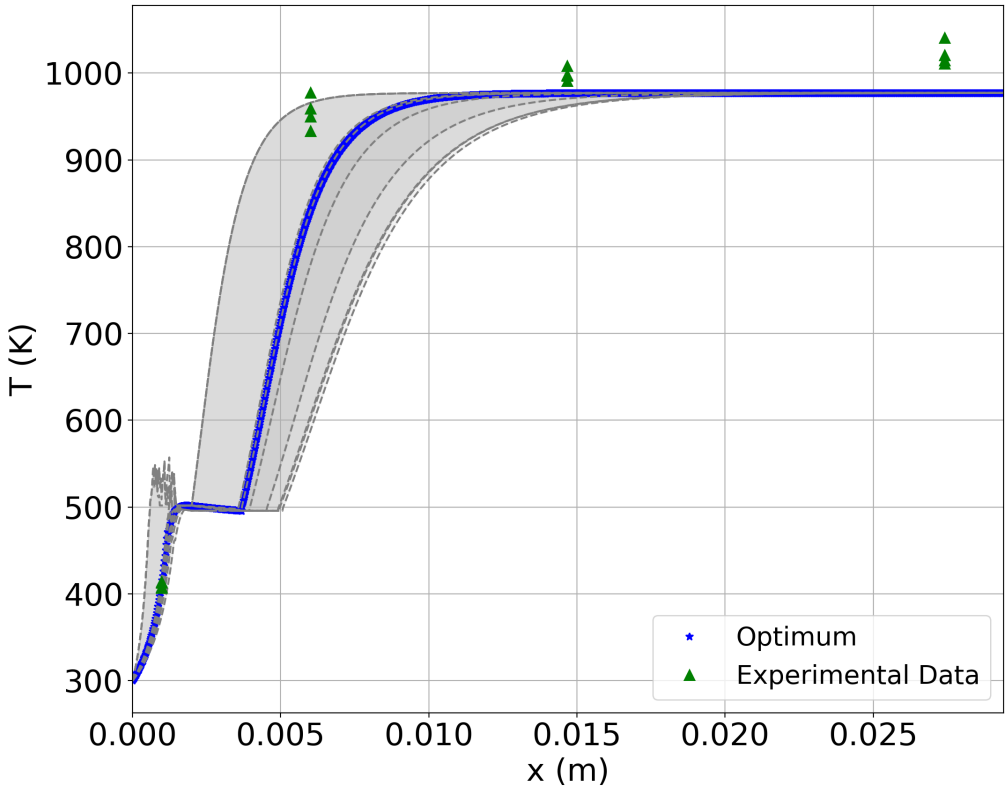

Figure 4.38: Axial Temperature Profile with Confidence Intervals for Mock Data with Non-Optimal Low Confidence Data

It can be seen in the figure above that the upper bounds for each of the confidence intervals seem to collapse into a single value indicated by a single dotted line. This occurs because each of the confidence intervals extends to the boundary of the study domain. In other words, the 50% confidence interval contains the domain boundaries leading to the fastest possible reaction rates in the domain.

While the addition of experimental data to a region of low confidence, or high response function variation, can significantly alter response function boundaries prescribed by the confidence intervals, it is worth examining the effects of adding data in a region of high confidence. As the fluid approaches the catalyst bed outlet, the temperature asymptotically

approaches the complete decomposition temperature of the mixture, a quantity independent of the tuning parameters, and the confidence intervals shrink. Figure 4.39 contains the axial temperature profile with confidence intervals for the mock data set with additional data at $x = 0.022$ m.

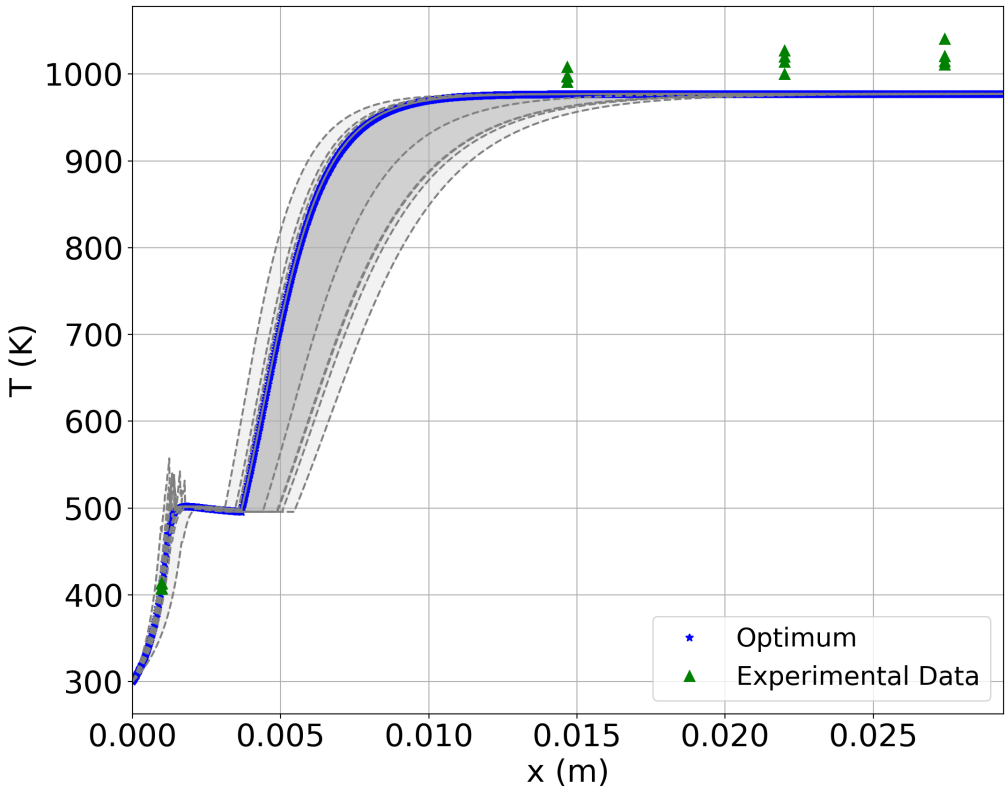

Figure 4.39: Axial Temperature Profile with Confidence Intervals for Mock Data with High Confidence Data

From the figure above, it can be seen that the addition of high confidence data has negligible impact on the confidence intervals as compared to those in Figure 4.36. Acquisition of data in locations of the low confidence is critical for refining confidence intervals and increasing the confidence in model predicted values. While moving pressure transducers and thermocouples may prove laborious and impractical, it is entirely feasible to shift the region

of uncertainty by altering the input conditions. Model predictions and experimental data from Jung et al. [10] in Section 2.2.1 show that the rapid temperature increase in Region III can be delayed by reducing the concentration of H_2O_2 or increasing the mixture mass flow rate. For this reason, calibration on these cases may prove more fruitful in terms of refining the confidence intervals for single case calibration.

CHAPTER 5

Conclusions and Future Directions

Work presented in the study at hand explored parameter sensitivity and uncertainty propagation through the monopropellant catalyst bed model proposed in Pasini et al. [9]. The model is capable of predicting temperature within the catalyst bed with reasonable accuracy but is a poor predictor of pressure. Good agreement was shown between the model and experimental data in 5/6 test cases with reasons for the deviation in the final case remaining unknown. An attempt to modify the model in order to predict mixture properties for a HAN-H_2O mixture was made but due to significantly different behavior than H_2O_2 and a lack of validation data, the resulting model will require further attention to attain sufficient predictive capabilities. Results have shown that model behavior exhibits a strong dependence on the reference enthalpies of liquid H_2O_2 and H_2O in both phases. Model behavior is also highly sensitive to the activation energy and number of active sites per unit volume. Sensitivity analysis of the model also indicates that outlet temperature and pressure loss through the catalyst bed are predominately determined by the initial propellant mass fraction. Propellant mass fraction is also the most sensitive of the physical inputs in determining the aspect ratio of the temperature profile while the primary tuning parameter in affecting the aspect ratio is the activation energy.

Bayesian inference on the model revealed the coupled nature of the tuning parameters E_{f2} and N_s and the weak-dependence on K_1. It was found that confidence intervals established on the 3D probability distribution formed surfaces that followed logarithmic curves in E_{f2} and N_s with little variation in the K_1 direction. This is not a reflection of real world behavior but instead implies that the model at hand requires another equation to decouple E_{f2} and N_s. Logarithmic curve fits were established for both mock experimental data and for the

standard case experimental data to evaluate the relation between E_{f2} and N_s. By plotting multiple temperature profiles for different values of the two tuning parameters based on the standard case curve fit, it was seen that the profiles were highly varied in Region II and early Region III but had similar probabilities due to passing through the first experimental data point.

Generation of posterior distributions was also performed using PCEs for different grid types which was deemed a viable method for well-behaved and well-characterized domains but not for expansion into unknown model territory. Using the same inference techniques, confidence intervals were used to create boundaries on the axial temperature profile. Axial profile confidence intervals responded as expected to several mock data sets; confidence increases and boundaries tightened with the addition of data within existing intervals in areas of high uncertainty. Conversely, boundaries expanded with the addition of data outside the intervals in the same area and were negligibly affected with data addition in regions of low certainty. Future catalyst bed experiments should have a temperature probe placed in the predicted area of rapid temperature increase in Region III for the nominal test conditions. Mass flow rate and propellant concentration can be tuned such that some temperature indicative of partial decomposition can be measured at that location thereby establishing experimental data in a region of low confidence.

Both predictive deficiencies in the reduced-order model and the extensiveness of the UQ field present ample opportunity for further developments on the model and its analysis. To enhance the robustness of the model's property profile prediction with uncertainty envelopes for uncertainty in the physical system inputs ($T_i,\ p_i,\ \dot{m}$, and Y), the median with sampling distance method should be replaced with the maximum likelihood estimate and confidence interval method. While it would be unexpected to have bimodal or otherwise obscure property distributions in which using the median with sampling distance would be insufficient, having the capability to accurately represent those distributions, as well as having the maximum likelihood estimate represented, is an optimal configuration. An attempt was made to generate the axial uncertainty profiles using confidence intervals but was met with little

success. This was primarily due to sampling density being too low to generate well-formed property distributions at each node. Unlike the mean and median, to achieve the highest probability result each sample needs to be binned in order to have a representation of the probability density function of the distribution. In order to have a sufficient number of properly filled bins, a large number of samples is required which the author had difficulty generating using GSB. The best attempt generated a coarse approximation of the distribution with few bins that resulted in grainy confidence intervals and maximum likelihood estimate profiles as the aforementioned values would shift discontinuously from node to node. It may be possible to generate confidence intervals and the maximum likelihood estimate from distribution statistics approximated using the same number of samples and bins. This would then allow for the optimal property profile and uncertainty bounds to be smoothly generated with the caveat that additional uncertainty is introduced by approximating the property distribution.

Property profiles with confidence intervals and the corresponding posterior distributions based on the 3 tuning parameters were generated using mock data and experimental data for the Jung et al. standard case. A more rigorous analysis using the Jung et al. experimental data for the 5 successfully validated test cases could be conducted to provide a more substantial base of experimental data for the property profiles and posterior distributions. Likelihood functions would be computed for each test case in the manner described for the standard case earlier in the text and their multiplicative sum would be the posterior probability. Because each test case has different physical inputs, this method would require running the code 5 separate times for each hypothesis and for this reason, the computational time required to conduct the analysis through direct simulation rendered the study intractable given the author's time constraints. It may be possible to approximate the results using PCE but, as was mentioned earlier in Section 5, the author experienced some difficulty in obtaining large amounts of data using GSB. While using a each test case would allow one to obtain a more accurate posterior distribution, it would likely result in a similarly shaped distribution as for the single case distribution because the governing equations, and therefore

underlying behavior, is independent of the test case. Using additional test cases is essentially the same as adding more data points to one case but yields the advantage of more robustly defining the confidence intervals as to be sensitive to variation in the physical inputs.

To improve the predictive capabilities of the H_2O_2 model, it seems necessary to implement a higher fidelity reaction mechanism. Currently, the model makes use of a single global reaction with no account for local sub-reactions. Increasing the number of chemical reactions and product species would be a simple way to more accurately represent the reaction taking place far from the outlet and provide a better estimate regarding intermediate property evolution. Using the same reaction advancement parameter architecture implemented in the model at hand, increasing the number of governing ODEs should pose little difficulty. Including additional reactions, while increasing model fidelity, increases the number of system tuning parameters and assuming the reactions are driven by Arrhenius rates, they may exhibit the same coupling behavior shown in the current study. Regardless of the reaction fidelity, decoupling E_{f2} and N_s would be advisable as it would allow for the establishment of closed posterior probability distributions for the tuning parameters and thus formulation of more well-defined confidence intervals. Further research must be conducted to determine an appropriate constraint to decouple the two parameters.

In addition to supplementing the model's reaction mechanism, improvements should also be made to the pressure prediction capabilities of the model. One possible way to do so would be to convert the model from a mixture model to a multifluid model that separately treats the properties in the liquid and gas phases such as in Koopmans et al. [17]. Currently it is assumed that the temperature, pressure, and species concentrations are uniform for both phases, ignoring any variation and interaction between the two phases. Accounting for interfacial friction between the phases and temperature variation, which would allow for higher-fidelity calculation of the fluid properties, could yield significant benefits in terms of improving model pressure prediction.

It would also be prudent to develop alternate region transition conditions as to avoid the discontinuity between Regions I and II. By switching to a multifluid model, using the

pressure-based definition of boiling may result in a less severe discontinuity at the transition location. Other methods of reducing the severity of the discontinuity would be to implement an adaptive ODE solver that could increase the grid resolution near region transitions. This would also yield the benefit of reducing the fidelity in region of low variation like near the catalyst bed outlet. Another method, which could also work in conjunction with an adaptive method, would be to use a coarse step size and upon reaching region transition, restart to slightly before the transition with a finer step size. This process could be repeated until a desired grid resolution is reached and returning the step size to the original resolution for the remainder of the simulation. While the aforementioned methods may ameliorate the discontinuity in some faculty, some degree of discontinuity is inherent in the model structure. Because the growing concentration of O_2 is ignored in Region I and accounted for in Region II, some property discontinuity will be present regardless of spatial resolution implemented in the ODE solver.

Significant effort is required to improve the HAN-H_2O model as it currently exhibits deficiencies in predicting both spatial temperature evolution and mixture behavior. Currently, temperature evolution through the bed is highly dependent on the initial mixture temperature and tuning parameters for the model have yet to be calibrated using experimental data. Conditions required for transitioning to Regions II and III are ill-suited for two main reasons: the initial temperature is greater than the boiling temperature of H_2O and the three region mixture model may be unsuitable for HAN-H_2O on the whole. The first point is the primary cause for the model skipping Regions I and II in the first few nodes in the domain. Secondly, using a three region mixture model may be inappropriate because, as was mentioned earlier in Section 2.2.2, the actual evaporation and reaction mechanisms of the mixture deviate from the mixture-based behavior. In the liquid phase, H_2O begins to vaporize prior to HAN [20] yet evaporation of individual species is neglected in the present model. While it is possible that the three-region simplification is sufficient for the purposes of reduced-order modeling, experimental data is required to ascertain the validity of such a claim.

Uncertain variables in this study were provided no rigorous classification into the two primary types of uncertainty: aleatory and epistemic. Aleatory uncertainties are classified as the irreducible uncertainties that are inherent in nature while epistemic uncertainties stem from a lack of information and thus can be further reduced [28]. Classifying the uncertain variables facilitates the usage of a hybrid methods that approach the implementation of aleatory and epistemic variables separately. Such hybrid methods could prove more useful if using the model at hand as a predictive tool as it would allow for quantification of confidence intervals not only for variation in tuning parameters but also for variation in the physical inputs and other model parameters. The Bayesian calibration performed in this study can be considered a purely epistemic form of UQ whereas the variation in the physical inputs would represent aleatory uncertainties. They too could be included in the Bayesian calibration but would likely have minimal impact on the form of the results (logarithmic relation between E_{f2} and N_s) due to the persistent form of the model governing equations. Additionally, to include the aleatory uncertainties would greatly increase the computational rigor required to generate the confidence intervals and, if using GSB, may introduce the errors characteristic of large data files as experienced by the author. For this reason, a hybrid method should be restricted to conducting predictive studies ideally with few response functions.

To further refine the uncertainty quantification studies performed on the model, it is important to not only classify the existing uncertainties but to seek values for untreated uncertainties. The study at hand made no consideration of model uncertainty nor surrogate error. Uncertainty from discretizing the domain can be assumed to be negligible as it was verified that the model results were grid independent with the given step size. Some idea of surrogate error can be gathered by comparing surrogate evaluations to high fidelity data that the surrogate model was not trained on but primary interest should be devoted to quantifying model error. Considering that the model at hand is a reduced-order model, it is no surprise that the pressure predictions differed significantly from the experimental data. For this reason, application of a model discrepancy function could greatly assist in pressure predictions. The model discrepancy function compensates for insufficient model accuracy

and acts to emulate behavior seen in experimental data [29]. It is possible to generate the model discrepancy function as a Gaussian process emulator using GSB which would improve the predictive capabilities of the model significantly.

APPENDIX A

Fluid Properties

A.1 Molar Masses

	H_2O_2	H_2O	O_2
$\mathcal{M}$ (g/mol)	34.0147	18.0153	31.9988

Table A.1: Species Molar Masses [30]

A.2 Reference Enthalpies

	$H_2O_2, (l)$	$H_2O_2, (g)$	$H_2O, (l)$	$H_2O, (g)$	O_2
h° (J/mol)	-187341.0	-135453.0	-285825.0	-241831.0	0.0

Table A.2: Species Reference Enthalpies [30]

The above values correspond to a reference temperature of $T^\circ = 298.15$ K.

A.3 Specific Heats

Specific heats for species in units of J/mol·K in the H_2O_2 model are computed using the following temperature-dependent polynomial with coefficients found in Table A.3:

$$c_p = A + Bt + Ct^2 + Dt^3 + Et^{-2} \quad \text{where} \quad t = T/1000$$

Coefficient	$H_2O_2, (g)$	$H_2O, (l)$	$H_2O, (g)$	O_2 ($T \leq 700$ K)	O_2 ($T > 700$ K)
A	34.25667	-203.606	30.09200	31.32234	30.03235
B	55.18445	1523.29	6.832514	-20.23531	8.772972
C	-35.15443	-3196.413	6.7934535	57.86644	-3.988133
D	9.087440	2474.455	-2.534480	-36.50624	0.788313
E	-0.422157	3.855326	0.082139	-0.007374	-0.741599

Table A.3: Coefficients for Specific Heat Polynomials [17]

The specific heat for $H_2O_2, (l)$ is a constant 89.377 J/mol·K.

A.4 Saturation Pressures

Saturation pressures in units of mmHg are computed using the following temperature-dependent relation with coefficients found in Table A.4:

$$\log_{10} p_{sat} = A + \frac{B}{T} + C\log_{10} T + DT + ET^2 + FT^3 + GT^4$$

Coefficient	H_2O_2 ($T < 363.15$ K)	H_2O_2 ($T \geq 363.15$ K)	H_2O
A	24.8436	38.8572	19.389127
B	-3511.54	-3627.72	-2861.9133
C	-4.61453	-11.2133	-3.2418662
D	-3.60245E-3	4.74132E-3	-1.0799994E-4
E	-7.73423E-6	0	-7.9189289E-6
F	1.78355E-8	0	1.5411774E-8
G	-2.27008E-13	0	-8.1926991E-12

Table A.4: Coefficients for Saturation Pressure Relation [31]

A.5 Species Densities

Density for liquid H_2O_2 in kg/m^3 can be calculated using the following equation [32]:

$$\rho_{H_2O_2,(l)} = 1597 + 0.0784 - 0.00197T^2$$

The above equation is valid for $273 < T < 425$ K but will be assumed to hold outside this range.

Density for liquid H_2O in kg/m^3 can be calculated using the following equations [17]:

$$\rho_{H_2O,(l)} = \frac{1000}{1 + 18.159725 \cdot 10^{-3} \cdot T_C} \left(0.9998396 + 18.224944 \cdot 10^{-3} \cdot T_C - 7.92221 \cdot 10^{-6} \cdot T_C^2 \right.$$
$$\left. -55.44846 \cdot 10^{-9} \cdot T_C^3 + 149.7562 \cdot 10^{-12} \cdot T_C^4 - 393.2952 \cdot 10^{-15} \cdot T_C^5\right)$$

where T_C is the temeperature in degrees Celsius.

A.6 Dynamic Viscosities

Dynamic viscosity in Pa·s for liquid and low-temperature gaseous H_2O is determined using the following equation:

$$\mu = A + BT + CT^2 + DT^3 + ET^4 + FT^5$$

where the coefficients are determined by using a polynomial fit to data from NIST [33]. The coefficients can be found in Table A.5.

Coefficient	$H_2O, (g)$ ($T < 373.2$ K)	$H_2O, (l)$
A	-4.16400E-4	8.75554E-2
B	5.17967E-6	-9.02487E-4
C	-2.50157E-8	3.71610E-6
D	5.97869E-11	-7.60852E-9
E	-7.03094E-14	7.73276E-12
F	3.25843E-17	-3.11856E-15

Table A.5: Coefficients for Dynamic Viscosities of Liquid and $T < 373.2$ K Gaseous H_2O

Dynamic viscosity in Pa·s for high-temperature gaseous H_2O and O_2 is determined using the following equation with coefficients shown in Tables A.6 and A.7 respectively [34]:

$$\mu = 10^7 \exp\left(A \ln T + \frac{B}{T} + \frac{C}{T^2} + D\right)$$

Coefficient	$H_2O, (g)$ $(373.2 \leq T \leq 1073.2$ K)	$H_2O, (g) (T > 1073.2$ K)
A	5.0019557E-1	5.8988538E-1
B	-6.9712796E2	-5.3769814E2
C	8.8163892E4	5.4263513E4
D	3.0836508E0	2.3386375E0

Table A.6: Coefficients for Dynamic Viscosities of $T \geq 373.2$ K Gaseous H_2O

Coefficient	$O_2, (g) (T < 1000$ K)	$O_2, (g) (T \geq 1000$ K)
A	6.0916180E-1	7.2216486E-1
B	-5.2244847E1	1.7550839E2
C	-5.9974009E2	-5.7974816E4
D	2.0410801E0	1.0901044E0

Table A.7: Coefficients for Dynamic Viscosities of O_2

For both phases of H_2O_2, it was assumed that the viscosity was equal to 0.975 of that corresponding to the same phase in H_2O. This is based on a comparison of viscosity values for $H_2O, (g)$ and $H_2O_2, (g)$ for $373 < T < 573$ K based on data from NIST [33] and Satterfield et al. [35] respectively. In this temperature range, the viscosity of gaseous H_2O_2 was on average 0.975 that of gaseous H_2O. This trend was then assumed to be sufficient outside the temperature range and for liquid H_2O_2.

APPENDIX B

Additional Figures

B.1 Histograms

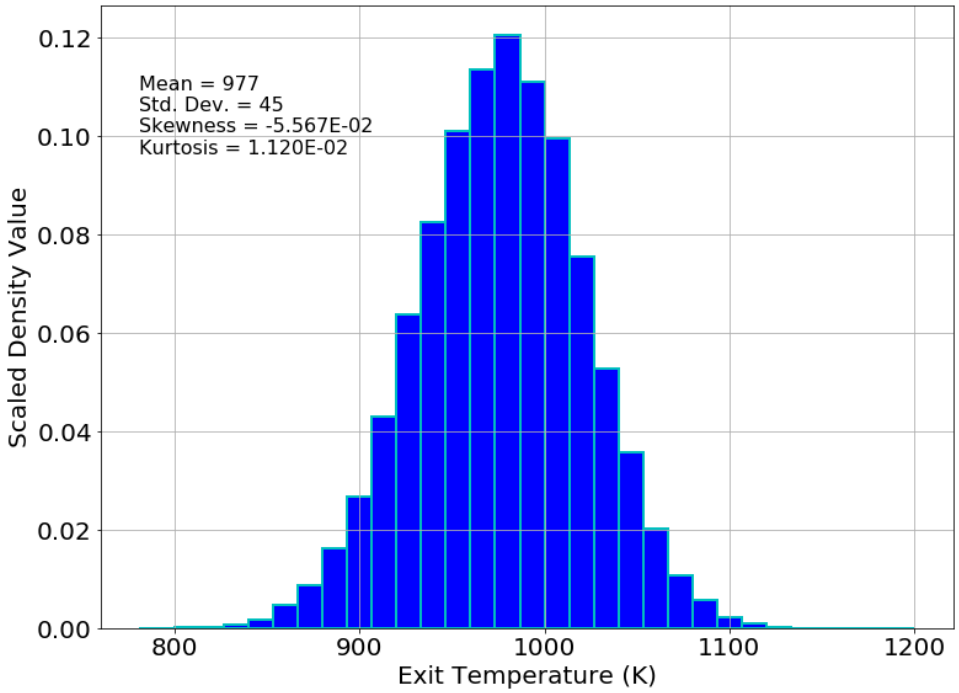

Figure B.1: Distribution of T_{end} for $\sigma = 0.01\mu$ in H_2O_2 and H_2O Reference Enthalpies

B.2 Property Profiles

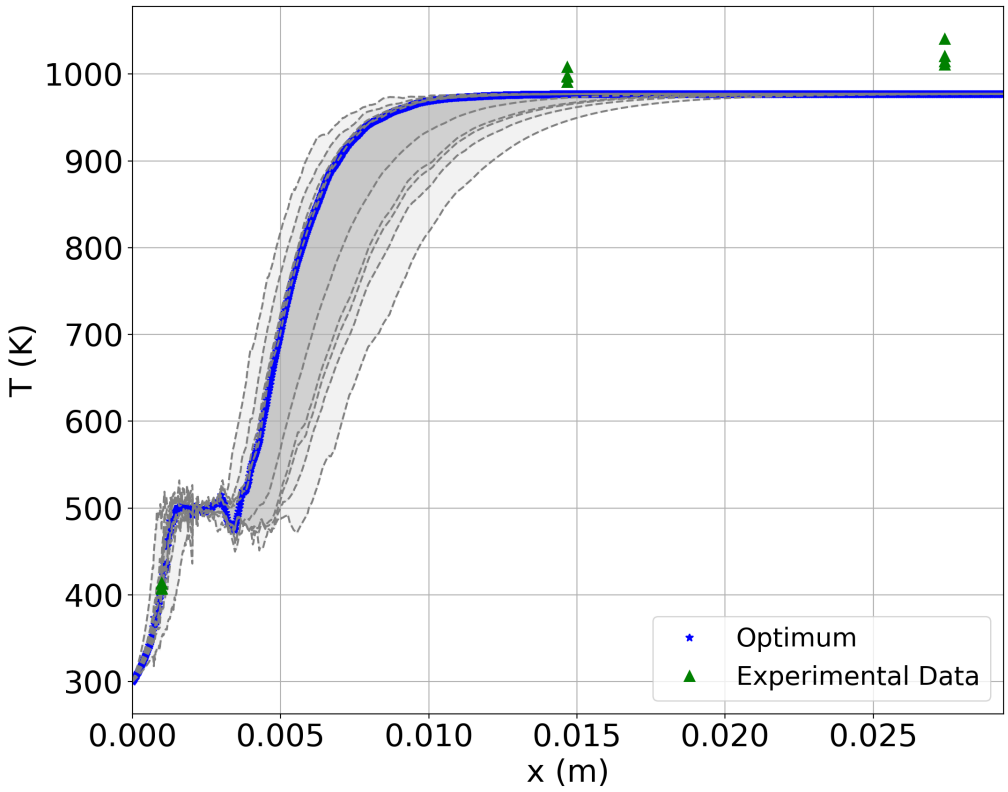

Figure B.2: Axial Temperature Profile with Confidence Intervals for Mock Data using 5^{th} Order Sparse Grid PCE with 8315 Samples

B.3 Miscellaneous

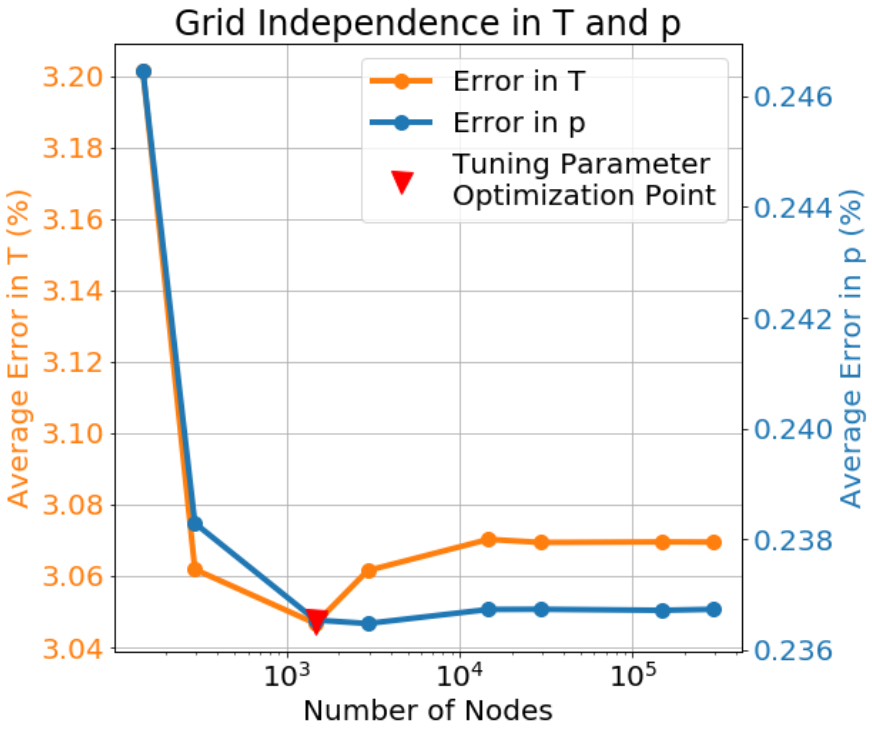

Figure B.3: Percent Error in Temperature and Pressure Profiles versus Grid Resolution

Several low fidelity grids were used to generate PCEs in T_{end} with inputs $\dot{m}$ and Y. The results were compared to those from a high fidelity PCE to evaluate how each method performed. The high fidelity PCE was generated using a 6^{th} order sparse grid trained using 257 direct simulations. High fidelity data in the following plots is shown by the contours with low fidelity direct simulation locations shown by the black points. Error for each method is computed using the L1 relative error between the high fidelity and low fidelity PCE results. Each low fidelity PCE is generated using 100 direct simulations.

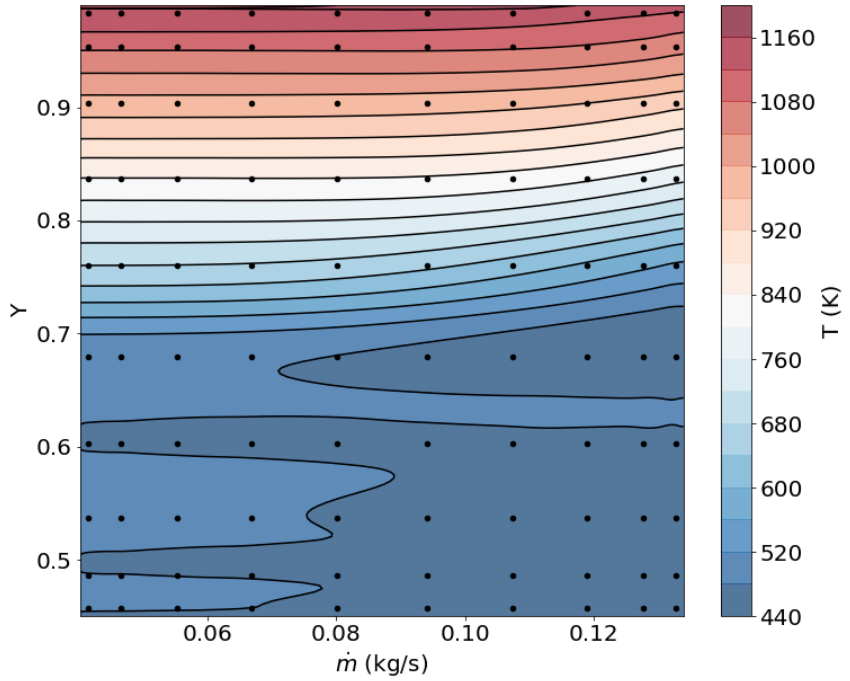

Figure B.4: 10^{th} Order Quadrature Grid Direct Samples on High Fidelity T_{end} PCE Contours (Error = 14.0%)

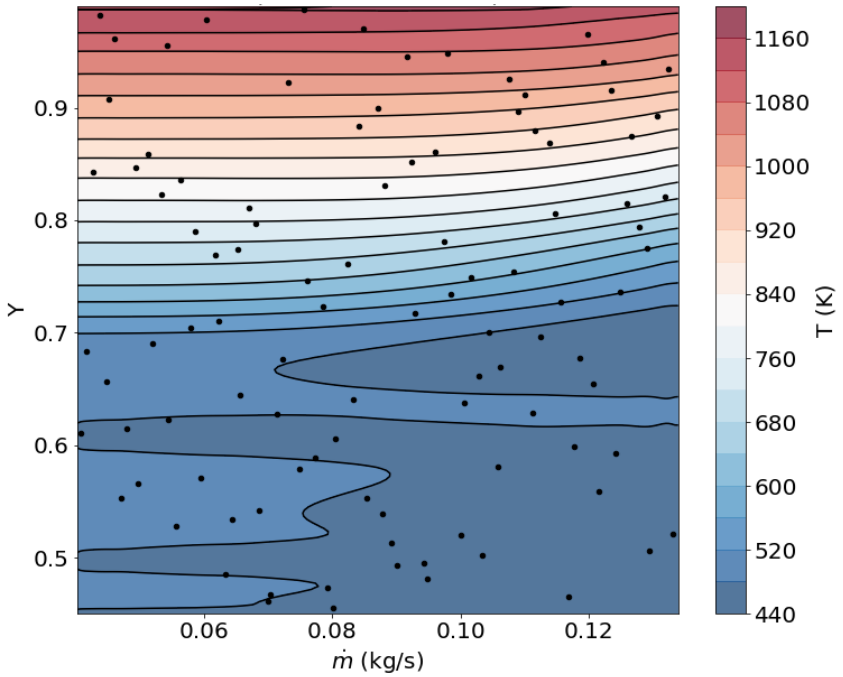

Figure B.5: Randomly Sampled Grid Direct Samples on High Fidelity T_{end} PCE Contours (Error = 69.6%)

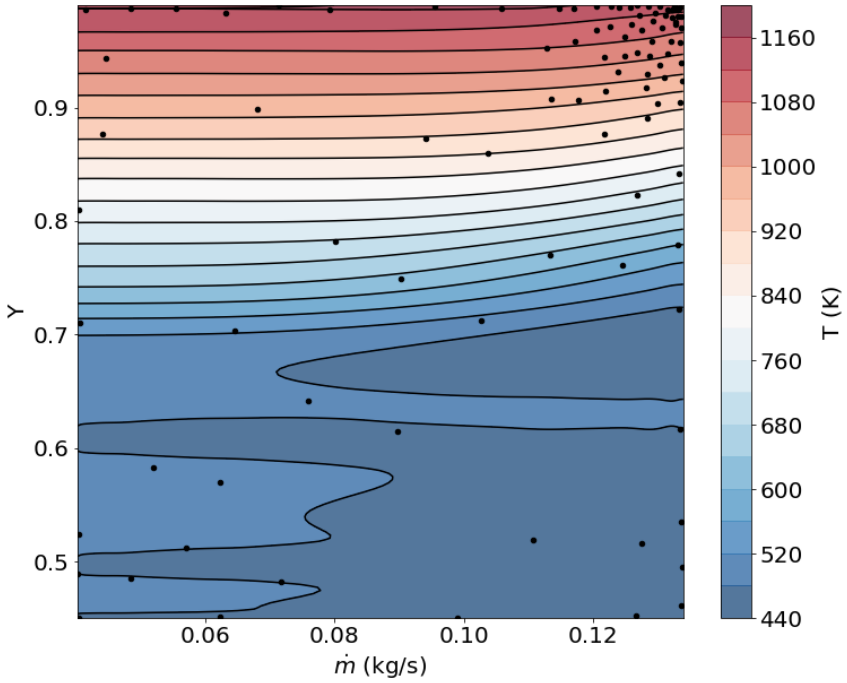

Figure B.6: Gradient-based Adaptive Grid Direct Samples on High Fidelity T_{end} PCE Contours (Error = 3E9%)

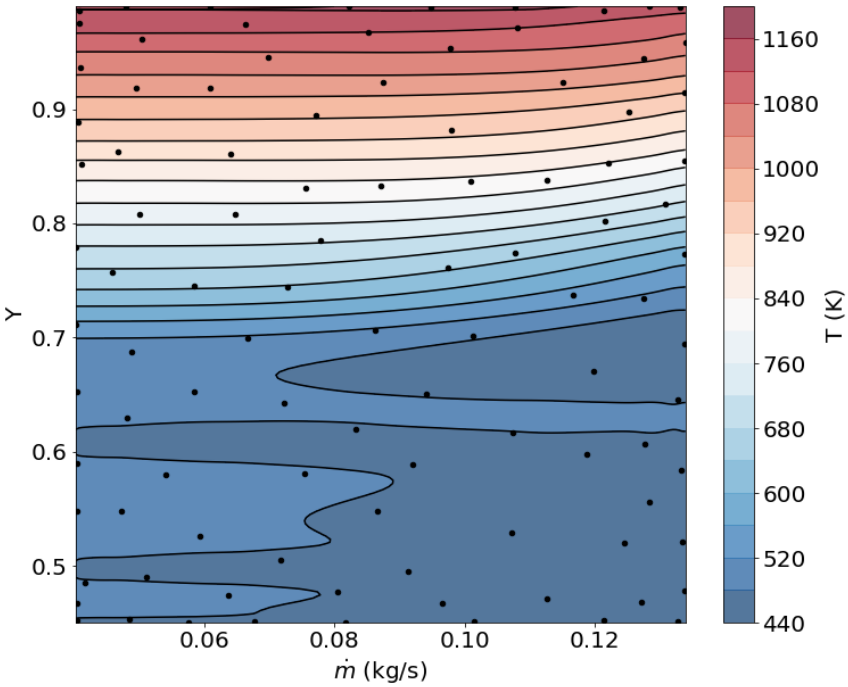

Figure B.7: Variance-based Adaptive Grid Direct Samples on High Fidelity T_{end} PCE Contours (Error = 1.26%)

REFERENCES

[1] Centers for Disease Control and Prevention. "CDC - Index of Chemicals - NIOSH Publications and Products.", 2016.

[2] National Center for Biotechnology Information. PubChem Compound Database. "Hydrogen Peroxide.", 2019.

[3] Rachid Amrousse, Toshiyuki Katsumi, Nobuyuki Azuma, and Keiichi Hori. "Hydroxylammonium Nitrate (HAN)-based Green Propellant as Alternative Energy Resource for Potential Hydrazine Substitution: From Lab Scale to Pilot Plant Scale-Up.". *Combustion and Flame*, 2017.

[4] National Aeronautics and Space Administration. "GPIM Fact Sheet: Green Propellant Infusion Mission Project.", 2018.

[5] Curtis Johnson, William Anderson, and Robert Ross. "Catalyst Bed Instability within the USFE H2O2/JP-8 Rocket Engine.". In *36th AIAA/ASME/SAE/ASEE Joint Propulsion Conference*.

[6] X. Zhou and D. L. Hitt. "One-Dimensional Modeling of Catalyzed H2O2 Decomposition in Microchannel Flows.". In *33rd AIAA Fluid Dynamics Conference and Exhibit*.

[7] L. M. Chiappetta, L. J. Spadaccini, H. Huang, W. Watkins, and A. M. Crocker. "Modeling a Hydrogen Peroxide Gas Generator for Rockets.". In *36th AIAA/ASME/SAE/ASEE Joint Propulsion Conference*.

[8] J. H. Corpening, S. D. Heister, and W. E. Anderson. "Thermal Decomposition of Hydrogen Peroxide, Part 2: Modeling Studies.". *Journal of Propulsion and Power*, 2006.

[9] A. Pasini, L. Torre, A. Cervone, and L. d'Agostino. "Reduced-Order Model for H2O2 Catalytic Reactor Performance Analysis.". *Journal of Propulsion and Power*, 2010.

[10] Sangwoo Jung, Sukmin Choi, and Sejin Kwon. "Design Optimization of Green Monopropellant Thruster Catalyst Beds Using Catalytic Decomposition Modeling.". In *53rd AIAA/SAE/ASEE Joint Propulsion Conference*.

[11] E. L. Cussler. *Diffusion: Mass Transfer in Fluid Systems*. Cambridge Series in Chemical Engineering. Cambridge University Press, 1997.

[12] Oliver Bey and Gerhart Eigenberger. "Fluid Flow through Catalyst Filled Tubes.". *Chemical Engineering Science*, 1997.

[13] C. K. Zoltani. "Flow Resistance in Packed and Fluidized Beds: An Assessment of Current Practice.". Technical report, U.S. Army Ballistic Research Laboratory, 1992.

[14] Larry A. Glasgow. *Transport Phenomena: An Introduction to Advanced Topics*. John Wiley & Sons, 2010.

[15] James F. Epperson. *An Introduction to Numerical Methods and Analysis*. John Wiley & Sons, 2007.

[16] Steven D. Chambreau, Denisia M. Popolan-Vaida, Ghanshyam L. Vaghjiani, and Stephen R. Leone. "Catalytic Decomposition of Hydroxylammonium Nitrate Ionic Liquid: Enhancement of NO Formation.". *The Journal of Physical Chemistry Letters*, 2017.

[17] Robert-Jan Koopmans, John S. Shrimpton, Graham T. Roberts, and Antony J. Musker. "A One-Dimensional Multicomponent Two-Fluid Model of a Reaction Packed Bed including Mass, Momentum and Energy Interphase Transfer.". *International Journal of Multiphase Flow*, 2013.

[18] Nian-Sheng Cheng. "Wall Effect on Pressure Drop in Packed Beds.". *Powder Technology*, 2011.

[19] Frank P. Incropera, David P. Dewitt, Theodore L. Bergman, and Adrienne S. Lavine. *Fundamentals of Heat and Mass Transfer*. John Wiley & Sons, 2007.

[20] Alan A. Esparza, Robert E. Ferguson, Ahsan Chouduri, Norman D. Love, and Evgeny Shafirovich. "Thermoanalytical Studies on the Thermal and Catalytic Decomposition of Aqueous Hydroxylammonium Nitrate Solution.". *Combustion and Flame*, 2018.

[21] Laurence Courthéoux, Dan Amariei, Sylvie Rossignol, and Charles Kappenstein. "Thermal and Catalytic Decomposition of HNF and HAN Liquid Ionic as Propellants.". *Applied Catalysis B: Environmental*, 2005.

[22] Sandia National Laboratories. *Dakota, A Multilevel Parallel Object-Oriented Framework for Design Optimization, Parameter Estimation, Uncertainty Quantification, and Sensitivity Analysis: Version 6.8 Theory Manual*.

[23] Gary Tang, Gianluca Iaccarino, and M. S. Eldred. "SDM 2010 Student Paper Competition Global Sensitivity Analysis for Stochastic Collocation.". In *51st AIAA/ASME/ASCE/AHS/ASC Structures, Structural Dynamics, and Materials Conference*.

[24] I. M. Sobol. "Sensitivity Estimates for Nonlinear Mathematical Models.". *MMCE*, 1993.

[25] D. S. Sivia and J. Skilling. *Data Analysis: A Bayesian Tutorial*. Oxford University Press, 2012.

[26] Nikos Drakos. "The Earth Mover's Distance.", Mar 1998.

[27] Rémi Flamary and Nicolas Courty. "POT Python Optimal Transport library.", 2017.

[28] Sandia National Laboratories. *Dakota, A Multilevel Parallel Object-Oriented Framework for Design Optimization, Parameter Estimation, Uncertainty Quantification, and Sensitivity Analysis: Version 6.8 User Manual*.

[29] Marc C. Kennedy and Anthony O'Hagan. "Bayesian Calibration of Computer Models.". *Journal of the Royal Statistical Society*, 2001.

[30] Argonne National Laboratory. "Active Thermochemical Tables v1.118.". Online. accessed June 5th, 2018.

[31] Stanley L. Manatt and Margaret R. R. Manatt. "On the Analyses fo Mixture Vapor Pressure Data: The Hydrogen Peroxide/Water System and Its Excess Thermodynamic Functions.". *Chem. Eur. J.*, 2004.

[32] A. L. Tsykalo and A. G. Tabachnikov. "Density, Viscosity, and Bond Energy of Molecules in Aqueous Hydrogen Peroxide solutions.". *Theoretical and Experimental Chemistry*, 2(6):604–605, Nov 1966.

[33] E. W. Lemmon, M. O. McLinden, and D. G. Friend. *NIST Chemistry WebBook, NIST Standard Reference Database Number 69*, chapter Thermophysical Properties of Fluid Systems. National Institute of Standards and Technology, 2019.

[34] Bonnie J. McBride and Sanford Gordon. *Computer Program for Calculation of Complex Chemical Equilibrium Compositions and Applications II. Users Manual and Program Description*. National Aeronautics and Space Administration.

[35] C. N. Satterfield, R. L. Wentworth, and S. T. Demetriades. "The Viscosity of Vapor Mixtures of Hydrogen Peroxide and Water.". Technical report, Massachusetts Institute of Technology, 1953.